ISBN 978-82-471-2749-0 (printed ver.)
ISBN 978-82-471-2748-3 (electronic ver.)
ISSN 1503-8181

Doctoral theses at NTNU, 2011:107

Sten Roar Snare

Quantitative Cardiac Analysis Algorithms for Pocket-sized Ultrasound Devices

NTNU
Norwegian University of
Science and Technology
Thesis for the degree of
philosophiae doctor
Faculty of Medicine
Department of Circulation and Medical Imaging

NTNU
Norwegian University of
Science and Technology

Doctoral theses at NTNU, 2011:107

NTNU

NTNU
Norwegian University of
Science and Technology

Sten Roar Snare

Quantitative Cardiac Analysis Algorithms for Pocket-sized Ultrasound Devices

Thesis for the degree of philosophiae doctor

Trondheim, April 2011

Norwegian University of
Science and Technology
Faculty of Medicine
Department of Circulation and Medical Imaging

NTNU
Norwegian University of
Science and Technology

NTNU
Norwegian University of Science and Technology

Thesis for the degree of philosophiae doctor

Faculty of Medicine
Department of Circulation and Medical Imaging

ISBN 978-82-471-2749-0 (printed ver.)
ISBN 978-82-471-2748-3 (electronic ver.)
ISSN 1503-8181

Doctoral Theses at NTNU, 2011:107

Printed by Tapir Uttrykk

Sammendrag

Siden introduksjonen i 1970-årene har ultralyd blitt ett av de viktigste verktøyene for påvisning av hjertesykdommer. De fleste ultralydundersøkelser er hurtige og smertefrie. Ultralydapparatene har tradisjonelt vært store og komplekse systemer, og det har vært nødvendig med omfattende opplæring og erfaring for å anvende dem. Fra årtusenskiftet har det blitt utviklet mindre og mer tilgjengelige ultralydapparater. Dette har resultert i lansering av flere *håndholdte* systemer. Disse apparatene har et enkelt brukergrensesnitt og relativt lav pris. En forventer at de også vil bli brukt av klinikere med mindre ultralyderfaring enn det som har vært tilfelle med de store skannerne.

Parallelt med utviklingen av håndholdte systemer har det vært gjort store fremskritt på sanntids 3D-avbildning med ultralyd. Mye av teknologien som har inngått i de nye 3D-systemene, har også spilt en nøkkelrolle i miniatyriseringen til håndholdte systemer. For sanntids 3D bildesegmentering har det blitt utviklet en svært effektiv algoritme basert på deformerbare modeller og Kalmanfilter. Denne løsningen burde være egnet for bruk på de minste systemene, hvor krav til beregningseffektivitet er høye. Vi har derfor undersøkt hvorvidt denne metoden også kan være egnet i sanntids brukerstøttesystemer for håndholdte ultralydskannere. Eksempler på anvendelser av håndholdt ultralyd innen ekkokardiografi, vil være å vurdere venstre hovedkammers (venstre ventrikkels) pumpefunksjon og å oppdage økning i hjertemuskemasse (hypertrofi). Venstre ventrikkels pumpefunksjon har vi vurdert ved hjelp av en algoritme som måler hvor mye klaffeplanet i hjertet beveger seg opp og ned gjennom en hjertesyklus. Sykelig hypertrofi innebærer at hjertets muskelmasse vokser, uten at det pumper bedre. Vi har utviklet og testet en algoritme for å oppdage hypertrofi ved å måle tykkelsen av ventrikkel septum, som er skilleveggen mellom hjertets høyre og venstre hovedkammer. Begge algoritmene synes å ha en nøyaktighet god nok til en hurtig undersøkelse, men de erstatter ikke en erfaren kardiolog med en ordinær skanner. For å slippe å bruke elektrokardiogram-elektrodene som finnes på større skannere, har vi utviklet en algoritme som automatisk finner ut hvor lang hjertesykelen er, og i tillegg, når den starter. Alle algoritmene over betinger at man har et godt opptak av hjertet for analysen. Vi har anvendt Kalmanfilteret til å lage et system for å gjenkjenne standardbilder av hjertet. En videreutvikling av dette, er en assistent for å hjelpe brukeren til å ta et av de vanligste og mest informative standardsnittene, det apikale firekammerbildet.

Formålet med alle disse algoritmene er å gjøre det enklere, spesielt for ikke-eksperter, å ta gode ultralydbilder av hjertet og hente ut nyttig kvantitativ informasjon ved hjelp av håndholdte ultralydsystemer. Våre resultater tilsier at Kalmanfilterbasert segmentering kan være et viktig bidrag til brukerstøttesystemer for håndholdte skannere.

Sten Roar Snare
Institutt for Sirkulasjon og Bildediagnostikk
Hovedveileder: Hans Torp
Biveiledere: Bjørn Olav Haugen og Svein Arne Aase
Finansieringskilde: BIA (brukerstyrt innovasjonsarena) prosjekt støttet av Norges Forskningsråd med GE Vingmed Ultrasound som industripartner.

Ovennevnte avhandling er funnet verdig til å forsvares offentlig for graden Philosophiae Doctor (PhD) i medisinsk teknologi. Disputas finner sted i Øya Helsehus (ØHA11) , torsdag 14. april kl. 12:15.

Abstract

Medical ultrasound is widely used within the field of cardiology. The pocket-sized ultrasound scanners with performance suitable for echocardiography represent one of the latest developments within ultrasound technology. It is forecasted that these scanners will be operated also by users with less experience than what has been the case for full-size scanners. Additionally, pocket-sized devices have less possibilities for user interaction due to the reduced screen size and limited space for buttons and sliders. It is likely that these scanners would benefit from having algorithms aiding the user to capture and interpret the images.

For 3D cardiac segmentation, an efficient Kalman filtering based approach has previously been developed and shown to operate in real-time on a commercial scanner. By reducing the problem to two dimensions, this approach could probably be used to provide real-time segmentation also on pocket-sized scanners. We have developed and tested Kalman filter based solutions for improved image acquisition and quantification of some selected parameters related to left ventricle size and performance. The algorithms are intended for use with pocket-sized ultrasound devices.

The main contributions of this thesis are:

- An automatic method for measuring the mitral annulus excursion, using a combination of low frame rate speckle tracking and model based segmentation.
- A novel method for semiautomatic measurement of interventricular septal thickness using a model based Kalman filter approach.
- A timing algorithm for estimation of cardiac cycle length and cycle start without using electrocardiography (ECG).
- Methods for recognizing standard apical echocardiographic views and assisting the user to find the apical four-chamber view during acquisition.

The mitral annulus excursion and septal thickness measurement projects were evaluated using patient ultrasound recordings and manual cardiologist measurements as reference values. In case of mitral annulus excursion measurements, the accuracy of the automatic algorithm was comparable to results published by other researchers. Regarding measurements of septal thickness, the algorithm accuracy was comparable to the discrepancy between two cardiologists. Although designed for automatic operation, the algorithm turned out to frequently require manual interaction due to unsatisfactory automatic initialization. The timing algorithm robustly identified cardiac cycle length in more than 91% and cycle start in more than 77% of the 11866 test cases extracted from patient data. The view detection method was tested on 37 patient recordings and correctly classified 87% of the standard views. Using the scan assistant, ten medical students managed to capture clinically acceptable apical four-chamber recordings in 85% of the cases, compared to 55% without the scan assistant.

Preface

This thesis is submitted to the Norwegian University of Science and Technology (NTNU) for partial fulfilment of the requirements for the degree of *Philosophiae Doctor* (PhD) at the Faculty of Medicine of the Norwegian University of Science and Technology (NTNU). The research has been funded by a User-driven Research based Innovation (BIA) project at the *Norwegian Research Council*, in cooperation with *GE Vingmed Ultrasound*. The work was carried out under the supervision of Dr.Techn Hans Torp at the Department of Ciculation and Medical Imaging, NTNU. Co-supervisors have been MD,PhdD Bjørn Olav Haugen and MSc,PhD Svein Arne Aase.

Acknowledgements

First of all, I would like to thank my main supervisor Hans for all kind guidance and inspiration during my PhD work. Hans is a remarkable well of enthusiasm and inspiring ideas. I have also appreciated the very low threshold for dropping by his office for a quick discussion. I do not think I ever have felt unwelcome in his office, and I am very grateful to have had him as my supervisor. I have also appreciated the support I have got from my co-supervisors Bjørn Olav and Svein Arne. We have had some great disucssions (and quite a few laughs). I also want to express my gratitude to Fredrik, who let me in to his RCTL project and allowed med to fiddle with, and sometimes mess up, his beatiful code library. In retrospect, the introduction to RCTL turned out to probably be the most important event in my PhD work. I am also very thankful for the cooperation with all the clincians at the department. It is always motivating to hear your opinions and get constructive feedback. In particular, I would like to mention Ole Christian and Håvard, who have contributed a lot to the work presented in this thesis. I would like to thank all my other co-authors for great cooperation and my fellow workmates at the department for the nice working environment. I would also like to mention former colleague Dag-Håkon, with whom I shared office during the two first years of my PhD work. We had some hilarious off-topic (and a few on-topic) discussions. I also want to thank GE Vingmed Ultrasound for the collaboration, in particular Vidar, Kjetil, Tor Arne, Arve and Sigmund for all kind assistance when playing with their scanners.

I want to thank my parents for encouragement and showing interest in my work. A special thought goes to my mother, who for some reason always believed that I would enjoy working with medical technology. I guess she was right. Finally, I will thank Thea for always being there, for always claiming that I will make it and to ignore some work-related frustrational outbursts when things have not gone as expected.

Table of Contents

Abbreviations

AAM	Active Appearance Model.
AAMM	Active Appearance Motion Model.
AMM	Anatomic M-mode.
ANN	Artificial Neural Network.
ASE	American Society of Echocardiography.
ASM	Active Shape Model.
CAUSE	Cardiac Arrest Ultrasound Exam.
ECG	Electrocardiogram/Electrocardiography.
ED	End Diastole.
EF	Ejection Fraction.
EKF	Extended Kalman Filter.
ES	End Systole.
FAST	Focused Assessment with Sonography in Trauma.
FIR	Finite Impulse Response.
HCM	Hypertrophic CardioMyopathy.
HCU	Hand-Carried Ultrasound.
IIS	Infinite Impulse Response.
IVSd	Interventricular Septum Thickness in end Diastole.
LA	Left Atrium.
LV	Left Ventricle.
MAE	Mitral Annulus Excursion.
MIMO	Multiple Input Multiple Output.
MMSE	Minimum Mean-Square Error.

NURBS	Non-uniform Rational B-splines.
PCA	Principal Component Analysis.
PDA	Personal Digital Assistant.
PSU	Pocket-Sized Ultrasound.
RA	Right Atrium.
RV	Right Ventricle.
SAD	Sum of Absolute Differences.
SLR	Single Lens Reflex.

Chapter 1

Introduction

Sten Roar Snare
Dept. Circulation and Medical Imaging, NTNU

1.1 Background and Motivation

Portable Ultrasound

Since the introduction in the 1970's, ultrasound as medical imaging modality has become one of the most important tools for detection of cardiac disease. The advantages, such as low cost, low risk and real-time images have made ultrasound the modality of choice for an extensive number of clinical applications. Since the late 1990's, portable ultrasound scanners have entered the market. In the echocardiographic literature, they are often termed Hand-Carried Ultrasound (HCU) devices. HCU scanners are typically battery operated and at the size of a laptop, or even a bit smaller. By using a carrying bag or shoulder strap, the system becomes portable. In the scanning setting, the scanner has to be placed on a table or similar.

The first HCU unit was presented as early as in 1978 (Minivisor, Organon Teknica) from the Thoraxcenter group in the Netherlands [1]. The Rochester group displayed their Scan Mate (Damon Corp) sector scanner in 1988. None of these devices were clinically accepted [2]. The main reason for this was poor image quality. During the 1990's, ultrasound technology was progressing rapidly forwards, making the leap to clinically feasible real-time 3D/4D ultrasound on commercial systems. At the same time as the high end systems grew more advanced, there was a trend towards developing smaller and less expensive systems meant for bedside use. In the period around year 2000, both SonoSite and Philips launched what they presented as handheld systems (SonoSite 180 and OptiGo respectively). In 2002, the American Society of Echocardiography (ASE) released their recommendations regarding these new systems [3] and introduced the term Hand-Carried Ultrasound (HCU). It was recommended to use HCU as an extension of the physical exam, and that users should have at least ASE "Level 1" of training before performing echocardiographic investigations.

In recent years, the development of HCU systems has started to diverge. Some

HCU systems get more functionality, including pulsed and continuous wave Doppler, M-mode and harmonic imaging. The other branch of systems is focusing towards further miniaturization. October 20th 2009, Jeff Immelt, being the vice president of General Electric, unveiled the latest of the portable ultrasound devices, the GE Vscan. Two years earlier, Siemens/Acuson launched their P10 and Direct Medical Systems their InNovaSound. Both the Vscan and the P10 are *pocket-sized* multi purpose scanners with decent image quality, harmonic imaging and frame rates suitable for cardiac applications. The Vscan also offers color flow functionality for blood flow visualization. The small size of the scanners makes them fit into the clinicians pocket. They can be operated using one hand to hold the scanner and one hand to hold the probe. Throughout this thesis we will use the term *Pocket-Sized Ultrasound (PSU)* devices to describe such scanners. In the literature these systems are also frequently encountered as handheld or PDA (personal digital assistant) type systems.

The number of sold HCU units in US has increased from 870 in year 2000 to 7500 units in 2008 [4]. The cost of a laptop-sized system is typically ranging from 15.000$ and upwards to 50-60.000$. Being fresh additions to the portable ultrasound market, the PSU systems do not make up a large share of the sold portable units. In 2008, one year after the introduction of InNovaSound and P10, only 125 of the 7500 portable units sold in the US were PSU systems. The selling price of less than 10.000$ is also lower than for typical HCU devices. The market forecast by Klein biomedical consultants [4] suggests that possible end users for the PSU systems will be physicians (family/general practice, internists, cardiologists, OB/GYN and emergency medicine) and maybe emergency medical services/technicians. They estimate the total addressable market for PSU devices in the US alone to be more than 1.5 Million units. In these estimates it was even assumed that PSU devices will not make it into the hospitals. In 2008, the forecast was fast unit growth from 125 PSU units in 2008 to 4570 units in 2013, combined with a drop in the average selling price from $8100 to $5300. This corresponds to an increase in revenues of 88%, which by far makes this the most rapidly growing segment in medical ultrasound.

Since 2002, numerous papers have been published on portable ultrasound. These devices cause great interest in many clinical fields of application. Within cardiology, HCU/PSU has been used for detection of hypertrophy, assessing LV chamber and wall dimensions, LV regional and global function and morphological abnormalities of the valves [5–15]. Most of the papers conclude that HCU/PSU has great potential and additional value provided that sufficient training is given. Spencer [16] was a bit more critical in his review paper, pointing out the danger of abusing the new technology. Being a valid concern, still the number of publications listing positive experiences with HCU devices suggests that such equipment has a future within cardiology, provided proper training [17]. Similar conclusions are drawn within radiology [18, 19] and emergency care [20, 21]. There are several publications specifically addressing PSU systems, presenting thoughts and considerations related to the latest step on the miniaturization scale [2, 5, 6, 9, 10, 12, 14, 15, 18, 19, 22, 23]. Not all of the published studies have actually used PSU equipment in their studies. The authors in [5, 10, 15] used PSU devices for their studies on cardiac size and function, and they reported good results. Cardim et al. [6] investigated how the use of a PSU device as an extension of

the physical examination changed the workflow in an outpatient clinic. Giusca et al. [9] tested the usefulness of PSU when operated by cardiology trainees and found it to be helpful, although not a replacement for a standard examination. A similar study using a more limited protocol and expert users was published in [12]. Pozza et al. [22] compared PSU, HCU and regular scanners in a pediatric cardiology setting and found the image quality of the PSU to be inferior, while still claiming that the PSU unit could be helpful in certain clinical settings. These results were also discussed in the editorial paper of Kimura [23], where the author raised the important question of what defines an echo machine? The answer to that question is essential for how to compare and test PSU equipment, where screen size and temporal resolution has been traded off to gain portability and usability. The European Association of Echocardiography has recently also published a position paper [24] providing recommendations on the use of PSU devices.

Operating a full-size scanner properly requires long experience and extensive training. If the market predictions and forecasts for PSU systems are correct, these scanners will most likely be operated also by clinicians less experienced with use of ultrasound equipment. One of the main uncertainties is whether non-expert users will be able to conduct a proper clinical ultrasound examination. The amount of training which should qualify for performing PSU investigations is a research topic for itself, but to require the same level of training for all users of PSU systems is likely to be economically and practically intractable. It is forecasted that non-expert PSU users frequently will perform *focused* ultrasound examinations, such as FAST [25] or CAUSE [26]. In case of focused ultrasound, tailored and less comprehensive training protocols could be adopted [27]. In addition, the scanners should be equipped with functionality to aid the user when performing focused examinations. The relation between PSU and regular scanners can be compared to the relation between compact digital cameras and complex single lens reflex (SLR) cameras. The potential for taking superb images is higher for the SLR camera, while the compact camera, with its user friendliness, may be the better solution for less experienced users.

First and foremost, the acquired image must have acceptable quality. In echocardiography this translates to, in addition to having correct image settings, getting a proper acoustic window and angling the probe such that the anatomy is shown correctly on the screen. An algorithm aiding the user to acquire clinically acceptable images would be of great interest. Such functionality can be implemented either as user feedback from the scanner during the acquisition, or as a post-processing step to quality check or identify views in already recorded material. The first solution has the advantage that the user gets real-time information and can continuously adjust the probe position to get the required view. One disadvantage is that the real-time requirement puts restrictions on the complexity of the algorithms to be run. Another problem may be that, in the worst case, the user feedback can disturb the user while struggling to find the optimal view. View detection work in the literature is mostly restricted to offline post-processing algorithms to identify views from a dataset containing different standard views. Various approaches have been presented, such as model template fit combined with support vector machines [28], multiresolution elastic registration [29] and hierarchical classification [30]. The, to our best knowledge, most

recent publication addressing cardiac view detection, is the work by Park et al. [31] who applied a solution based on machine learning from an annotated database and got a classification accuracy of 96%. Orderud et al. [32] published related work on automatic *alignment* of standard views in 3D echocardiography using an efficient extended Kalman filter.

In addition to getting the correct view, quantification on a PSU device is inherently more difficult due to the small screen and few knobs/sliders. The scanner should thus have functionality to aid the user when making some of the most common measurements.

Left ventricle contractility has traditionally been measured using the Ejection Fraction (EF) [1]. Using two dimensional ultrasound, the EF measurement typically involves manual tracing of the left ventricle cavity in one or multiple projections of the heart. The tracings are then used to calculate EF, either by area or volume ratios using Simpson's rule. With the advent of 3D ultrasound, EF can be found without assuming a particular geometry. In case of PSU devices, three dimensional imaging is not yet available, and manual tracing is unpractical. Correct measurement of EF also requires recordings where the complete left ventricle is visible, which can be difficult to achieve for non-expert users. Another way of measuring left ventricle contractility is to use the mitral annulus excursion. This is a measurement of how much the mitral annulus moves towards the cardiac apex during the systole. This has shown to be a valuable measure of cardiac contractile performance, and has been shown to correlate well with EF [33–36]. This measurement does not require the complete left ventricle to be visible in the image and should thus be more suitable for non-expert users. Several authors have published semi-automatic approaches for mitral annulus excursion measurements. Nevo et al. [37] presented a low frame rate (25Hz) method based on dynamic programming combined with apodized block matching. Eto et al. [38] presented a high frame rate speckle tracking approach, using manual initialization. Some studies based on the commercial Philips QLab high framerate speckle tracking system [39], which also utilizes manual initialization, have also been presented [33, 34].

In cardiology, hypertrophy means that segments of the heart is growing. This can be due to exercise or pathology. In the latter case, the muscle gets bigger while the contractility is reduced. Local hypertrophies can also obstruct normal blood flow or cause valvular problems [40]. Pathologic compensatory hypertrophy can be caused by hypertension over a longer period of time. Another disease state where there is pathological hypertrophy of the left ventricle is hypertrophic cardiomyopathy (HCM). HCM is often characterized by asymmetric septal hypertrophy, frequently close to the aortic tract [40, 41]. Hypertrophy increases the risk for adverse cardiac events and heart failure [42]. Patients with isolated septal hypertrophy, without increased LV mass, have a higher prevalence for diastolic dysfunction and arrhythmias [43]. According to the American College of Cardiology Foundation/American Heart Association guidelines [44], echocardiography may be used to detect hypertrophy also in asymptomatic patients.

Hypertrophy is commonly diagnosed by estimation of LV mass. In 2D

[1] $EF = \frac{EDvolume - ESvolume}{EDvolume}$

echocardiography, formulas exist which take septal and posterior wall thickness together with ventricular diameter as input to calculate LV mass [45]. It is common to use M-mode and caliper functionality to do this measurement. As an approximation, sometimes only the septal thickness measurement is made. A normal septum is approximately 1cm thick [46]. There have been few attempts to automize this measurement. Moladoust et al. [47] used an adaptive thresholding scheme to measure septum thickness in apical images. Subramanian et al. [48] did the measurement in parasternal views, applying a variant of the active shape algorithm with local region based segmentation energy.

Both mitral annulus excursion and LV mass measurements rely on identification of the cardiac cycle. Mitral annulus excursion measurements require identification of both end diastole and end systole, while LV mass can be estimated using measurements from the end diastole only. In case of mitral annulus excursion, by ignoring cases of post-systolic shortening, it is possible to directly use the maximum and minimum values of the excursion during a complete cardiac cycle. Still, the cardiac cycle length has to be estimated. This introduces some challenges for PSU equipment, as these devices do not have the option of connecting electrocardiogram (ECG) leads for cardiac cycle detection. Thus, manual cycle definition or a different automatic approach must be chosen. Previous research on cardiac cycle identification has been related to fetal ultrasound [49–51]. Due to the high heart rates and little respiratory motion, longer sequences with many heart cycles can be used. This enables the use of for instance Fourier analysis. In case of adults, the problem is slightly different because of the slower heart rate and respiratory motion. The number of cardiac cycles which can be present in the input signal for cycle identification is limited and other solutions must be considered.

Segmentation schemes in ultrasound

In order to make user assistance algorithms for ultrasound, it is frequently necessary to apply automatic segmentation schemes for identification of interesting regions or objects in the image. This problem of *image segmentation* in echocardiographic images has been an extensively studied topic for decades, and numerous solutions have been presented. A full review of all the possible algorithms is out of the scope of this thesis, and the interested reader is recommended to consult the excellent review papers by Noble et al. [52] or Hammoude et al. [53]. Algorithms studied in the literature include schemes based on artificial neural networks (ANN), level sets/fast marching methods, fuzzy logic, mathematical morphology and various region- and pixel-based classification based algorithms. In this section, we will briefly mention some selected terms and solutions.

Cost function based methods rely on minimizing a cost or energy function for finding the most probable border through an edge map identified by an edge operator. By incorporating prior knowledge into the cost function, it is possible to correctly segment the structure of interest by applying an optimization procedure. The computation time and accuracy is tightly connected to the size and accuracy of the search space for the optimization problem.

Cost function schemes can also be applied to *active contour models*. In these cases the structure of interest is modeled as a deformable curve, which is then fitted to the image data using cost minimization. This approach can be implemented efficiently, but is often sensitive to initialization. The methods are suitable for extensions to incorporate time and the third dimension. Various optimization schemes [52] have been applied, such as gradient descent techniques, Newton/quasi-Newton methods, dynamic programming or genetic algorithms. Methods based on statistical/probabilistic theory, such as simulated annealing, maximum likelihood or maximum a posteriori (MAP) estimation, are also frequently encountered. The cost functions can contain a number of different terms. External terms such as intensity gradients, energy (gray level statistics, Rayleigh distribution), phase information, regional forces, optical flow and speckle statistics have all been applied [52, 53]. The cost functions can also have internal terms, such as curve shape/smoothness and temporal regularization. This ensures sensible shapes and motion, and can be used to make the model compliant with prior knowledge.

By using *active shape models* (ASM) as contours, it is possible to incorporate more prior knowledge into the model. This can make the segmentation scheme faster by reducing the numbers of parameters to estimate. However, it can also cause problems when encountering new pathologies which were not included in the training set. A popular extension of ASM, using prior information about intensities, is called active appearance modeling (AAM). Bosch et al. [54] extended the AAM to what they named active appearance motion model (AAMM), which incorporates motion as well. An advantage of this approach could be that principal component analysis (PCA) is used to model temporal patterns, as well as spatial patterns. This makes it possible to include more prior information about movement into the segmentation scheme.

A framework for using a *Kalman filter* for segmentation was developed by Blake et al. [55–57] and later adapted to 2D echocardiography by Jacob et al. [58, 59]. Orderud et al. [60] extended it to 3D and could report real-time capabilities even in 3D. These methods use a parametric model of the object of interest, in combination with a motion model. The filter can have different inputs, such as edge measurements and block matching. The prior shape knowledge is built into the parametric model. Hansegård et al. [61] applied active shape models in the Kalman filter framework. The temporal motion pattern still has to be modeled in the kinematic model, which can get complex.

Much of the enabling technology for pocket-sized ultrasound came from the development of real-time 3D scanners. Achieving real-time 3D requires efficient algorithms and advanced electronics. By running the Kalman filter segmentation using 2D instead of 3D data, Orderuds approach could potentially be able to run in real-time even on miniaturized systems. This could open up for a series of user-assistance applications benefiting from the Kalman filter segmentation. This thesis is thus devoted to developing and testing real-time Kalman filter based algorithms for use with pocket-sized ultrasound devices. The Kalman filter approach is described in detail in Chapter 2.

1.2 Aims of study

Since the advent of pocket-sized ultrasound devices, one of the main uncertainties has been whether non-expert users will be able to use the equipment correctly. Compared to full-size scanners, pocket-sized systems have reduced temporal resolution, smaller screens, less possibilities for interfacing the user and, most likely, a more diverse user population. This work aims to investigate whether algorithms based on real-time Kalman filter segmentation can be used to improve the usability and user friendliness of pocket-sized ultrasound systems, in particular when operated by less experienced users. Although it is not an aim to implement the algorithms on a physical pocket-sized scanner, they should be fast and suitable for operation with such devices.

More detailed, the work aims to:

- Assist the user in measuring left ventricle systolic function.
- Assist the user to detect hypertrophy.
- Investigate whether it is possible to automatically detect cardiac cycle length and start, without using an electrocardiogram.
- Aid the user in capturing and recognizing a good apical view for left ventricle analysis

1.3 Summary of presented work

All of the presented algorithms are using the Kalman filter, either alone (Chapters 4, 6 and 7) or in combination with other techniques, such as speckle tracking (Chapter 3) or intensity analysis and database lookup (Chapter 5). The Kalman filter is described in detail in Chapter 2. We have applied an extended Kalman filter with non-uniform rational B-spline models. In general, the Kalman filter has proved fast, flexible and robust to noise. None of the algorithms used more than $7.7ms$ computation time per frame. The flexibility of the algorithm has been illustrated in the septum thickness and view detection work, where a transform hierarchy and multiple submodels have been used to create more complex anatomical models.

1.3.1 Contribution 1 - Mitral annulus excursion measurement (Chapter 3)

Mitral annulus excursion is often used as an indicator of the global left ventricle contractile function. On full-size scanners, this distance measurement is normally made using M-mode or anatomic M-mode. More recently, speckle tracking based algorithms, such as the algorithm in the Philips Qlab quantification system [39], have also become commercially available.

On PSU devices, due to the limited temporal resolution, it can be difficult to generate anatomic M-mode images. Even if making anatomic M-mode was feasible, due to the lack of mouse/touch pad and the small screen, it would be challenging to

do a reliable mitral annulus excursion measurement using a caliper function. Regular speckle tracking is also non-trivial. Due to the low frame rate, image speckle may move significantly between frames. We developed a fully automatic solution which combines speckle tracking and left ventricle Kalman filter segmentation to make a robust mitral annulus excursion estimate.

The algorithm was tested using 30 PSU and 29 HCU apical four-chamber recordings made by a cardiologist, who also did reference measurements. The algorithm was tested in both fully automatic and semi-automatic operation. In case of automatic operation, the algorithm was run using a batch script. After two full cardiac cycles, the reported mitral annulus excursion value was stored together with an image of the displacement curve. Only tracking the septal part of the mitral annulus was also tested, as the image quality generally is better on the septal side of the apical four-chamber images. During semi-automatic operation, a second cardiologist, blinded to the reference values, operated the algorithm offline on a regular laptop. He had the option of doing corrections to the initialization and to turn off lateral point tracking. Using PSU data, 15 of 30 recordings were then processed fully automatic. For the HCU device the number was lower, as only 5 of 29 recordings were processed without human interaction. The most common correction was re-initialization of tracking points or disabling the lateral point tracking.

Comparing the automatic PSU results to the anatomic M-mode reference measurements, a paired t-test revealed an error of $-1.80 \pm 1.96mm$ when both the lateral and septal side of the mitral annulus were tracked and $-0.27 \pm 1.89mm$ when only using the septal side. When tested with HCU recordings, the results were only slightly improved. Allowing for manual interaction, the errors were reduced to $-1.57 \pm 1.72mm$ when using PSU. We found the algorithm results to be underestimated when the lateral point was included, which is similar to previously published comparisons between speckle tracking and anatomic M-mode based measurements [62]. The standard deviation was less than 2mm, which should be considered acceptable given the image quality and number of patients included in the study. The results suggest that the algorithm measures MAE using PSU data with an accuracy suitable for rapid assessment of left ventricle systolic performance.

This topic is described in the paper "Fast automatic measurement of mitral annulus excursion using a pocket-sized ultrasound system" accepted for publication in *Ultrasound in Medicine and Biology*. The paper is a joint work with Ole Christian Mjølstad, who performed the ultrasound examinations and contributed significantly to the data analysis.

1.3.2 Contribution 2 - Measurement of septal thickness (Chapter 4)

Septal thickness can be used as a parameter to detect LV septal hypertrophy [46]. LV hypertrophy is an important risk factor for cardiac events [42] and should thus be detected as early as possible. Septum thickness should preferably be measured at end diastole using the parasternal long-axis view [46]. It is common to do the measurement using M-mode or anatomic M-mode. Using a regular scanner, this can be performed

directly after acquisition or on a workstation after the exam. The measurement should be made at the level of the mitral valve tip.

We developed an algorithm based on coupled parametric models of the septum, mitral valve leaflet and aortic outlet tract. All the models are arranged in a transform hierarchy, in order to fit with the parasternal long-axis view. The control points of the parametric curves and the geometric transform parameters are used as states in a Kalman filter. The Kalman filter uses edge measurements and speckle tracking as input. Accurate measurement of septal thickness requires correct handling of structures which are not parts of the septum. Including trabeculae and the moderator band in the measurement will cause overestimation. We addressed these problems by making the models stiffer in regions where the comibation of these structures and unclear edges are expected. Normally, the moderator band is easiest identifiable in the apical regions of the right ventricle side of the septum. When the moderator band is visible, a low intensity region between the septum and the moderator band is frequently observed. We applied a tailored edge detector termed a "double edge detector" to detect this region.

The measurement should not be made based on B-mode information from single frames, as the moderator band and right ventricle trabeculae often can not be visually separable from the septum in single frames. We addressed this problem by continuously monitoring the septum through the heart cycle, and thus include temporal information into the segmentation. The measurement is displayed on screen together with a measurement line for visual reference.

The algorithm was tested on 37 patients, whereof five had suspected hypertrophy. Using a paired t-test, we found an error of (mean $\pm$ SD) $0.14 \pm 1.36mm$ compared to cardiologist B-mode measurements. This was comparable to the discrepancy between B-mode measurements made by two cardiologists, which was found to be $1.29 \pm 1.23mm$. The algorithm performed fully automatic in 78.4% of the cases, while depth initialization was failing in the remaining 21.6%. As a fast assessment of septal thickness, where the goal is to decide whether further investigations should be made or not, the algorithm is considered successful.

This project is described in the paper "Automated Septum Thickness Measurement - a Kalman Filter Approach", accepted for publication in *Computer Methods and Programs in Biomedicine*.

1.3.3 Contribution 3 - Echocardiography without ECG (Chapter 5)

On regular cardiac scanners, it is common to use an echocardiogram (ECG) to identify cardiac events and cycle length. Connecting ECG leads to the patient when using PSU systems is unpractical. It would introduce more cables and slow down the acquisition process, as the patient would need to be connected to the ECG electrodes prior to the exam.

We developed and tested an algorithm for cardiac cycle length and cycle start estimation, without using ECG. This enables automatic storage and looping of the cardiac cycle during playback, as well as eases quantitative measurements to be taken

at certain steps in the cardiac cycle, such as the end-diastole. For cycle length estimation, a sum of absolute differences (SAD) based algorithm is applied to intensity curves extracted from different parts of the image. The resulting cycle length is found by taking the median of regional results. The cycle start estimation is utilizing Kalman filter segmentation to extract mitral annulus excursion curves. This is similar to the procedure in the mitral annulus excursion measurement project. The displacement curve is then processed and provided as input to an algorithm which estimates the cardiac cycle start using a displacement waveform shape lookup procedure.

We tested the algorithm using recordings from the HUNT database [63]. The proposed algorithm had a feasibility for cycle length estimation of 98% when tested with normal subjects and 91% for pathology cases. The median error, when compared to ECG, was 0 and $-3ms$ respectively. The cycle start estimation turned out to be less robust and was feasible for 90% of the normal subjects and 77% of the pathology cases. The median error for cycle start was 62 and $76ms$ respectively.

Cardiac cycle length and cycle start estimation without ECG is explored in the paper "Echocardiography without ECG", which was a joint effort with postdoctoral researcher Svein Arne Aase and published in *European Journal of Echocardiography*.

1.3.4 Contribution 4 - Real-time view detection and scanning aid (Chapter 6 and Chapter 7)

An important prerequisite for evaluating cardiac function, is to have a decent imaging view of the heart. We developed and tested two approaches for addressing this challenge. One approach was a view identification algorithm aiming to recognize an echocardiographic view as being one of the standard apical views. The other solution was a scan assistant which aimed to help the user acquiring an apical four-chamber view. Both methods were using the Kalman filter segmentation scheme to fit parametric models of the preferred views to the image data. A quality-of-fit measure was used to give the user feedback on the current view.

For view detection, multiple apical view models are fitted to the image data. By analyzing the number of discarded edge detection measurements, a a score for how well each model fits to the image data is calculated. If the image quality is low, or if the model has a poor fit, the score will be low. If the current view is one of the standard views, the score will have a peak for one of the view models. The algorithm was trained using 31 randomly selected recordings, with approximately ten recordings from each of the standard apical views (apical long-axis, apical two-chamber and apical four-chamber). After training, another 37 random recordings were used for validation. The view was correctly classified in 32 of the 37 cases (86.5%). This method can be used to identify which of the standard views the user has acquired. This can be for instance be used as a preprocessing step for automatic algorithms. The algorithm is presented in the paper "Automatic Real-time view detection" published in the *Proceedings of IEEE Ultrasonic Symposium 2009*.

We also developed a scan assistant tool which aims to help the user to acquire an apical four-chamber view. This is one of the most informative views during an echocardiographic examination. Also, two other apical views (apical two-chamber and

apical long-axis) can be obtained by doing rotations of the probe, starting out from the four-chamber view. For the untrained user, assistance in getting the four-chamber view correctly would be of great value. The scan assistant tool was implemented and tested on a GE Vingmed E9 cardiac scanner (GE Vingmed Ultrasound, Horten, Norway). A model of the apical four-chamber is fitted in real-time to the image data. A quality-of-fit score is calculated and shown to the user together with an icon ("emoticon") indicating the view quality. The assistant was tested using ten medical students, who examined two healthy volunteers during two sessions separated more than four days in time. Half of the group used the scan assistant during their first session, while the other half used it during the second session. All recordings were later randomized, anonymized and rated by a cardiologist. The students managed to capture recordings of acceptable quality in 85% of the cases when using the scan assistant, compared to 55% when not using the assistant. Use of the scan assistant improved the view quality from poor to acceptable in 8 of 9 (89%) cases. The manuscript "Real-time Scan Assistant for Echocardiography" submitted to *IEEE Transactions on Ultrasonics and Ferroelectrics* describes the algorithm and the results.

1.3.5 List of publications

Papers included in the Thesis

1. **Sten Roar Snare**; Ole Christian Mjølstad; Fredrik Orderud; Bjørn Olav Haugen; Hans Torp "Fast automatic measurement of mitral annulus excursion using a pocket-sized ultrasound system", *Ultrasound in Medicine and Biology*, 2011, In Press

2. **Sten Roar Snare**; Ole Christian Mjølstad; Fredrik Orderud; Håvard Dalen; Hans Torp, "Automated Septum Thickness Measurement - a Kalman Filter Approach", accepted for publication in *Computer Methods and Programs in Biomedicine*

3. Svein Arne Aase; **Sten Roar Snare**; Håvard Dalen; Asbjørn Støylen; Fredrik Orderud; Hans Torp, "Echocardiography without electrocardiogram", *European Journal of Echocardiography*, vol. 12, no. 1,pp. 3-10, 2011.

4. **Sten Roar Snare**; Svein Arne Aase; Ole Christian Mjølstad; Håvard Dalen; Fredrik Orderud; Hans Torp, "Automatic Real-time View Detection", *Proc. IEEE Ultrason. Symp. 2009*

5. **Sten Roar Snare**; Hans Torp; Fredrik Orderud; Bjørn Olav Haugen, "Real-time Scan Assistant for Echocardiography", submitted to *IEEE Transactions on Ultrasonics, Ferroelectrics and Frequency Control*

Related work not included in the Thesis

1. Svein Arne Aase; **Sten Roar Snare**, Ole Christian Mjølstad, Håvard Dalen, Fredrik Orderud, Hans Torp, "QRS detection and cardiac cycle separation

without ECG", *Proc. IEEE Ultrason. Symp. 2009*

2. **Sten Roar Snare**; Hans Torp, "Estimating Frequency Dependent Attenuation to Improve Automatic Time Gain Compensation in B-mode Imaging", *Proc. IEEE Ultrason. Symp. 2008*

1.4 Evaluation and Discussion of Results

The work presented in this thesis illustrates applications of real-time Kalman filter based segmentation intended for use with pocket-sized ultrasound. The segmentation scheme is used in all of the projects, either alone as in the septal thickness measurements and view quality projects, or combined with other approaches, as in the mitral annulus excursion measurement and ultrasound without ECG projects.

Although the focus for this thesis has been computationally efficient algorithms for use with PSU equipment, it was not an aim to implement the algorithms on a PSU device. The presented algorithms have all had measured computation times $< 7.7ms/frame$ on a laptop computer. A PSU device operating at approximately 20 frames per second, has a time slot for calculations of 50ms. We believe that the efficiency of the algorithms should facilitate implementation on PSU devices. In case of the mitral annulus excursion project, we were able to test the algorithm on data captured from a PSU device (the GE Vscan). The results suggest that the algorithm functioned with the image quality and frame rate found on a commercial PSU device.

Our aim was to test the Kalman filter approach, as this was an approach which had already proved to be highly efficient and whose flexibility laid ground for use in multiple applications. The Kalman filter may not be the only solution which is sufficiently efficient for a PSU implementation. For a future study, when the technical limitations of the PSU devices are better mapped, a thorough benchmarking of methods should be considered.

1.4.1 Mitral annulus excursion measurement

The parametric model used in the mitral annulus excursion estimation algorithm is used to initialize and constrain a more regular speckle tracking procedure. The mean error of $-1.80 \pm 1.96mm$ for the fully automatic and $-1.57 \pm 1.72mm$ for the semi-automatic analysis using PSU data, indicates an underestimation compared to manual anatomic m-mode measurements. This was also supported by the results when using HCU/laptop scanner data. When only using the septal tracking point for analysis, the automatic measurement was not biased. Similar results have previously been reported in [62].

The Pearson's correlation coefficients range between $r = 0.61$ and $r = 0.69$ and are lower than some of the other numbers encountered in the literature, where regular scanners have been used. One explanation for this could be that the excursion values in our patient data had a narrow range of 6 to $14mm$, while for instance Eto et al. [38] had a range of 1.9 to $24.6mm$. We believe that the correlation coefficient would benefit from having a wider range in the data.

When the algorithm was operated semi-automatically, only 50% of the PSU data and 17% of the HCU data were processed without human interaction. In a few cases, the model position was re-initialized, but most frequently the corrections were re-initialization of the tracking points or disabling the lateral point. Judging from the results, the main effect of the manual interaction was reduced maximum errors. On average, the improvements were so small that it can hardly be justified to turn to the semi-automatic approach on PSU devices.

The accuracy suggests it should be possible to fully automatically separate between healthy and poorly contracting ventricles, which can be considered a main goal for operation with PSU devices. The tendency of underestimation can cause some false positives being unneccesarily referred to a more thorough cardiac exam. The standard deviation of the error is relatively high. Converting the standard deviation of the error to EF, using a factor of 5 [35] yields 9.8% for the PSU results. For comparison have interobserver numbers for EF, using full-size scanners and Simpsons rule, been reported to range from 4.2% (a study on echogenic patients) to 10.7% [64].

Our results indicate small differences between the results from the two scanners. This was unexpected, as the lower frame rate on the PSU device should favor the HCU scanner. One reason may be that the HCU recordings had some issues with gain settings, causing intensity saturation in the basal region. The similar results can also be explained by the image quality being limited by the acoustic window and reverberations/aberrations, not the technical limitations of the equipment.

The computation time of 3.7ms/frame on a dual core 1.17GHz laptop computer suggests that a real-time implementation is feasible. The advantage of real-time operation would primarily be to display the mitral annulus excursion value during the scan. In this way the user will get a feel for the variability and robustness of the measurement.

A topic for future research could be to relieve the real-time constraint in order to gain accuracy. Then other techniques, such as a Kalman smoother and two-way speckle tracking [65] may be applied. Nevo et al. [37] used a low frame rate dynamic programming approach, which outperformed the regular forward tracking scheme. They reported a computation time of (mean $\pm$ SD) 162.1 ± 10.3 seconds. Such solutions, utilizing the whole loop, can possibly improve the accuracy, but is obviously not applicable for real-time operation.

As no ECG is available, the mitral annulus excursion value is calculated using maximum and minimum excursion directly. In case of post-systolic shortening, that is when the ventricle is contracting even more after end systole, the excursion value will be over-estimated. This is not easily resolved without ECG. A topic for further work could be to investigate a velocity curve, constructed from the displacement data, to identify the true end systole by a near-zero velocity.

1.4.2 Septum thickness

The proposed solution provides information about septal hypertrophy. Hypertensive hypertrophy is commonly seen as symmetric [66]. Hypertrophic cardiomyopathy, on the other side, is often asymmetric [40]. The presented algorithm would detect

asymmetric septal hypertrophy, but would not detect asymmetric hypertrophy in the posterior wall.

The paired t-test revealed a non-significant mean error compared to the average of the manual caliper measurements from two cardiologists of $(mean \pm SD)$ $0.14 \pm 1.36mm$. The 95% limits of agreement were $-2.53mm$ to $2.81mm$. When comparing the B-mode caliper reference measurements from the two cardiologists, the t-test yielded a statistically significant difference of $1.29 \pm 1.23mm$. The correlation coefficient between the algorithm and the cardiologists was $0.79 (p < 0.001)$. Between the cardiologists, the correlation was $0.84 (p < 0.001)$. Based on these results, it seems as if the algorithm is unbiased. The larger measurement errors of the algorithm exceed the difference between normal and mildly hypertrophic septa, but the accuracy should be adequate for separating normal and moderately hypertrophic septa, according to the normal ranges in [46]. The standard deviation of the error is similar to that of the measurement difference between the two clinicians. This indicates that the algorithm accuracy is comparable to the inconsistency between trained cardiologists, which should be sufficient to make it clinically acceptable for use with pocket-sized ultrasound devices. The variability of the measurement error is high compared to the range of the septal thickness measurement.

Manual septal thickness measurements are also reported to have large interobserver variation. Using manual M-mode measurements, interobserver variability has been reported to range from 9.1% [67] to 12% [63]. Converting the mean error between the algorithm and manual M-mode measurements to percentage yields 11.3%, and is thus in the same range as these numbers. Numbers for B-mode measurements were not found in the literature. Here, the interobserver error for the two cardiologists using B-mode was found to be 15%, which is somewhat higher than the M-mode numbers from the literature. The variability in the B-mode references seems to originate from a few recordings where the two cardiologists interpret differently the borders on the right ventricle side of the septum. Correct measurement of septal thickness using B-mode images is challenging both for the algorithm and humans. Especially the right ventricle structures can make it hard to identify the true septal border, which probably is also why the recommendations [46] suggest to also use (targeted) M-mode for this measurement.

Due to local thickness variations, the measurement can be dependent on the measurement level, which in turn is based on identification of the mitral valve tip. The mitral valve and its tip is often poorly visible. The septum models may also fail to accurately follow local variations in the septum shape, especially in the stiffer parts of the models.

The computation time of 7.7ms per frame on a dual core 1.17GHz laptop computer, suggests that a real-time implementation could be feasible on PSU scanners.

The algorithm performed automatic in 78.4% of the test cases, and is thus within range of becoming fully automatic. The depth initialization procedure sometimes failed to correctly identify the septum. Improving the depth initializer is a topic for further research. Unfortunately, the data analysis was not split. It would have been interesting to analyze the fully automatic results separately.

Using a semi-automatic algorithn, Moladoust et al. [47] reported measurement

errors for septum thickness in apical images to have standard deviations of 0.87 and 0.89mm in base and mid septal regions respectively. The reference method and clinical foundation for this work is a bit unclear. Subramanian et al. [48] proposed to use an active shape algorithm with local region based segmentation energy. They also applied a motion clustering scheme to detect the mitral valve. The computation time was reported to be 100ms per frame on a 2.6GHz computer with 2GB RAM. They analyzed 57 recordings and reported an accuracy of $(mean \pm SD)$ $0.88 \pm 0.96mm$ and $1.17 \pm 0.92mm$ versus two different cardiologists respectively. This is a significantly better accuracy than our proposed method, although it should be noted that Subramanian et al. did not make any statements whether they used a separate training set, nor how the recordings were selected. Their proposed mitral valve detector is also incompatible with real-time operation.

The septum thickness measurement does not really *need* to be real-time. By utilizing the data stored in the image buffer, the measurement can be performed as a post-processing step. For the Kalman filter, turning to an offline solution, would make it feasible to use other estimation schemes, such as a Kalman smoother [68] or an unscented Kalman filter [69]. This is a topic for further research. As of now, aiming for real-time operation, only information up to the current time step is utilized.

1.4.3 Echocardiography without ECG

The results from the validation study, indicate that cardiac cycle length estimation without ECG is feasible. The estimate has a very small median error, and the 85% percentile of -15ms to 15ms on healthy subjects and -17ms to 14ms on subjects with pathology is considered tolerable. Cycle start estimation was less robust with a feasability of 77% for subjects with pathology. The median error of 62ms for healthy and 76ms for pathologic cases indicates that the method is slightly biased. The 85% percentile is wider (-4ms to 160ms). The better robustness of the the cycle length estimate is partly explained by the assumption that it is easier to detect the repetition of any event than to detect a predefined, single event in a cardiac cycle. The cardiac cycle start algorithm also involves speckle tracking to measure the longitudinal motion of the mitral annulus. This introduces more sources of errors than a purely intensity based approach.

The current algorithm has an inherent heart rate range limitation. It relies on a sum of absolute differences (SAD) fit of a template to detect the cardiac cycle length. If the length of the data buffer is long compared to the template length, there is a risk that there are multiple local optima for the SAD function. We have presumed that the SAD function has one single global minimum. This imposes restrictions on the heart rates, depending on the template length. Using our current setup, the supported range is from 45 to 90 beats per minute. This suffices for most cardiac examinations in resting subjects. However, for trauma patients, the heart rates can be outside the supported range. By using a training set with a wider span in the cycle lengths, the algorithm could possibly be tuned to support other heart rates. To completely relieve the heart rate range limitation, the algorithm must be redesigned to handle multiple minima in the SAD function. It is worth noting that the failure mode when the

algorithm is applied to higher framerates than supported, is to store multiple cycles. In some applications this may not constitute a problem.

The model-based cycle start estimation is limited by the assumption of an apical view of the heart. Future work could involve an extension of the algorithm to also handle parasternal views. Note that this limitation is not imposed on the cycle length algorithm.

1.4.4 View detection and Scan assistant

The view detection algorithm successfully identified the standard views in 86.7% of the 37 test cases. The apical long-axis was the most frequently misidentified view, where two of elleven cases were misclassified as being apical two-chamber views. This is probably caused by poor visibility of the aortic outlet tract, which is the most reliable landmark to separate a two-chamber view from an apical long-axis view. In two other cases, apical four-chamber views were identified as two-chamber views. This was caused by poor visibility of the right ventricle in combination with foreshortened atria. We did not establish whether non-standard views were successfully rejected by the system. For instance, there is a risk that a corrupt four-chamber view missing large parts of either the left or right side, can be misinterpreted as a two-chamber view. Extending the validation and, if required, the algorithm to robustly filter out non-standard views is a topic for further research.

The scan assistant was targeted towards acquisition of the apical four-chamber view only. We presented promising results when the assistant was used by non-expert users. When using the scan assistant and showing the template model on screen, 85% of the recordings were of acceptable (good or fair) quality. Without showing the model, 80% were of acceptable quality, and with no scan assistant only 55% of the recordings were acceptable. It is also important to note that use of the scan assistant improved the quality from poor to acceptable in 89% of the cases when showing the model. It should be noted that in two cases (10%) when the scan assistant was used with model display, the image quality degraded from acceptable to poor when using the assistant. In one case the image quality remained poor. All of these cases happened when the scan assistant was used to examine subject 2 during the first session. It may be that display of the view template model on the screen confused the students, who were unfamiliar with the situation and struggled hard to find an acoustic window on subject 2. Also, one of the cases of degradation included a recording where the student stored the image while the scan assistant was reporting poor quality.

The main challenge for the scan assistant algorithm turned out to be failing detection of oblique views. Particularly challenging were the cases where the atria were visible but deformed. This is related to the distinction between *view quality* and *image quality*. The number of successful edge detections are used to generate the quality scores. An edge detection either fails because the edge is too weak to be reliable (image quality), or because there is no edge close to the cavity model (orientation/view quality). Poorly fitting atrial models, having a percentage of successful edge detections lower than a certain threshold, are used to detect oblique cuts. In order to approve a good view having medium to poor image quality, the threshold for atrium detection

must be lowered. In recordings having good image quality, with good contrast and intensity, few edges are discarded due to image quality. As a result, the number of spurious edges and edges from deformed atria may in some cases cause faulty identification of the atria, leading to failed detection of foreshortening/oblique cuts.

Further studies should focus on improved detection of foreshortening. This could either be achieved by taking the atrial *shapes* into account when calculating the score values, or by using an adaptive discard threshold for cavity detection, yielding a better separation between view and image quality. Currently, the focus has been on apical views. We did not test the scan assistant with parasternal views. This also seems less relevant, as the apical and parasternal views are taken from two different scanning windows. It should not be possible to confuse parasternal and apical views. For further studies, it would be interesting to also investigate the application of a parasternal view model in the scan assistant framework. It is essential to keep the real-time operation, as our results suggest that non-expert users of ultrasound benefit from getting feedback on the view quality *during* image acquisition.

1.5 Conclusion

In this work we have developed and tested user assistance and quantification algorithms for echocardiography using pocket-sized ultrasound devices. We presented automated algorithms for rapid assessment of mitral annulus excursion values and septal thickness measurements. We also presented an algorithm intended to replace some of the functionality of the electrocardiogram on high end scanners. Finally, we developed an algorithm to aid untrained users acquiring and recognizing standardized images of the heart. The possibility of applying the algorithms in real-time reduces the need for post-processing and can speed up the examination.

The algorithms have all been utilizing an extended Kalman filter in conjunction with non-uniform rational B-splines. The Kalman filter approach has demonstrated computational efficiency, versatility and noise robustness. The convergence radius of the models has been adequate. For the mitral annulus excursion measurement project our results are comparable to previously published results, but more accurate offline high frame rate algorithms have been published. In the septal thickness case, we achieved an accuracy comparable to the inconsistency between two cardiologists. We have been successfully estimating the cycle length without ECG leads, and in most cases even the cycle start/end diastole time point. The proposed scan assistant was shown to be a promising aid for inexperienced users.

Overall, the Kalman filter approach is likely to be well suited for applications with miniaturized scanners. As the use of pocket-sized ultrasound devices become more widespread, we hope that the presented work can be a contribution to making echocardiography accessible for non-expert users.

References

[1] C. Ligtvoet, H. Rusterborgh, L. Kappen, and N. Bom, "Real time ultrasonic imaging with a hand-held scanner Part I–Technical description," *Ultrasound in Medicine & Biology*, vol. 4, pp. 91–92, 1978.

[2] E. C. Vourvouri and J. R. T. C. Roelandt, "Ultrasound Stethoscopy," in *Echocardiography* (P. Nihoyannopoulos and J. Kisslo, eds.), ch. 32, pp. 619–636, London: Springer London, 2009.

[3] J. Seward, "Hand-carried cardiac ultrasound (HCU) device: Recommendations regarding new technology. A report from the Echocardiography Task Force on New Technology of the Nomenclature and Standards Committee of the American Society of Echocardiography," *Journal of the American Society of Echocardiography*, vol. 15, pp. 369–373, Apr. 2002.

[4] Klein Biomedical Consultants, "The U.S. Market for Portable Ultrasound Systems: Challenges & Opportunities 2008 Report," 2009.

[5] C. Prinz and J.-U. Voigt, "Diagnostic Accuracy of a Hand-Held Ultrasound Scanner in Routine Patients Referred for Echocardiography.," *Journal of the American Society of Echocardiography : official publication of the American Society of Echocardiography*, pp. 0–5, Dec. 2010. Epub ahead of print 2011 Jan 10.

[6] N. Cardim, C. Fernandez Golfin, D. Ferreira, A. Aubele, J. Toste, M. A. Cobos, V. Carmelo, I. Nunes, A. Gouveia Oliveira, and J. Zamorano, "Usefulness of a New Miniaturized Echocardiographic System in Outpatient Cardiology Consultations as an Extension of Physical Examination.," *Journal of the American Society of Echocardiography : official publication of the American Society of Echocardiography*, pp. 1–8, Nov. 2010. Epub ahead of print 2011 Jan 10.

[7] G. Perez-Avraham, S. L. Kobal, O. Etzion, V. Novack, T. Wolak, N. Liel-Cohen, and E. Paran, "Left ventricular geometric abnormality screening in hypertensive patients using a hand-carried ultrasound device.," *Journal of clinical hypertension (Greenwich, Conn.)*, vol. 12, pp. 181–6, Mar. 2010.

[8] E. Vourvouri, "Left ventricular hypertrophy screening using a hand-held ultrasound device," *European Heart Journal*, vol. 23, pp. 1516–1521, Oct. 2002.

[9] S. Giusca, R. Jurcut, R. Ticulescu, D. Dumitru, A. Vladaia, O. Savu, A. Voican, B. a. Popescu, and C. Ginghina, "Accuracy of Handheld Echocardiography for Bedside Diagnostic Evaluation in a Tertiary Cardiology Center: Comparison with Standard Echocardiography.," *Echocardiography (Mount Kisco, N.Y.)*, Nov. 2010.

[10] B. C. Culp, J. D. Mock, C. D. Chiles, and W. C. Culp, "The Pocket Echocardiograph: Validation and Feasibility.," *Echocardiography (Mount Kisco, N.Y.)*, pp. 1–6, Apr. 2010.

[11] E. C. Vourvouri, A. F. L. Schinkel, J. R. T. C. Roelandt, F. Boomsma, G. Sianos, M. Bountioukos, F. B. Sozzi, V. Rizzello, J. J. Bax, H. I. Karvounis, and D. Poldermans, "Screening for left ventricular dysfunction using a hand-carried cardiac ultrasound device.," *European journal of heart failure : journal of the Working Group on Heart Failure of the European Society of Cardiology*, vol. 5, pp. 767–74, Dec. 2003.

[12] B. J. Kimura, G. W. Gilcrease, B. K. Showalter, J. N. Phan, and T. Wolfson, "Diagnostic performance of a pocket-sized ultrasound device for quick-look cardiac imaging.," *The American journal of emergency medicine*, vol. 1, pp. 1–5, Oct. 2010.

[13] L. Croft, W. Duvall, and M. Goldman, "A pilot study of the clinical impact of hand-carried cardiac ultrasound in the medical clinic," *Echocardiography*, vol. 23, no. 6, pp. 439–446, 2006.

[14] M. Egan and a. Ionescu, "The pocket echocardiograph: a useful new tool?," *European journal of echocardiography : the journal of the Working Group on Echocardiography of the European Society of Cardiology*, vol. 9, pp. 721–5, Nov. 2008.

[15] S. Fukuda, K. Shimada, T. Kawasaki, H. Fujimoto, K. Maeda, H. Inanami, K. Yoshida, S. Jissho, H. Taguchi, M. Yoshiyama, and J. Yoshikawa, "Pocket-sized transthoracic echocardiography device for the measurement of cardiac chamber size and function.," *Circulation journal : official journal of the Japanese Circulation Society*, vol. 73, pp. 1092–6, June 2009.

[16] K. Spencer and R. Lang, "Point of service echocardiography," *ACC Cardiosource Review Journal*, vol. 1458, no. 02, pp. 49–51, 2002.

[17] K. Spencer, "Hand-carried cardiac ultrasound," *Current Cardiovascular Imaging Reports*, vol. 17, pp. 399–403, May 2008.

[18] J. Wise, "Everyone's a radiologist now," *British Medical Journal*, vol. 336, pp. 1041–1043, May 2008.

[19] H. Edwards, "Special Feature Let's all jump on the ultrasound bandwagon : further debate on the use of ultrasound," *Ultrasound*, vol. 18, pp. 4 –7, 2010.

[20] R. Breitkreutz, S. Price, H. V. Steiger, F. H. Seeger, H. Ilper, H. Ackermann, M. Rudolph, S. Uddin, M. a. Weigand, E. Müller, and F. Walcher, "Focused echocardiographic evaluation in life support and peri-resuscitation of emergency patients: A prospective trial.," *Resuscitation*, vol. 81, pp. 1527–1533, Aug. 2010.

[21] D. M. Spevack, P. A. Tunick, and I. Kronzon, "Hand carried echocardiography in the critical care setting.," *Echocardiography (Mount Kisco, N.Y.)*, vol. 20, pp. 455–61, July 2003.

[22] R. D. Pozza, M. Loeff, R. Kozlik-Feldmann, and H. Netz, "Hand-Carried Ultrasound Devices in Pediatric Cardiology: Clinical Experience with Three Different Devices in 110 Patients.," *Journal of the American Society of Echocardiography : official publication of the American Society of Echocardiography*, vol. 23, pp. 1231–1237, Oct. 2010.

[23] B. J. Kimura, "What Is an Echo Machine?," *Journal of the American Society of Echocardiography*, vol. 23, pp. 1238–1241, Dec. 2010.

[24] R. Sicari, M. Galderisi, J.-u. Voigt, G. Habib, J. L. Zamorano, P. Lancellotti, and L. P. Badano, "The use of pocket-size imaging devices : a position statement of the European Association of Echocardiography," *European Journal of Echocardiography*, pp. 10–12, 2011. Epub ahead of print 2011 Jan 07.

[25] T. M. Scalea, A. Rodriguez, W. C. Chiu, F. D. Brenneman, J. Fallon, W. F., K. Kato, M. G. McKenney, M. L. Nerlich, M. G. Ochsner, and H. Yoshii, "Focused assessment with sonography for trauma (fast): results from an international consensus conference," *J Trauma*, vol. 46, no. 3, pp. 466–72, 1999.

[26] C. Hernandez, K. Shuler, H. Hannan, C. Sonyika, A. Likourezos, and J. Marshall, "C.A.U.S.E.: Cardiac arrest ultra-sound exam–a better approach to managing patients in primary non-arrhythmogenic cardiac arrest.," *Resuscitation*, vol. 76, pp. 198–206, Feb. 2008.

[27] A. J. Labovitz, V. E. Noble, M. Bierig, S. a. Goldstein, R. Jones, S. Kort, T. R. Porter, K. T. Spencer, V. S. Tayal, and K. Wei, "Focused cardiac ultrasound in the emergent setting: a consensus statement of the american society of echocardiography and american college of emergency physicians.," *Journal of the American Society of Echocardiography : official publication of the American Society of Echocardiography*, vol. 23, pp. 1225–30, Dec. 2010.

[28] S. Ebadollahi, S. Chang, and H. Wu, "Automatic view recognition in echocardiogram videos using parts-based representation," in *Computer Vision and Pattern Recognition,*, 2004.

[29] S. V. Aschkenasy, C. Jansen, R. Osterwalder, A. Linka, M. Unser, S. Marsch, and P. Hunziker, "Unsupervised image classification of medical ultrasound data by multiresolution elastic registration.," *Ultrasound in medicine & biology*, vol. 32, pp. 1047–54, July 2006.

[30] M. Otey, J. Bi, S. Krishna, B. Rao, J. Stoeckel, A. Katz, J. Han, and S. Parthasarathy, "Automatic view recognition for cardiac ultrasound images," in *in Proceedings of Int'l Workshop on Computer Vision for Intravascular and Intracardiac Imaging*, pp. 187–194, 2006.

[31] J. H. Park, S. Zhou, C. Simopoulos, J. Otsuki, and D. Comaniciu, "Automatic cardiac view classification of echocardiogram," in *2007 IEEE 11th International Conference on Computer Vision*, 2007.

[32] F. Orderud, H. Torp, and S. I. Rabben, "Automatic alignment of standard views in 3D echocardiograms using real-time tracking," *Proceedings of SPIE*, pp. 72650D–72650D–7, 2009.

[33] J. M. DeCara, E. Toledo, I. S. Salgo, G. Lammertin, L. Weinert, and R. M. Lang, "Evaluation of left ventricular systolic function using automated angle-independent motion tracking of mitral annular displacement.," *Journal of the American Society of Echocardiography*, vol. 18, pp. 1266–9, Dec. 2005.

[34] W. Tsang, H. Ahmad, A. R. Patel, L. Sugeng, I. S. Salgo, L. Weinert, V. Mor-Avi, and R. M. Lang, "Rapid estimation of left ventricular function using echocardiographic speckle-tracking of mitral annular displacement.," *Journal of the American Society of Echocardiography*, vol. 23, pp. 511–5, May 2010.

[35] K. Emilsson, "The relation between mitral annulus motion and ejection fraction: A nonlinear function," *Journal of the American Society of Echocardiography*, vol. 13, pp. 896–901, Oct. 2000.

[36] M. F. Elnoamany and A. K. Abdelhameed, "Mitral annular motion as a surrogate for left ventricular function: correlation with brain natriuretic peptide levels.," *European journal of echocardiography : the journal of the Working Group on Echocardiography of the European Society of Cardiology*, vol. 7, pp. 187–98, June 2006.

[37] S. T. Nevo, M. van Stralen, A. M. Vossepoel, J. H. C. Reiber, N. de Jong, A. F. W. van der Steen, and J. G. Bosch, "Automated tracking of the mitral valve annulus motion in apical echocardiographic images using multidimensional dynamic programming.," *Ultrasound in medicine & biology*, vol. 33, pp. 1389–99, Sept. 2007.

[38] Y. Eto, H. Yamada, J.-H. Shin, D. a. Agler, H. Tsujino, J.-X. Qin, G. Saracino, N. L. Greenberg, J. D. Thomas, and T. Shiota, "Automated mitral annular tracking: a novel method for evaluating mitral annular motion using two-dimensional echocardiography.," *Journal of the American Society of Echocardiography*, vol. 18, pp. 306–12, Apr. 2005.

[39] Philips, "Qlab cardiac analysis [online]." http://www.healthcare.philips.com/in_en/products/ultrasound/technologies/QLAB/cardiac/index.wpd, October 2010.

[40] L. K. Williams, M. P. Frenneaux, and R. P. Steeds, "Echocardiography in hypertrophic cardiomyopathy diagnosis, prognosis, and role in management.," *European journal of echocardiography : the journal of the Working Group on Echocardiography of the European Society of Cardiology*, vol. 10, pp. iii9–14, Dec. 2009.

[41] E. Braunwald, D. Zipes, and L. P., eds., *Heart disease: a textbook of cardiovascular medicine*, vol. 1. Philadelphia, Pennsylvania: W.B. Saunders Company, 6th ed., 2001.

[42] G. Mancia, G. De Backer, A. Dominiczak, R. Cifkova, R. Fagard, G. Germano, G. Grassi, A. M. Heagerty, S. E. Kjeldsen, S. Laurent, K. Narkiewicz, L. Ruilope, A. Rynkiewicz, R. E. Schmieder, H. A. Boudier, A. Zanchetti, A. Vahanian, J. Camm, R. De Caterina, V. Dean, K. Dickstein, G. Filippatos, C. Funck-Brentano, I. Hellemans, S. D. Kristensen, K. McGregor, U. Sechtem, S. Silber, M. Tendera, P. Widimsky, J. L. Zamorano, S. Erdine, W. Kiowski, E. Agabiti-Rosei, E. Ambrosioni, L. H. Lindholm, M. Viigimaa, S. Adamopoulos, E. Agabiti-Rosei, E. Ambrosioni, V. Bertomeu, D. Clement, S. Erdine, C. Farsang, D. Gaita, G. Lip, J. M. Mallion, A. J. Manolis, P. M. Nilsson, E. O'Brien, P. Ponikowski, J. Redon, F. Ruschitzka, J. Tamargo, P. van Zwieten, B. Waeber, and B. Williams, "2007 guidelines for the management of arterial hypertension: The task force for the management of arterial hypertension of the european society of hypertension (esh) and of the european society of cardiology (esc)," *J Hypertens*, vol. 25, no. 6, pp. 1105–87, 2007.

[43] D. Harpaz, T. Rosenthal, E. Peleg, and A. Shamiss, "The correlation between isolated interventricular septal hypertrophy and 24-h ambulatory blood pressure monitoring in apparently healthy air crew.," *Blood pressure monitoring*, vol. 7, pp. 225–9, Aug. 2002.

[44] P. Greenland, J. S. Alpert, G. A. Beller, E. J. Benjamin, M. J. Budoff, Z. A. Fayad, E. Foster, M. A. Hlatky, J. M. Hodgson, F. G. Kushner, M. S. Lauer, L. J. Shaw, J. Smith, Sidney C., A. J. Taylor, W. S. Weintraub, and N. K. Wenger, "2010 ACCF/AHA Guideline for Assessment of Cardiovascular Risk in Asymptomatic Adults: A Report of the American College of Cardiology Foundation/American Heart Association Task Force on Practice Guidelines Developed in Collaboration With the American Society of Echocardiography, American Society of Nuclear Cardiology, Society of Atherosclerosis Imaging and Prevention, Society for Cardiovascular Angiography and Interventions, Society of Cardiovascular Computed Tomography, and Society for Cardiovascular Magnetic Resonance," *J Am Coll Cardiol*, vol. 56, no. 25, pp. e50–103, 2010.

[45] M. Foppa, B. B. Duncan, and L. E. P. Rohde, "Echocardiography-based left ventricular mass estimation. How should we define hypertrophy?," *Cardiovascular ultrasound*, vol. 3, p. 17, Jan. 2005.

[46] R. M. Lang, M. Bierig, R. B. Devereux, F. a. Flachskampf, E. Foster, P. a. Pellikka, M. H. Picard, M. J. Roman, J. Seward, J. Shanewise, S. Solomon, K. T. Spencer, M. St John Sutton, and W. Stewart, "Recommendations for chamber quantification.," *European journal of echocardiography : the journal of the Working Group on Echocardiography of the European Society of Cardiology*, vol. 7, pp. 79–108, Mar. 2006.

[47] H. Moladoust, M. Mokhtari-Dizaji, and Z. Ojaghi-Haghighi, "Determination of instantaneous interventricular septum wall thickness by processing sequential 2D echocardiographic images.," *Pakistan journal of biological sciences: PJBS*, vol. 10, no. 3, p. 454, 2007.

[48] N. Subramanian, D. Padfield, S. Thiruvenkadam, A. Narasimhamurthy, and S. Frigstad, "Automated interventricular septum thickness measurement from B-mode echocardiograms.," *Medical image computing and computer-assisted intervention : MICCAI ... International Conference on Medical Image Computing and Computer-Assisted Intervention*, vol. 13, pp. 510–7, Jan. 2010.

[49] M. S. Sklansky, T. R. Nelson, and D. H. Pretorius, "Usefulness of gated three-dimensional fetal echocardiography to reconstruct and display structures not visualized with two-dimensional imaging.," *The American journal of cardiology*, vol. 80, pp. 665–8, Sept. 1997.

[50] G. R. DeVore, P. Falkensammer, M. S. Sklansky, and L. D. Platt, "Spatio-temporal image correlation (STIC): new technology for evaluation of the fetal heart.," *Ultrasound in obstetrics & gynecology : the official journal of the International Society of Ultrasound in Obstetrics and Gynecology*, vol. 22, pp. 380–7, Oct. 2003.

[51] F. Viñals, P. Poblete, and a. Giuliano, "Spatio-temporal image correlation (STIC): a new tool for the prenatal screening of congenital heart defects.," *Ultrasound in obstetrics & gynecology : the official journal of the International Society of Ultrasound in Obstetrics and Gynecology*, vol. 22, pp. 388–94, Oct. 2003.

[52] J. A. Noble and D. Boukerroui, "Ultrasound image segmentation: a survey.," *IEEE transactions on medical imaging*, vol. 25, pp. 987–1010, Aug. 2006.

[53] A. Hammoude, "Endocardial border identification in two-dimensional echocardiographic images: review of methods.," *Computerized medical imaging and graphics : the official journal of the Computerized Medical Imaging Society*, vol. 22, no. 3, pp. 181–93, 1998.

[54] J. G. Bosch, S. C. Mitchell, B. P. F. Lelieveldt, F. Nijland, O. Kamp, M. Sonka, and J. H. C. Reiber, "Automatic segmentation of echocardiographic sequences by active appearance motion models.," *IEEE transactions on medical imaging*, vol. 21, pp. 1374–83, Nov. 2002.

[55] A. Blake, R. Curwen, and A. Zisserman, "A framework for spatio-temporal control in the tracking of visual contours," *Int. J. Comput. Vis.*, vol. 11, no. 2, pp. 127–145, 1993.

[56] A. Blake, M. Isard, and D. Reynard, "Learning to track the visual motion of contours," *Artificial Intelligence*, vol. 78, pp. 179–212, Oct 1995.

[57] A. Blake and M. Isard, *Active Contours*. New York: Springer-Verlag, 1998.

[58] G. Jacob, J. A. Noble, M. Mulet-Prada, and A. Blake, "Evaluating a robust contour tracker on echocardiographic sequences," *Med. Image Anal.*, vol. 3, pp. 63–75, 1999.

[59] G. Jacob, J. Noble, C. Behrenbruch, A. Kelion, and A. Banning, "A shape-space-based approach to tracking mycordial borders and quantifying regional left-ventricular function applied in echocardiography," *IEEE Trans. Med. Imag.*, vol. 21, pp. 226–238, Mar 2002.

[60] F. Orderud and S. I. Rabben, "Real-time 3d segmentation of the left ventricle using deformable subdivision surfaces," in *Computer Vision and Pattern Recognition, IEEE Computer Society Conference on*, (Los Alamitos, CA, USA), pp. 1–8, IEEE Computer Society, June 24-26 2008.

[61] J. Hansegård, F. Orderud, and S. Rabben, "Real-time active shape models for segmentation of 3d cardiac ultrasound," in *Computer Analysis of Images and Patterns* (W. Kropatsch, M. Kampel, and A. Hanbury, eds.), vol. 4673 of *Lecture Notes in Computer Science*, pp. 157–164, Springer Berlin / Heidelberg, 2007.

[62] S. Y. Hayashi, B. I. Lind, A. Seeberger, M. M. do Nascimento, B. J. Lindholm, and L.-A. Brodin, "Analysis of mitral annulus motion measurements derived from M-mode, anatomic M-mode, tissue Doppler displacement, and 2-dimensional strain imaging.," *Journal of the American Society of Echocardiography*, vol. 19, pp. 1092–101, Sept. 2006.

[63] A. Thorstensen, H. Dalen, B. H. Amundsen, S. A. Aase, and A. Stoylen, "Reproducibility in echocardiographic assessment of the left ventricular global and regional function, the hunt study," *Eur J Echocardiogr*, vol. 11, no. 2, pp. 149–56, 2010.

[64] J. H. McGowan and J. G. Cleland, "Reliability of reporting left ventricular systolic function by echocardiography: a systematic review of 3 methods," *Am Heart J*, vol. 146, no. 3, pp. 388–97, 2003. Journal Article Review United States.

[65] T. Helle-Valle, J. Crosby, T. Edvardsen, E. Lyseggen, B. H. Amundsen, H.-J. Smith, B. D. Rosen, J. A. C. Lima, H. Torp, H. Ihlen, and O. A. Smiseth, "New noninvasive method for assessment of left ventricular rotation: speckle tracking echocardiography.," *Circulation*, vol. 112, pp. 3149–56, Nov. 2005.

[66] M. Shimizu, N. Sugihara, K. Shimizu, H. Yoshio, H. Ino, K. Nakajima, and R. Takeda, "Asymmetrical septal hypertrophy in patients with hypertension: a type of hypertensive left ventricular hypertrophy or hypertrophic cardiomyopathy combined with hypertension?," *Clinical cardiology*, vol. 16, pp. 41–6, Jan. 1993.

[67] J. S. Gottdiener, S. V. Livengood, P. S. Meyer, and G. A. Chase, "Should echocardiography be performed to assess effects of antihypertensive therapy? test-retest reliability of echocardiography for measurement of left ventricular mass and function," *Journal of the American College of Cardiology*, vol. 25, no. 2, pp. 424 – 430, 1995.

[68] Y. Bar-Shalom, X. Li, and T. Kirubarajan, *Estimation with Applications to Tracking and Navigation*. New York, NY, USA: John Wiley & Sons, Inc., 2001.

[69] S. Julier and J. Uhlmann, "A new extension of the Kalman filter to nonlinear systems," in *Int. Symp. Aerospace/Defense Sensing, Simul. and Controls*, pp. 182–193, 1997.

Chapter 2

Kalman filter based segmentation

Sten Roar Snare
Dept. Circulation and Medical Imaging, NTNU

In this background chapter, the segmentation scheme using Kalman filter and non-uniform rational B-splines is explained. The purpose of the chapter is to give the reader a more thorough walkthrough than what has been possible in the papers. Most of the descriptions in this chapter are based on [1–5], where also more general background information about state estimation and deformable models can be found.

2.1 Linear state space models

State space models are frequently encountered in control engineering. The generalized concept of a state space model is typically based on two separate models; the *kinematic model* and the *measurement model*. The kinematic model aims to describe how the process, characterized by its states, changes with time as a function of external inputs. The measurement model describes how the measurable variables, here denoted as $\mathbf{z}$, are related to the process states. Generally, considering the system states as $\mathbf{x}$, the input as $\mathbf{u}$, the input noise as $\mathbf{w}$ and the measurement noise as $\mathbf{v}$, a discrete system using the discrete time variable k, can be described by the *state equation* f and the *output equation* h:

$$\mathbf{x}_{k+1} = f(\mathbf{x}_k, \mathbf{u}_k, \mathbf{w}_k) \tag{2.1}$$

$$\mathbf{z}_k = h(\mathbf{x}_k, \mathbf{v}_k) \tag{2.2}$$

When f and h are linear in their states and inputs, the discrete system equations can be simplified as:

$$\mathbf{x}_{k+1} = \mathbf{F}_k\mathbf{x}_k + \mathbf{B}_k\mathbf{u}_k + \mathbf{w}_k \tag{2.3}$$

$$\mathbf{z}_k = \mathbf{H}_k\mathbf{x}_k + \mathbf{v}_k \tag{2.4}$$

$\mathbf{F}_k$ is called the "state matrix", $\mathbf{B}_k$ is the "input matrix" and $\mathbf{H}_k$ is the "output matrix". The system can thus be investigated by regular linear algebra. Typically, few

real-life systems are inherently linear. It is thus common to either simplify the system descriptions to achieve a sufficiently accurate linear system model or to linearize the nonlinear system model around a working point. The latter means that the system can be considered a linear process as long as the system states are within certain bounds.

By estimating the system states for each time step, it is possible to characterize the system behavior with time.

2.2 Kalman Filter

The topic of estimation deals with inferring values, which are unknown or random, from a set of observations which should be considered as random variables. If the variable to estimate is an unknown but deterministic number, the term *parameter estimation* is used. If the variable itself is a random variable, the common term is *random variable estimation*. A typical example is where one want to accurately estimate a random variable x from a set of related observations $z_1, z_2, \ldots, z_N$. The estimate $\hat{x}$ is then found by:

$$\hat{x} = \hat{x}(\mathbf{z}) = \phi(z_1, z_2, \ldots, z_N) \tag{2.5}$$

To calculate the estimator, ϕ, it is necessary to know the conditional probability $f(x|\mathbf{z})$ [5]. A Bayes procedure with an appropriate cost function can then be applied to achieve estimates of x. If the relation between x and z was linear, simpler techniques such as *linear mean square estimation* could be used. In case of ultrasound cineloop segmentation, the variables of interest, i.e. the system states, are constantly changing. The random variables are *dynamic*. Thus, different estimation schemes are required.

Problems with dynamic random variables were traditionally solved using Wiener filters. In Wiener filtering, the goal is to estimate a sequence $x[n]$ of a jointly stationary random process from observations of another related stationary random process $z[n]$. In case of the finite impulse response (FIR) Wiener filters, estimating $x[n]$ requires knowledge of $z[n]$ and the last P-1 values $z[n-1], z[n-2], \ldots, z[n-P+1]$, where P is the FIR filter length. The linear mean square optimal solution of the FIR filter can then be found using the discrete Wiener-Hopf Equations [5]. By formulating a recursive or causal infinite impulse response (IIR) version of the Wiener filter, the filter can be made shorter and more efficient. Solving the Wiener filter numerically can be computationally intractable, especially for larger or more complex systems. In addition, the Wiener filters inherently assume the signals to be noiselike, which often is an invalid assumption.

In 1960, R.E. Kalman presented a new way of formulating the minimum mean-square error (MMSE) filtering problem [4]. He used state space methods, and his recursive filter method was much more practical than the Wiener filter solutions commonly used at the time. Especially the ability to efficiently handle multiple input/output systems (MIMO), made the Kalman filter popular for instance in navigation problems. One of the early major achievements was the application in trajectory estimation in the Apollo space program, thus contributing to the first manned excursion to the moon. Since its introduction, the Kalman filter has found

numerous applications within space and military technology, communication systems, computer science, economy and control theory.

The Kalman filter estimates the internal states of linear dynamic systems, using series of noisy input measurements. The system models f and h are constrained to be linear, and the system noise terms $\mathbf{w}$ and $\mathbf{v}$ are assumed to be uncorrelated Gaussian zero mean processes. The Kalman filters are based on Markov chains, perturbed by Gaussian noise. In practice this means that the next state only depends on the current state. In mathematical notation, we may write:

$$f(\mathbf{x}_k, \mathbf{u}_k, \mathbf{w}_k) = \mathbf{F}_k\mathbf{x}_k + \mathbf{B}_k\mathbf{u}_k + \mathbf{w}_k \tag{2.6}$$

$$h(\mathbf{x}_k, \mathbf{v}_k) = \mathbf{H}_k\mathbf{x}_k + \mathbf{v}_k \tag{2.7}$$

$$\mathbf{w}_k \propto \mathcal{N}(0, \mathbf{Q}_k) \qquad \mathbf{v}_k \propto \mathcal{N}(0, \mathbf{R}_k) \tag{2.8}$$

$$E(\mathbf{w}_i\mathbf{w}_j^T) = \mathbf{Q}_i\delta_{i-j} \qquad E(\mathbf{v}_i\mathbf{v}_j^T) = \mathbf{R}_i\delta_{i-j} \tag{2.9}$$

$$E(\mathbf{w}_k\mathbf{v}_k^T) = 0 \tag{2.10}$$

The matrices $\mathbf{Q}_k$ and $\mathbf{R}_k$ are the covariance matrices corresponding to the second order statistics of the process and measurement noise values. As the input is Gaussian and the model is linear, the state and output will also be Gaussian and fully described by their means and covariances. The Kalman filter is a two-step process, where the first is the *prediction* step and the second is the *update* step. During the prediction step, a *prior* state estimate, $\bar{\mathbf{x}}_k$ is calculated at time k, before taking the measurements:

$$\bar{\mathbf{x}}_k = \mathbf{F}_k\hat{\mathbf{x}}_{k-1} + \mathbf{B}_k\mathbf{u}_k \tag{2.11}$$

$$\bar{\mathbf{P}}_k = \mathbf{F}_k\hat{\mathbf{P}}_{k-1}\mathbf{F}_k^T + \mathbf{Q}_k \tag{2.12}$$

The *posterior* state estimate, $\hat{\mathbf{x}}_k$, after taking the measurements is given as:

$$\mathbf{K}_k = \bar{\mathbf{P}}_k\mathbf{H}_k^T(\mathbf{H}_k\bar{\mathbf{P}}_k\mathbf{H}_k^T + \mathbf{R}_k)^{-1} \tag{2.13}$$

$$\hat{\mathbf{x}}_k = \bar{\mathbf{x}}_k + \mathbf{K}_k(\mathbf{z}_k - \mathbf{H}_k\bar{\mathbf{x}}_k) \tag{2.14}$$

$$\hat{\mathbf{P}}_k = (\mathbf{I} - \mathbf{K}_k\mathbf{H}_k)\bar{\mathbf{P}}_k \tag{2.15}$$

The matrix $\mathbf{K}_k$ is called the Kalman gain matrix and is used in the update step of both the state and covariance ($\mathbf{P}$) estimates. Note that except for the matrix inversion in the calculation of the Kalman gain, the Kalman filter calculation is completely linear. It is thus well suited for computer implementation.

The Kalman filter is also tightly connected to Bayesian tracking. To show this, we apply similar kinematic and measurement models as for the Kalman filter:

$$\mathbf{x}_{k+1} = f(\mathbf{x}_k, \mathbf{w}_k) \tag{2.16}$$

$$\mathbf{z}_k = h(\mathbf{x}_k, \mathbf{v}_k) \tag{2.17}$$

For simplicity, we have dropped the control input term, $\mathbf{u}$. The goal is to recursively estimate the states $\mathbf{x}_k$ from the available measurements $\mathbf{z}_k$. We want to use all available data up to time k, $\mathbf{z}_{1:k}$. In order to get the Bayesian solution, we thus need knowledge of the conditional density $p(\mathbf{x}|\mathbf{z}_{1:k})$. If the initial probability density function is known

and we assume the kinematic model to be a Markov process of order one, $p(\mathbf{x}|\mathbf{z}_{1:k})$ (the prior) can be found recursively using the Chapman-Kolmogorov equation:

$$p(\mathbf{x}_k|\mathbf{z}_{1:k-1}) = \int p(\mathbf{x}_k|\mathbf{x}_{k-1})p(\mathbf{x}_{k-1}|\mathbf{z}_{1:k-1})d\mathbf{x}_{k-1} \tag{2.18}$$

When the measurement in time step k becomes available, the prior probability density function can be updated according to Baye's rule:

$$p(\mathbf{x}_k|\mathbf{z}_{1:k}) = \frac{p(\mathbf{z}_k|\mathbf{z}_k)p(\mathbf{x}_k|\mathbf{z}_{1:k-1})}{\int p(\mathbf{z}_k|\mathbf{x}_k)p(\mathbf{x}_k|\mathbf{z}_{1:k-1})} \tag{2.19}$$

By assuming the posterior density at every time step to be Gaussian, and thus parameterized by the mean and covariance, it is possible to derive the Kalman filter. If $p(\mathbf{x_{k-1}}|\mathbf{z}_{k-1})$ is Gaussian, $p(\mathbf{x_{k-1}}|\mathbf{z}_k)$ is also Gaussian, provided that the kinematic and measurement models are linear and that the noise terms are drawn from a known Gaussian distribution. We may write:

$$\mathbf{x}_k = \mathbf{F}_k\mathbf{x}_{k-1} + \mathbf{w}_{k-1} \tag{2.20}$$
$$\mathbf{z}_k = \mathbf{H}_k\mathbf{x}_k + \mathbf{v}_k \tag{2.21}$$

The recursive Kalman filter algorithm can now be written as:

$$p(\mathbf{x}_{k-1}|\mathbf{z}_{1:k-1}) = \mathcal{N}(\mathbf{x}_{k-1}; m_{k-1|k-1}, P_{k-1|k-1}) \tag{2.22}$$
$$p(\mathbf{x}_k|\mathbf{z}_{1:k-1}) = \mathcal{N}(\mathbf{x}_k; m_{k|k-1}, P_{k|k-1}) \tag{2.23}$$
$$p(\mathbf{x}_k|\mathbf{z}_{1:k}) = \mathcal{N}(\mathbf{x}_k; m_{k|k}, P_{k|k}) \tag{2.24}$$

where:

$$m_{k|k-1} = \mathbf{F}_k m_{k-1|k-1} \tag{2.25}$$
$$\mathbf{P}_{k|k-1} = \mathbf{Q}_{k-1} + \mathbf{F}_k\mathbf{P}_{k-1|k-1}\mathbf{F}_k^T \tag{2.26}$$
$$m_{k|k} = m_{k|k-1} + \mathbf{K}_k(\mathbf{z}_k - \mathbf{H}_k m_{k|k-1}) \tag{2.27}$$
$$\mathbf{P}_{k|k} = \mathbf{P}_{k|k-1} - \mathbf{K}_k\mathbf{H}_k\mathbf{P}_{k|k-1}) \tag{2.28}$$

Here, $\mathcal{N}(x; m, P)$ means a Gaussian density with argument x, mean m and covariance P. In addition:

$$\mathbf{S}_k = \mathbf{H}_k\mathbf{P}_{k|k-1|}\mathbf{H}_k^T + \mathbf{R}_k \tag{2.29}$$
$$\mathbf{K}_k = \mathbf{P}_{k|k-1}\mathbf{H}_k^T\mathbf{S}_k^{-1} \tag{2.30}$$

These equations can be recognized as the Kalman filter. The Kalman filter is the *optimal solution* provided that the restrictions on the system are valid (linearity and Gaussianity) [2].

2.3 Extended Kalman Filter

As real-world systems seldom are purely linear, the Kalman filter can normally not be applied directly. By using an extended Kalman filter (EKF), the system is linearized around the current state estimate. This is achieved by calculating the Jacobian of f and h:

$$\mathbf{F}_k = \mathbf{J}_{\mathbf{x}} f(\mathbf{x}, \mathbf{u}, \mathbf{w}) = \left. \frac{\partial f(\mathbf{x}, \mathbf{u}, \mathbf{w})}{\partial \mathbf{x}} \right|_{\hat{\mathbf{x}}_k, \mathbf{u}_k, 0} \tag{2.31}$$

$$\mathbf{H}_k = \mathbf{J}_{\mathbf{x}} h(\mathbf{x}, \mathbf{v}) = \left. \frac{\partial h(\mathbf{x}, \mathbf{v})}{\partial \mathbf{x}} \right|_{\bar{\mathbf{x}}_k, 0} \tag{2.32}$$

The corresponding Kalman filter equations become:

$$\bar{\mathbf{x}}_k = f(\hat{\mathbf{x}}_{k-1}, \mathbf{u}_k, 0) \tag{2.33}$$

$$\bar{\mathbf{P}}_k = \mathbf{F}_k \hat{\mathbf{P}}_{k-1} \mathbf{F}_k^T + \mathbf{Q}_k \tag{2.34}$$

The *posterior* state estimate:

$$\mathbf{K}_k = \bar{\mathbf{P}}_k \mathbf{H}_k^T (\mathbf{H}_k \bar{\mathbf{P}}_k \mathbf{H}_k^T + \mathbf{R}_k)^{-1} \tag{2.35}$$

$$\hat{\mathbf{x}}_k = \bar{\mathbf{x}}_k + \mathbf{K}_k (\mathbf{z}_k - h(\bar{\mathbf{x}}_k, 0)) \tag{2.36}$$

$$\hat{\mathbf{P}}_k = (\mathbf{I} - \mathbf{K}_k \mathbf{H}_k) \bar{\mathbf{P}}_k \tag{2.37}$$

Except for the Jacobian computation, this is very similar to the regular Kalman filter.

2.4 Information space

In the typical applications of the Kalman filter, for instance in control engineering, the goal is often to estimate the states using as few measurements as possible. In case of image segmentation, the number of measurements can be high and exceed the number of states. In these cases, it can be advantageous to use a variant of the discrete Kalman filter, called the *information filter*. This formulation has the advantage of avoiding matrix inversion of the same size as the measurement covariance matrix. Instead, matrices with the same dimensions as the length of the state vector is inverted. The prediction step is unchanged from the discrete Kalman filter:

$$\bar{\mathbf{x}}_k = \mathbf{F}_k \hat{\mathbf{x}}_{k-1} + \mathbf{B}_k \mathbf{u}_k \tag{2.38}$$

$$\bar{\mathbf{P}}_k = \mathbf{F}_k \hat{\mathbf{P}}_{k-1} \mathbf{F}_k^T + \mathbf{Q}_k \tag{2.39}$$

The measurement update step is on the other hand different:

$$\hat{\mathbf{P}}_k^{-1} = \bar{\mathbf{P}}_k^{-1} + \mathbf{H}_k^T \mathbf{R}_k^{-1} \mathbf{H}_k \tag{2.40}$$

$$\hat{\mathbf{P}}_k^{-1} \hat{\mathbf{x}}_k = \bar{\mathbf{P}}_k^{-1} \bar{\mathbf{x}}_k + \mathbf{H}_k^T \mathbf{R}_k^{-1} \mathbf{z}_k \tag{2.41}$$

This requires an inversion step to get access to the updated state estimate and covariance:

$$\hat{\mathbf{P}}_k = (\bar{\mathbf{P}}_k^{-1} + \mathbf{H}_k^T \mathbf{R}_k^{-1} \mathbf{H}_k)^{-1} \tag{2.42}$$

$$\hat{\mathbf{x}}_k = \hat{\mathbf{P}}_k (\bar{\mathbf{P}}_k^{-1} \bar{\mathbf{x}}_k + \mathbf{H}_k^T \mathbf{R}_k^{-1} \mathbf{z}_k) \tag{2.43}$$

By expanding (2.43) and compare to the regular Kalman filter equations (2.14)(2.15), it can be seen that this filter uses a different Kalman gain:

$$\mathbf{K}_k = \hat{\mathbf{P}}_k \mathbf{H}_k^T \mathbf{R}_k^{-1} \tag{2.44}$$

Using this formulation, the measurements are all summed up into the *information matrix* $\mathbf{H^T R^{-1} H}$ and the *information vector* $\mathbf{H^T R^{-1} z}$.

If there are several independent scalar measurements at each time step, the information filter approach can be made even more efficient. If the scalar measurements are all independent, the measurement covariance matrix will be a *diagonal matrix* and its inverse will just be another diagonal matrix with all elements inverted:

$$\mathbf{R^{-1}} = \begin{bmatrix} r_1^{-1} & 0 & 0 \\ 0 & \ddots & 0 \\ 0 & 0 & r_N^{-1} \end{bmatrix} \tag{2.45}$$

Inserting this into the expressions for the information vector and matrix yields:

$$\mathbf{H^T R^{-1} z} = \sum_i \mathbf{h}_i r_i^{-1} z_i \tag{2.46}$$

$$\mathbf{H^T R^{-1} H} = \sum_i \mathbf{h}_i r_i^{-1} \mathbf{h}_i^T \tag{2.47}$$

Thus, the large matrix inversion is reduced to scalar divisions.

2.5 Deformable models

So far, state space models and suitable estimation methods have been presented. The remaining question is how to use this for image segmentation? Generally, image segmentation aims to separate the input image or image sequence into different parts or *segments*. In medical imaging, these segments typically corresponds to organs or anatomic structures. Deformable models contain the prior knowledge about the structure we are trying to segment out from the image. This can be size, shape, orientation and sometimes deformation modes. This prior knowledge can be utilized when conducting the segmentation.

We have applied so called *explicit models*. That means models where there is a direct mapping between parametric and spatial coordinates, depending on the model parameters. This is opposed to implicit models, such as level set models, where no such mapping exists. Explicit models are generally less complex than implicit models. In addition, it is often easier to add prior shape knowledge to explicit models. More accurately, we have applied Non-uniform rational B-splines.

2.6 Non-uniform rational B-splines

We have chosen to use Non-uniform rational B-splines (NURBS) as the foundation for our models. NURBS have become the de facto industry standard [6] for curve modeling. They have the advantage of being linear in their control points, and are thus suitable for the type of segmentation scheme we are applying. In addition, the possibility of adding weights to the various control points of the model makes it possible to preserve shape characteristics, even during large deformations. A k'th degree NURBS curve is defined by:

$$\mathbf{p}_l(u) = \frac{\sum_{i=0}^{n} N_{i,k}(u) w_i \mathbf{q_i}}{\sum_{i=0}^{n} N_{i,k}(u) w_i}, u_{low} \leq u \leq u_{high} \tag{2.48}$$

$N_{i,k}(u)$ are the k'th-degree B-spline basis functions. $\mathbf{q_i}$ are the spline control points and w_i are the weights of the NURBS curve. The parametric coordinate u is bounded by the constants u_{low} and u_{high}. We denote points on the NURBS curve as $\mathbf{p}_l(u)$. The rational basis functions are then written as:

$$b_{i,k}(u) = \frac{N_{i,k}(u) w_i}{\sum_{j=0}^{n} N_{j,k}(u) w_j}, u_{low} \leq u \leq u_{high} \tag{2.49}$$

which allows us to write:

$$\mathbf{p}_l(u) = \sum_{i=0}^{n} b_{i,k}(u) \mathbf{q_i}, u_{low} \leq u \leq u_{high} \tag{2.50}$$

The basis functions are defined on the knot vector:

$$U = u_{low}, \ldots, u_{low}, u_{k+1}, \ldots, u_{m-k-1}, u_{high}, \ldots, u_{high} \tag{2.51}$$

By letting the normal displacements of the NURBS control vertices be *local states*, $\mathbf{x}_l$, in the system description, local deformations can be estimated. A control point is then written as:

$$\mathbf{q}_i = \bar{\mathbf{q}}_i + x_{l,i} \mathbf{n}_i \tag{2.52}$$

where $\mathbf{n}_i$ is the normal displacement vector for the control vertex and $\bar{\mathbf{q}}_i$ is the mean/initial position of the control vertex. In some cases, it can be advantageous to let control points be fixed to their mean/initial position. By splitting the control points into sets of movable ($\mathcal{M}$) and static ($\mathcal{S}$) points, we can write:

$$\begin{aligned} \mathbf{p}_l(u) &= \sum_{i=\mathcal{M}} b_{i,k}(u)(\mathbf{q}_{0,i} + x_{l,i}\mathbf{n}_i) + \sum_{i=\mathcal{S}} b_{i,k}(u)\mathbf{q}_{0,i} \\ \mathbf{p}_l(u) &= T_l(\mathbf{x}_l, u) \end{aligned} \tag{2.53}$$

where we have introduced the term *local deformation model*, T_l, which relates points on the NURBS curve with the local states, $\mathbf{x}_l$.

Note that the points on the NURBS curve are defined by the parametric coordinate u. In order to draw a NURBS curve, a vector $\mathbf{u}$ of parametric coordinate values

must be decided for calculating the set of points composing the curve. The $\mathbf{u}$ vector is commonly defined to be uniformly distributed between $u = 0$ and $u = 1$. To improve readability, we will omit the parametric u coordinate from the equations in the following descriptions.

In order to orient and scale the NURBS curve into its final position, a similarity transform is applied to the $\mathbf{p}_l$ points. The similarity transform applies regular geometric transforms (translation, rotation and scale) [7]. During initalization, the transform parameters are found manually. Transform paramters can also be defined as dynamic and included as *global states*, $\mathbf{x}_g$, in the system equations. The total state vector then becomes $\mathbf{x} = \mathbf{x}_l + \mathbf{x}_g$. The similarity transform defines the *global deformation model*, T_g:

$$\mathbf{p} = T_g(\mathbf{p}_l, \mathbf{x_g}) \tag{2.54}$$

2.7 Kinematic model

The Kalman filter approach allows for complex kinematic models. If the motion of the structure of interest was strictly limited or predictable, this could be reflected in the motion model. Making assumptions about the movements of anatomic structures/organs can be dangerous when pathology is encountered. In our work we have thus chosen to use the motion model:

$$\mathbf{x}_{k+1} - \mathbf{x_0} = \mathbf{A}_1(\mathbf{x}_k - \mathbf{x_0}) + \mathbf{A}_2(\mathbf{x}_{k-1} - \mathbf{x_0}) + \mathbf{w}_k \tag{2.55}$$

This implies the prediction step of the Kalman filter to be just:

$$\bar{\mathbf{x}}_{k+1} - \mathbf{x}_0 = \mathbf{A}_1(\hat{\mathbf{x}}_k - \mathbf{x}_0) + \mathbf{A}_2(\hat{\mathbf{x}}_{k-1} - \mathbf{x}_0) \tag{2.56}$$

If $\mathbf{A}_2$ is set to zero, the basic interpretation is that the model is assumed stationary. If there was no measurement input, the model would then converge to its initial shape at an exponential rate defined by $\mathbf{A}_1$. The $\mathbf{A}_1$ matrix can thus be said to define the *regularization* of the model. By adjusting $\mathbf{A}_2$ or by adding more terms to the kinematic model, it is possible to introduce damping and other more complex motion modes.

2.8 Measurement inputs

In order to update the model, it is necessary to make measurements for use as input to the Kalman filter. The segmentation scheme currently utilizes the following measurements:

- Normal displacement edge detection
- Block matching

The measurement model in our system is nonlinear due to the local and global deformation models. The edge measurements aim to measure the correct position

of points on the contour $\mathbf{p}$. Measured values for $\mathbf{p}$ are related to the system states, $\mathbf{x}$, by T_l and T_g. The composite deformation model, T, includes both the local and global deformation models. The local deformation Jacobian matrix is derived from (2.53) and found by multiplying the displacement vectors with their respective basis functions:

$$\mathbf{J}_l = [b_{i_0}\mathbf{n}_{i_0}, b_{i_1}\mathbf{n}_{i_1}, \ldots] \tag{2.57}$$

This is precomputed and is computationally efficient.

The global T_g deformation model is directly applied to curve points, as in (2.54). For curve normals, the curve normal transformation rule must be applied [8, 9]:

$$\mathbf{n}_g = \left|\frac{\partial T_g(\mathbf{p}_l, \mathbf{x}_g)}{\partial \mathbf{p}_l}\right| \left(\frac{\partial T_g(\mathbf{p}_l, \mathbf{x}_g)}{\partial \mathbf{p}_l}\right)^{-T} \mathbf{n}_l \tag{2.58}$$

The overall Jacobian matrix is found using the chain-rule of multivariate calculus:

$$\mathbf{J}_g = \left[\frac{\partial T_g(\mathbf{p}_l, \mathbf{x}_g)}{\partial \mathbf{x}_g}, \frac{\partial T_g(\mathbf{p}_l, \mathbf{x}_g)}{\partial \mathbf{p}_l} J_l\right] \tag{2.59}$$

The edge measurements are made using *normal displacements*. N_p edge points are distributed around the NURBS model. For each edge point, it is searched for an intensity transition along a normal, $\mathbf{n}$, to the NURBS curve. This search can be performed in many ways, such as fitting a step function, finding the maximum intensity gradient or detecting an intensity plateau. The edge detector variants are discussed in Chapter 4. The distance from the edge point on the curve, $\mathbf{p}$, to the measured measured edge point, $\mathbf{p_{obs}}$, is called a *normal displacement* measurement z.

$$z = \mathbf{n^T}(\mathbf{p_{obs}} - \mathbf{p}) \tag{2.60}$$

A measure of edge confidence, r, is be found by taking the inverse of the intensity difference across the edge transition. This is use to weight the influence of each measurement. It is also possible to discard measurements that are too uncertain or differ significantly from the neighboring edge detectors. By only using normal displacements, the linearized measurement model for use in the Kalman filter becomes:

$$\mathbf{h^T} = \mathbf{n^T}\mathbf{J} \tag{2.61}$$

The block matching measurement is very similar to the edge detection. N_t points on the model are selected as start-out points for block matching. An offset normal vector, $\mathbf{o}$ of adjustable length is applied to locate centers for the block matching regions of interest. In frame k, a single kernel block is extracted around each center point. In frame *k+1* a kernel block of the same size is moved within a search window centered around the model center point from the previous frame, and a sum of absolute differences (SAD) fit to the previous frame is calculated. This defines the new kernel center position for frame *k+1*.

Denoting the normalized absolute error as ϵ, the kernel size as $l \cdot k$, the coordinates within the search window as (m, n) and the kernel frames at two consecutive time

points as X and Y, the SAD fit can be described as:

$$\epsilon_{m,n} = \sum_{i=1}^{l} \sum_{j=1}^{k} |X_{i,j} - Y_{i+m,j+n}| \tag{2.62}$$

By finding the (m, n) coordinates giving the smallest ϵ, the vector $\mathbf{b}$, pointing from the kernel position in frame k to frame $k+1$ is found. The normal component of $\mathbf{b}$ defines a normal displacement vector $\mathbf{z}_b$, and its length is used as a filter input in the same manner as for edge detection. This is illustrated in Fig. 2.1.

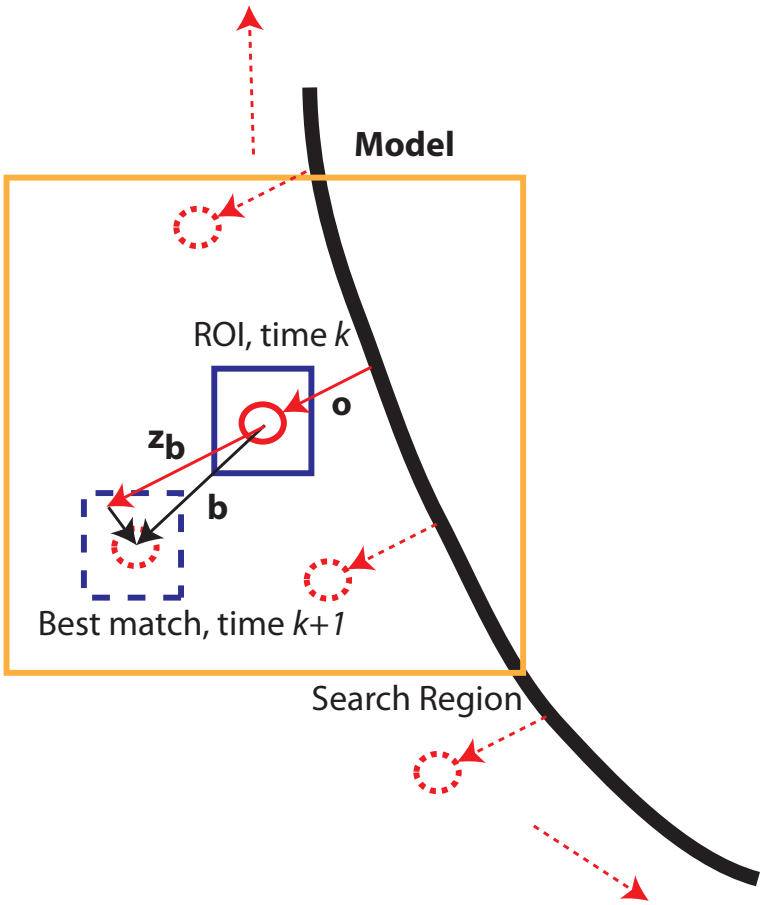

Figure 2.1: Illustration of block matching measurements used as input to the Kalman filter.

2.9 Combining models

It is also possible to combine multiple NURBS models and similarity transforms. By doing so, it is possible to develop complex models modeling multiple anatomical structures at the same time. By building a hierarchy of similarity transforms, each submodel may be defined to move (translate, scale, rotate) relative to the other submodels. Such a solution has been used in Chapters 4, 6 and 7. These projects have used four models and four similarity transforms. To keep the method descriptions at a sensible complexity level, and thus ensure readability, some implementation details of the combination process have been omitted in these manuscripts. In this section, the combination process is explained in detail using a simple example setup with two NURBS models (M_1 and M_2) and two similarity transforms ($\mathcal{T}_1$ and $\mathcal{T}_2$).

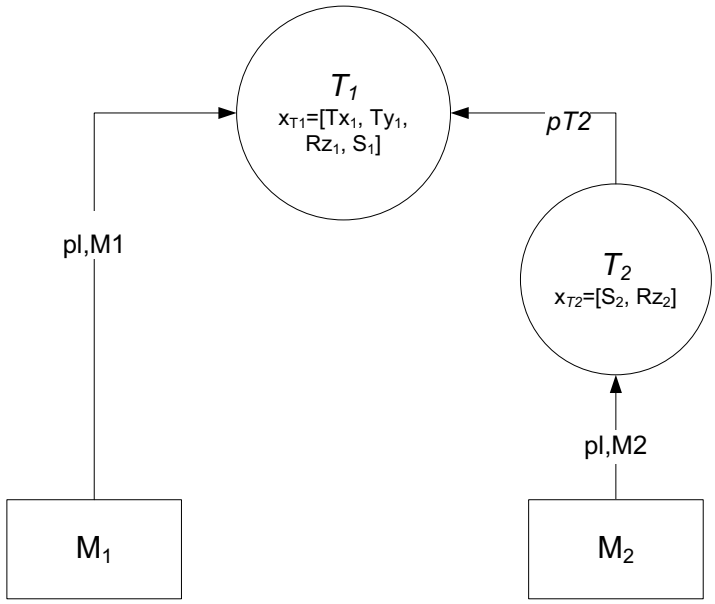

Figure 2.2: Example transform hierarchy using multiple models and transforms.

The models and transforms are combined by traversing the transform hierarchy in Fig.2.2 in a *depth first* manner. The composite state vector contains concatenated state vectors from all the models and transforms. For each of the models, a state vector containing normal displacements of the movable control points is defined. We denote these state vectors as $\mathbf{x}_{M1}$ and $\mathbf{x}_{M2}$. For the similarity transforms, state vectors containing the dynamic transform parameters are defined. We denote these vectors as $\mathbf{x}_{\mathcal{T}1}$ and $\mathbf{x}_{\mathcal{T}2}$. In this particular example, we say that model M_2 should be able to

scale (S) and rotate (Rz) relative to M_1. Additionally, M_1 and M_2 can both translate (Tx,Ty), rotate (Rz) and scale (S) together. In the example, we thus find:

$$\mathbf{x}_{\mathcal{T}1} = [Tx_1\, Ty_1\, S_1\, Rz_1]^T \tag{2.63}$$
$$\mathbf{x}_{\mathcal{T}2} = [S_2\, Rz_2]^T \tag{2.64}$$

By traversing the transform hierarchy depth first, the composite state vector becomes:

$$\mathbf{x} = [\mathbf{x}_{\mathcal{T}1}^T\, \mathbf{x}_{M1}^T\, \mathbf{x}_{\mathcal{T}2}^T\, \mathbf{x}_{M2}^T]^T \tag{2.65}$$

The measurement model will be different for the two models M_1 and M_2, as the latter has been processed by both similarity transforms. The points on each model prior to transformations ($\mathbf{p}_{l,M1}$ and $\mathbf{p}_{l,M2}$) are calculated as for the single model case, see (2.53). Likewise, the local Jacobians ($\mathbf{J}_{l,M1}$ and $\mathbf{J}_{l,M2}$) are found by (2.57). The overall Jacobian for model 1 becomes:

$$\mathbf{J}_{M1} = \left[\frac{\partial \mathcal{T}_1(\mathbf{p}_{l,M1}, \mathbf{x}_{\mathcal{T}1})}{\partial \mathbf{x}_{\mathcal{T}1}}, \frac{\partial \mathcal{T}_1(\mathbf{p}_{l,M1}, \mathbf{x}_{\mathcal{T}1})}{\partial \mathbf{p}_{l,M1}} \mathbf{J}_{l,M1}, \mathbf{0}, \mathbf{0}\right] \tag{2.66}$$

which is similar to what has been shown with one model and one transform, except for the zero-padding in the parts of the Jacobian related to the states not affecting M_1.

For model 2, it becomes more complex as two transforms are nested. We introduce the points $\mathbf{p}_{\mathcal{T}2} = \mathcal{T}_2(\mathbf{p}_{l,M2}, \mathbf{x}_{\mathcal{T}2})$ which are the points on model 2 after $\mathcal{T}_2$ but *before* $\mathcal{T}_1$. Using the chain rule again, the Jacobian can be written:

$$\begin{aligned}\mathbf{J}_{M2} = \Bigg[&\frac{\partial \mathcal{T}_1(\mathbf{p}_{\mathcal{T}2}, \mathbf{x}_{\mathcal{T}1})}{\partial \mathbf{x}_{\mathcal{T}1}}, \mathbf{0}, \frac{\partial \mathcal{T}_1(\mathbf{p}_{\mathcal{T}2}, \mathbf{x}_{\mathcal{T}1})}{\partial \mathbf{p}_{\mathcal{T}2}} \frac{\partial \mathcal{T}_2(\mathbf{p}_{l,M2}, \mathbf{x}_{\mathcal{T}2})}{\partial \mathbf{x}_{\mathcal{T}2}}, \\ &\frac{\partial \mathcal{T}_1(\mathbf{p}_{\mathcal{T}2}, \mathbf{x}_{\mathcal{T}1})}{\partial \mathbf{p}_{\mathcal{T}2}} \frac{\partial \mathcal{T}_2(\mathbf{p}_{l,M2}\mathbf{x}_{\mathcal{T}2})}{\partial \mathbf{p}_{l,M2}} \mathbf{J}_{l,M2}\Bigg]\end{aligned} \tag{2.67}$$

When knowing the Jacobians of the two models, edge and block measurements can be made. These measurements are assimilated to the information space for each model. All the information from all models is joined and used in the update step of the Kalman filter, using the composite state vector [10]. The same principles apply for cases with more models and transforms.

2.10 Implementation

In the preceding sections we have described all the building blocks needed to use the extended Kalman filter for image segmentation. The Kalman filter and the NURBS deformable model scheme has been implemented in a C++ based Real Time Contour tracking Library (RCTL), [1]. The model design has been conducted in Matlab (v2008a, The MathWorks, Inc.). For the scan assistance project, the application was implemented on a GE Vingmed E9 (GE Vingmed Ultrasound, Horten, Norway) cardiac ultrasound scanner. For the other projects, the applications were implemented using the WxWidgets framework [11].

2.11 Possible extensions

In this section some possible extensions to the current Kalman filter framework are presented. These are topics which could be subjects for further work.

Kalman smoother

A regular Kalman filter utilizes all information up to the current time stamp, k. Information about measurements from future time points is not used, even if such data is available. In the real-time setting, future measurements are, of course, never available. When working with post-processing algorithms, the whole measurement sequence can be used. In these cases, the Kalman filter may be a suboptimal choice. A Kalman smoother [3] does the state estimation based on all available measurements, both before and after k. The Kalman smoother is combining the results from a forward and backwards running Kalman filter [12], operating from $k = 1, \ldots, N$. We may write:

$$\hat{\mathbf{x}}_{k|N} = \hat{\mathbf{P}}_{k|N}\left(\hat{\mathbf{P}}_{k-}^{-1}\hat{\mathbf{x}}_{k-} + \hat{\mathbf{P}}_{k+}^{-1}\hat{\mathbf{x}}_{k+}\right) \tag{2.68}$$

$$\hat{\mathbf{P}}_{k|N} = \left(\hat{\mathbf{P}}_{k-}^{-1} + \hat{\mathbf{P}}_{k+}^{-1}\right)^{-1} \tag{2.69}$$

where $\hat{\mathbf{P}}_{k-}^{-1}$, $\hat{\mathbf{x}}_{k-}$ represents the backwards running estimate and $\hat{\mathbf{P}}_{k+}^{-1}$, $\hat{\mathbf{x}}_{k+}$ is the forwards running filter. The backwards filter is initialized with infinite covariance at the final time. The estimate for the final time is thus unchanged, while all earlier estimates are updated with measurements from future time points. This scheme can be utilized in post-processing schemes to improve the temporal regularization, which in this case regularizes both forwards and backwards in time. By wrapping around the data series, it can also be used to enforce a perfectly cyclic behavior.

Active shape models

Active shape models deal with models trained on a set of observations of the object of interest. The point distribution models introduced by Cootes and Taylor [13] capture the average shape and shape variations in a training set and use that knowledge to parametrize a model, using principal component analysis (PCA). Each model parameter thus represents an *orthogonal deformation mode*. This should be very efficient. By extending this framework to include a global pose transform, the resulting models are called Active Shape Models (ASM). Hansegård et al. [14] applied ASM with the Kalman filter by using a different motion model:

$$\mathbf{x}_{k+1} = \mathbf{A}_1(\mathbf{x}_k + +\mathbf{A}_2\mathbf{x}_{\mathbf{k-1}}) + \mathbf{B}_0\mathbf{w}_k \tag{2.70}$$

The purpose of this model is to use the matrices $\mathbf{A}_1, \mathbf{A}_2$ and $\mathbf{B}_0$ to adjust damping and inertia of the model, in order to get consistent temporal behavior of the model. More information about ASM and Kalman filter applications can be found in the literature [13–15].

Alternative measurements

In principle, many of the terms in the cost functions of active contours/cost minimization schemes could be applied as measurements to the Kalman filter.

Graph based edge detectors have been successfully applied with Kalman filters [16]. In these cases, the set of edge detection normals are treated as a graph. The optimum set of edge detection measurements for a given frame is given by a graph shortest path problem, where the cost of a transition is defined by gradient and smoothness operators. This opens up for a more robust way of identifying edges, but adds complexity as the edge measurements in each frame becomes a separate optimization problem.

Wavelet and phase based feature detection approaches have also been applied to Kalman filter schemes, such as in [17]. Wavelet analysis takes a sequence of image profiles and performs a wavelet decomposition. Then the profiles can be reconstructed using only the scales which contribute the strongest to the edge profile. The edge profiles are now denoised without extensive blurring. This is a favorable solution for detecting ridge-like edge profiles. The computation time is limited mainly by how the scales used for reconstruction are selected. Phase based approaches, such as in [18], calculate the phase of an edge profile using quadrature filters, such as Gabor wavelets. By investigating the output of these filters, the likely edge is found. In the Gabor filter case, a positive edge will be identified as a zero crossing from the even filter and a maximum in the odd filter.

References

[1] F. Orderud, *Real-time Segmentation of 3D Echocardiograms Using a State Estimation Approach With Deformable Models*. PhD thesis, Norwegian University of Science and Technology (NTNU), 2010.

[2] M. Arulampalam, S. Maskell, N. Gordon, and T. Clapp, "A tutorial on particle filters for online nonlinear/non-Gaussian Bayesian tracking," *IEEE Transactions on Signal Processing*, vol. 50, no. 2, pp. 174–188, 2002.

[3] Y. Bar-Shalom, X. Li, and T. Kirubarajan, *Estimation with Applications to Tracking and Navigation*. New York, NY, USA: John Wiley & Sons, Inc., 2001.

[4] R. Brown and P. Hwang, *Introduction to Random Signals and Applied Kalman Filtering*. Prentice-Hall International, Inc., 3 ed., 1996.

[5] C. W. Therrien, *Discrete random signals and statistical signal processing*. New Jersey: Prentice-Hall International, Inc., 1992.

[6] L. Piegl and W. Tiller, *The NURBS Book*. Springer Verlag, 1995.

[7] D. Hearn and P. Baker, *Computer Graphics with OpenGL*. Pearson Prentice Hall, 3rd ed., 2004.

[8] F. Orderud and S. I. Rabben, "Real-time 3d segmentation of the left ventricle using deformable subdivision surfaces," in *Computer Vision and Pattern Recognition, IEEE Computer Society Conference on*, (Los Alamitos, CA, USA), pp. 1–8, IEEE Computer Society, June 24-26 2008.

[9] A. Barr, "Global and local deformations of solid primitives," in *Proceedings of the 11th annual conference on Computer graphics and interactive techniques*, vol. 18, p. 30, ACM, 1984.

[10] F. Orderud, G. Kiss, and H. G. Torp, "Automatic coupled segmentation of endo- and epicardial borders in 3D echocardiography," *2008 IEEE Ultrasonics Symposium*, vol. m, pp. 1749–1752, Nov. 2008.

[11] wxWidgets [online]. http://www.wxwidgets.org/, October 2010.

[12] D. Fraser and J. Potter, "The optimum linear smoother as a combination of two optimum linear filters," *Automatic Control, IEEE Transactions on*, no. 31, pp. 387–390, 2002.

[13] T. Cootes, C. Taylor, D. Cooper, and J. Graham, "Training models of shape from sets of examples," in *Proc. British Machine Vision Conference*, vol. 9, p. 18, Citeseer, 1992.

[14] J. Hansegård, F. Orderud, and S. Rabben, "Real-time active shape models for segmentation of 3d cardiac ultrasound," in *Computer Analysis of Images and Patterns* (W. Kropatsch, M. Kampel, and A. Hanbury, eds.), vol. 4673 of *Lecture Notes in Computer Science*, pp. 157–164, Springer Berlin / Heidelberg, 2007.

[15] J. Hansegård, *Automated volume measurements in echocardiography by utilizing expert knowledge*. Phd thesis, University of Oslo, 2009.

[16] E. Dikici and F. Orderud, "Graph-Cut Based Edge Detection for Kalman Filter Based Left Ventricle Tracking in 3D+ T Echocardiography," in *Computers in Cardiology*, pp. 1–4, 2010.

[17] G. Jacob, J. Noble, C. Behrenbruch, A. Kelion, and A. Banning, "A shape-space-based approach to tracking mycordial borders and quantifying regional left-ventricular function applied in echocardiography," *IEEE Trans. Med. Imag.*, vol. 21, pp. 226–238, Mar 2002.

[18] G. Jacob, J. A. Noble, M. Mulet-Prada, and A. Blake, "Evaluating a robust contour tracker on echocardiographic sequences," *Med. Image Anal.*, vol. 3, pp. 63–75, 1999.

Chapter 3

Fast automated measurement of mitral annulus excursion using a pocket-sized ultrasound system

Sten Roar Snare[1], Ole Christian Mjølstad[1,2], Fredrik Orderud[3], Bjørn Olav Haugen[1,2] and Hans Torp[1]
[1] Dept. Circulation and Medical Imaging, NTNU
[2] Dept. Cardiology, St. Olav Hospital, Trondheim, Norway
[3] GE Vingmed Ultrasound, Horten, Norway

We present a fast automatic method for mitral annulus excursion measurement using pocket-sized ultrasound (PSU). The motivation is to provide PSU users with a rapid measurement of cardiac systolic function. The algorithm combines low frame rate tolerance, computational efficiency and automation in a novel way. The method uses a speckle tracking scheme, initialized and constrained by a deformable model. A feasibility study using 30 apical four-chamber PSU recordings from an unselected patient population revealed an error of (mean ± SD) -1.80 ± 1.96mm ($p < 0.001$), when compared to manual anatomic m-mode analysis using laptop scanner data. When only septal side excursion was measured, the mean error was $-0.27 \pm 1.89mm$ ($p < 0.001$). The accuracy is comparable to previously reported results using semi-automatic methods and full-size scanners. The computation time of 3.7ms/frame on a laptop computer suggests a real-time implementation on a PSU device is feasible.

3.1 Introduction

[1]The development of Hand-carried ultrasound (HCU) has branched in two directions [1]. Whereas one direction aims to close the performance gap between HCU and full-size scanners, the other direction heads towards miniaturization. Recently, several commercial equipment manufacturers have launched pocket-sized ultrasound (PSU) devices capable of echocardiography, such as Siemens/Acuson P10 and GE Healthcare Vscan. The advent of truly pocket-sized equipment, opens up for new applications of ultrasound.

Cardiac examination is one of the clinically interesting applications for portable ultrasound, and this topic has already been investigated in several studies [1–6]. Atherton [2] stated that HCU is promising as a screening tool for asymptomatic subjects, but that the specificity is high only for experienced sonographers. We believe that due to the smaller size and lower cost, PSU units will more often be operated by inexperienced users and would benefit from having applications actively *aiding* these users in detecting heart disease. One way of doing this, could be to include automatic or semi-automatic cardiac measurements.

Ejection fraction (EF) is the most commonly used measurement for global systolic left ventricular function. Correct measurement of EF using 2D ultrasound is difficult and requires good visibility of all segments of the left ventricle (LV). The mitral annulus excursion (MAE) measurement requires good image quality only in the base and has shown to correlate with EF [7–10].

Several recent papers [7, 8, 11, 12] address the topic of semi-automatic measurement of MAE. Pocket-sized scanners typically have a much lower frame rate than regular scanners, which is a challenge for speckle tracking approaches. One paper has addressed low frame rate tracking [11], but no published algorithm has been shown to combine computational efficiency with low frame rate tolerance. We propose a novel, highly efficient, method for measurement of MAE on low frame rate (20Hz) ultrasound data from a pocket-sized scanner, *combining* speckle tracking and model-based segmentation of the left ventricle. The system is designed to be fully automatic and capable of real-time operation on pocket-sized ultrasound scanners. In the following we will present the method and provide results from a feasibility study.

3.2 Materials and Method

The algorithm has two main parts. The first part is the Kalman filter segmentation, which uses a Kalman filter to fit a deformable model of the LV to the image data. The second part is a speckle tracker, which is a variant of the commonly used sum of absolute differences (SAD) speckle tracker, using correlation weighted spatial averaging. The Kalman filter segmentation is used to initalize the speckle tracker, and to prevent tracking drift. We are using a weighted averaging scheme combining the SAD fit and the movement of the deformable model, to derive the new kernel points for

[1]The reference style in this manuscript has been modified from (name,year) to numbered references, to comply with the rest of the thesis.

the speckle tracker. The system either loads cartesian data directly or beamspace data from dicom files. In the latter case, an in-house scan conversion is used to generate cartesian image data.

3.2.1 Kalman filter segmentation

The Kalman filter segmentation is founded on the work in [13, 14]. We have used non uniform rational B-splines (NURBS) to create the deformable model. NURBS were chosen due to their flexibility and versatility. Use of Kalman filter for 2D segmentation using B-splines has been published in [15–19]. As system states the Kalman filter uses pose parameters and normal displacements of the NURBS control points. The motion model in the filter is simple, and the prediction is based on the previous step only. Edge detection measurements, as well as block matching, are used as measurement input to the Kalman filter. By assimilating the measurements into information space, an efficient implementation is possible. A detailled description of the Kalman filter segmentation scheme can be found in 3.5.

The result of the Kalman filter segmentation is an efficient and robust model of the LV. By selecting model points in the basal region of the model, it is now possible to approximate MAE using the model only. Initial tests proved this approach to be inaccurate. Especially around end-diastole, the model was not able to accurately track the movement of the atrioventricular (AV) plane when facing challenging image quality. Our solution has been to use the Kalman filter model as initialization and drift compensation for a regular speckle tracker. The purpose is to combine the accuracy of speckle tracking with the robustness and low frame rate tolerance of the Kalman filter.

3.2.2 Speckle Tracking

AV plane speckle tracking should be done around the hinge point for the mitral valve leaflets. In practice, this region can be very blurred. When a clinician is selecting a point for speckle tracking, he should select a bright speckle in an anatomically correct position. It is challenging to automate this selection process. We have chosen to first locate an assymetric region of interest (ROI) at the model corner points, and then do a search for the brightest pixel within that ROI. Since we are using data from both pocket-sized and laptop systems, two different setups are required. Values for the laptop system are put in parentheses. The ROI size is 10x11mm (5x5mm) and centered 1mm (1mm) left and 3mm (1.5mm) down from the septal corner point, considering an apical 4 chamber view. On the lateral side, the ROI is centered 4mm (2mm) to the right and 3mm (3mm) down from the corner point.

For simplicity, we will now only consider one point at the time. We denote the detected initial tracking point, lateral or septal, as $\mathbf{x}_{0,S}$. The subscript **S** means "Speckle". We now search for the closest point on the deformable model and denote it as $\mathbf{p}_{0,K}$. The subscript **K** means "Kalman". The vector from the point on the model to the tracking point is denoted **b**. Using the parametric coordinate of $\mathbf{p}_{0,K}$ and the deformable model, we will always have knowledge about $\mathbf{p}_{i,K}$, where i means frame

number. See Fig. 3.1 for an illustration. We find the corresponding Kalman filter based tracking point for all frames:

$$\mathbf{x}_{i,K} = \mathbf{p}_{i,K} + \mathbf{b} \tag{3.1}$$

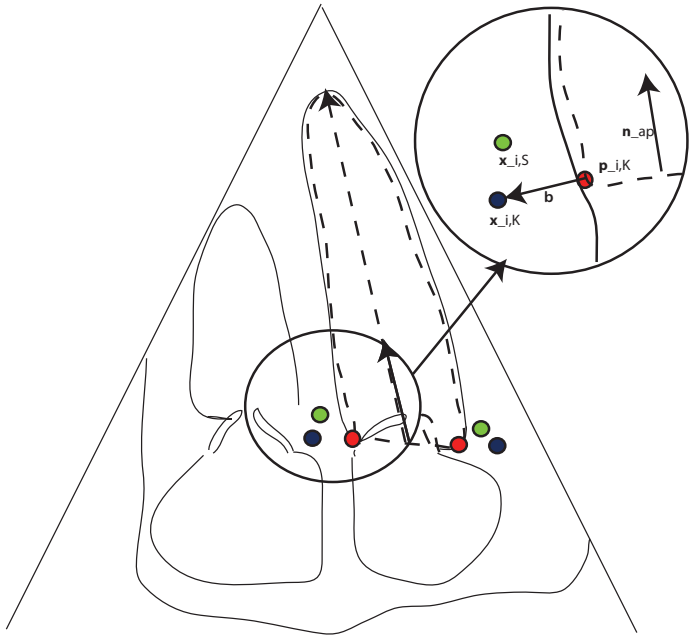

Figure 3.1: Figure illustrating the Kalman model mitral annulus (MA) points, $\mathbf{p}_{i,K}$ and the corresponding Kalman tracking points $\mathbf{x}_{i,K}$. $\mathbf{x}_{i,S}$ denote the final speckle tracking points. Also note the vector from the atrioventricular plane to the cardiac apex, $\mathbf{n_a p}$ and the vector $\mathbf{b}$ from the model MA point to the model-based tracking point.

In a 3x3mm (4x4mm) region around $\mathbf{x}_{i,S}$, $N_{avg}-1$ surrounding points for averaging are selected. The N_{avg} points become the center points for the block matching kernels in frame i. We have chosen to use 26 (36) points for averaging. Each kernel has a size of 5x6mm (5x5mm). Search windows are 7x14mm (8x9mm). A SAD fit of the kernels results in N_{avg} displacement vectors. These are combined using the weighted average of the N_{avg} displacement vectors. The weights are calculated from the Pearsons sample correlation coefficient between the kernel and the best fit for each of the averaging points. This means that tracking points where there is high correlation between the kernels in consecutive frames, get priority. Tracking points having a correlation coefficient below a threshold, $T_c = 0.4$, are discarded. The average displacement vector is denoted $\bar{\mathbf{d}}_{d,i}$. The new position of the tracking points $\mathbf{x}'_{i,S}$ becomes

$$\mathbf{x'_{i,S}} = \mathbf{x_{i-1,S}} + \bar{\mathbf{d}}_{\mathbf{d,i}}, i = \{1, 2, \ldots\} \tag{3.2}$$

In regular speckle tracking, the standard solution would be to set $\mathbf{x_{i,S}} = \mathbf{x'_{i,S}}$, add points for averaging and repeat the process. This would be sensitive to drift and is likely to fail on low frame rate loops. We thus combine this result with the model from the Kalman filter segmentation.

Three main criteria exist for this combination process:

- Speckle tracking results should be given priority as long as $\left\|\mathbf{x_{i,K}} - \mathbf{x'_{i,S}}\right\|$ is small or moderate.
- When $\left\|\mathbf{x_{i,K}} - \mathbf{x'_{i,S}}\right\|$ is large, the Kalman filter derived points should rapidly pull the speckle tracker towards the correct region.
- The combination should be a smooth process to avoid jumps and discontinuities in the result.

The chosen solution is to use a weighted sum of $\mathbf{x_{i,K}}$ and $\mathbf{x'_{i,S}}$:

$$\mathbf{x}_{i,S} = a * \mathbf{x}_{i,K} + (1 - a) * \mathbf{x'}_{i,S} \tag{3.3}$$

The weighting function a is chosen as an exponential function

$$a = min\{exp(C * (\left|\left\|\mathbf{x_{i,K}} - \mathbf{x'_{i,S}}\right\| - T\right|), 1\} \tag{3.4}$$

The constant C has been set to 650 and T is selected to be 0.010. The resulting weighting function is displayed in Fig. 3.2. Using this setup, it can be seen that as long as the difference between the Kalman filter and speckle tracker defined points is less than 5mm, the process is controlled mainly by the speckle tracker. When approaching a difference of 1cm, the weight is rapidly, but smoothly, shifted to the Kalman filter based values. After 1cm, the new kernel positions are solely defined by the Kalman filter segmentation.

The tracking process is repeated for all frames $[i + 1, i + 2, \ldots]$.

3.2.3 MAE value

The coordinates of the tracking points $\mathbf{x}_{i,S}$ are used to find MAE. Using the deformable model, a unity vector $\mathbf{n}_{ap}$, pointing from the center of the AV plane to the cardiac apex is calculated. Taking the inner product of this vector and the average position of the two tracking points, yields a distance measure for the mitral annulus towards the apex, y_{MAE}:

$$y_{MAE_i} =< \bar{\mathbf{x}}_{\mathbf{i,S}}, \mathbf{n}_{ap} > \tag{3.5}$$

Considering one heart cycle only, the mitral annlus excursion is found as, $MAE = max\{y_{MAE_i}\} - min\{y_{MAE_i}\}$. Fig. 3.3 shows a flowchart providing an overview of the overall tracking system.

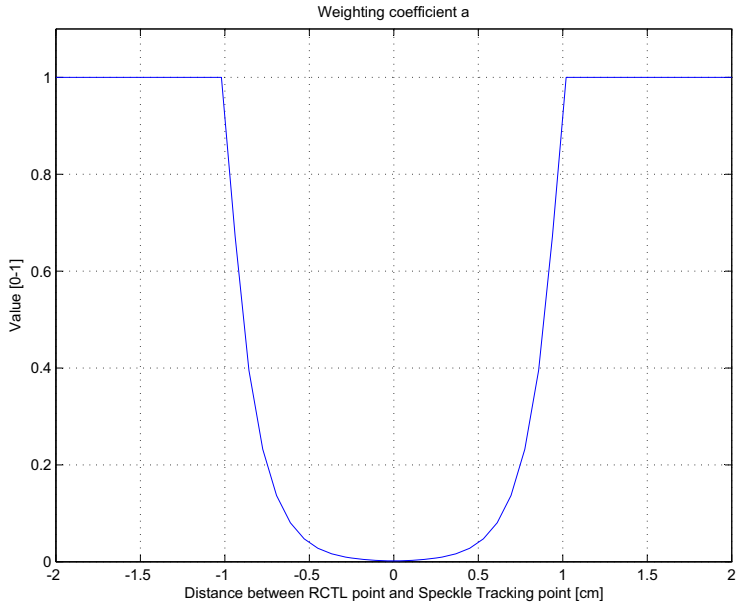

Figure 3.2: Weighting function for combining speckle tracking and Kalman filter results. As long as the difference between the Kalman based tracking point $\mathbf{x}_{i,K}$ and the speckle tracking point $\mathbf{x}_{i,S}$ is less than 5mm, the position of the next tracking kernel is mainly based on the speckle tracking. If the difference is more than 1cm, the parametric model is used to position the new kernel.

3.2.4 Manual corrections

Although the algorithm is designed for automatic operation, some optional manual interaction is supported. This covers manual re-initialization of the tracking points and model position. In addition, the lateral tracking point can be disabled, which can be relevant in a few hard-to-image patients. We will present both fully automatic and semi-automatic results.

3.2.5 Acquisition of data

The algorithm was tuned using recordings from a pocket-sized ultrasound (PSU) scanner (Vscan, GE Vingmed Ultrasound, Horten, Norway) and a commercially available high-end scanner (Vivid 7, GE Vingmed Ultrasound, Horten, Norway). Test data was acquired from 30 patients (age 72.8 ± 10.8 years; 60% men), who previously either had suffered a myocardial infarction, had known systolic heart failure or known arterial hypertension. An ethical committee aproval was obtained, and informed consent for the study was obtained from all human subjects per the WORLD Medical

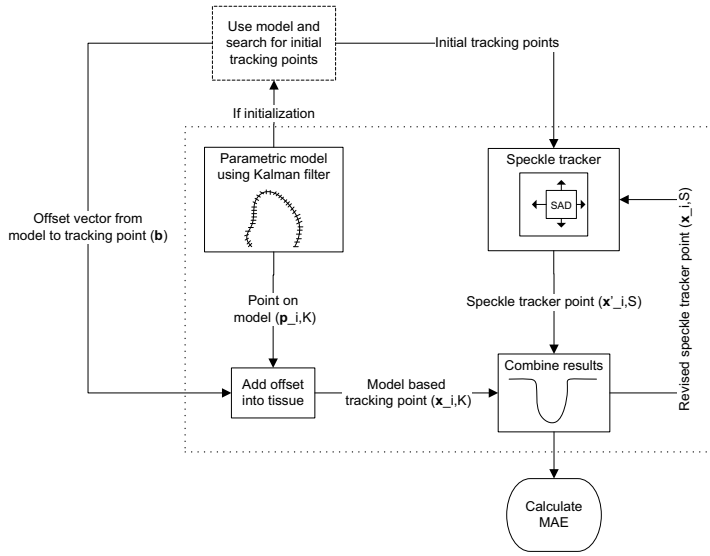

Figure 3.3: Flowchart illustrating the main components of the mitral annulus excursion measurement system. A parametric model is fitted to the image data using a Kalman filter. Upon initialization of the speckle tracker, the model is used to calculate initial tracking points and a vector, $\mathbf{b}$, pointing from the model to these initial tracking points. After initialization, the speckle tracker and Kalman filter is run in parallel. For each frame, the vector $\mathbf{b}$ is used to calculate new tracking kernel points based on the movement of the deformable model, $\mathbf{x}_{i,K}$. These results are combined with the sum of absolute differences (SAD) fit from the speckle tracker, $\mathbf{x}'_{\mathbf{i,S}}$, yielding the corrected tracking points $\mathbf{x}_{i,S}$. These points are used for calculation of mitral annulus excursion (MAE), as well as for new speckle tracker kernel points in the next frame.

Association Declaration of Helsinki: Ethical principles for medical research involving human subjects. A cardiologist collected the data from the apical four-chamber view using a commercially available laptop scanner (Vivid i, GE Vingmed Ultrasound, Horten, Norway) and a PSU system (Vscan, GE Vingmed Ultrasound, Horten, Norway). Following American Society of Echocardiography (ASE) nomenclature [20] the laptop scanner is in the following denoted as the hand-carried ultrasound (HCU) device, even if the image quality and user interface of this particular HCU device is close to that of a full size scanner.

3.2.6 Analysis

The cardiologist measured MAE on the HCU data using anatomic m-mode in the EchoPac software package (GE Vingmed Ultrasound, Horten, Norway). Both the

septal and lateral sides were measured. One HCU recording was considered unsuitable for speckle tracking and excluded from the analysis. The algorithm was thus tested on 30 patients from the PSU device and 29 patients from the HCU system.

The algorithm was tested offline on a standard laptop computer. The fully automatic solution was tested by running the algorithm using a batch script. One complete cardiac cycle must be analyzed to calculate MAE. In addition, the Kalman filter must have converged before initializing the speckle tracking points. This normally occurs within the first 10 frames. For convenience, each recording was run for two complete cycles. At the end of the second cycle, the MAE value was automatically stored together with an image and movie of the tracking. We tested both to use the septal point separately and to use the average of the septal and lateral points for calculating the MAE value. The analysis was run using both PSU and HCU data.

Semi-automatic operation was tested by letting a second cardiologist, blinded for the reference measurements, operate the algorithm while allowing for manual corrections. Semi-automatic operation using the septal point only was not tested. But as the clinician had the option of manually turning off the lateral point, some of the reported semi-automatic MAE values were in reality based on medial tracking only. In these cases we chose not to adjust the reference value accordingly. This has the consequence that in cases where the semi-automatically reported MAE value in reality was based on the septal excursion only, the reference value was still defined as the average of the lateral and septal anatomic m-mode measurements. The cardiologist noted what changes he did and rated the image quality as good or poor. The image quality was rated good in 19 (61.3%) cases using PSU and in 20 (69.0%) cases using HCU.

After testing for normality, the automatic results and the anatomic m-mode references were compared using paired t-test and Pearson's correlation coefficient. Bland-Altman plots and scatter plots of the results were produced. The mean and maximum absolute errors were calculated. The null hypothesis was that there was no difference between the automatic method and the manual m-mode reference. To assess the value of user interaction, the results from the semi-automatic analysis were also analyzed.

3.3 Results

Two examples of excursion measurements, one from the PSU and one from the HCU system, are shown in Fig. 3.4 and Fig. 3.5.

The results from the automatic and semi-automatic analysis are presented in Table 3.3. Figures 3.6 and 3.7 present scatter plots for the PSU device using respectively both points and the septal point only. Bland-Altman plots are provided in Figures 3.8 and 3.9. For the HCU device, scatter plots are found in Figures 3.10 and 3.11, while Bland-Altman plots are found in Figures 3.12 and 3.13. For the semi-automatic analysis using PSU data, the cardiologist let the algorithm process 15 of the 30 recordings fully automatic. For the HCU data, only 5 of the 29 were processed fully automatic. The manual corrections are summarized in Table 3.3.

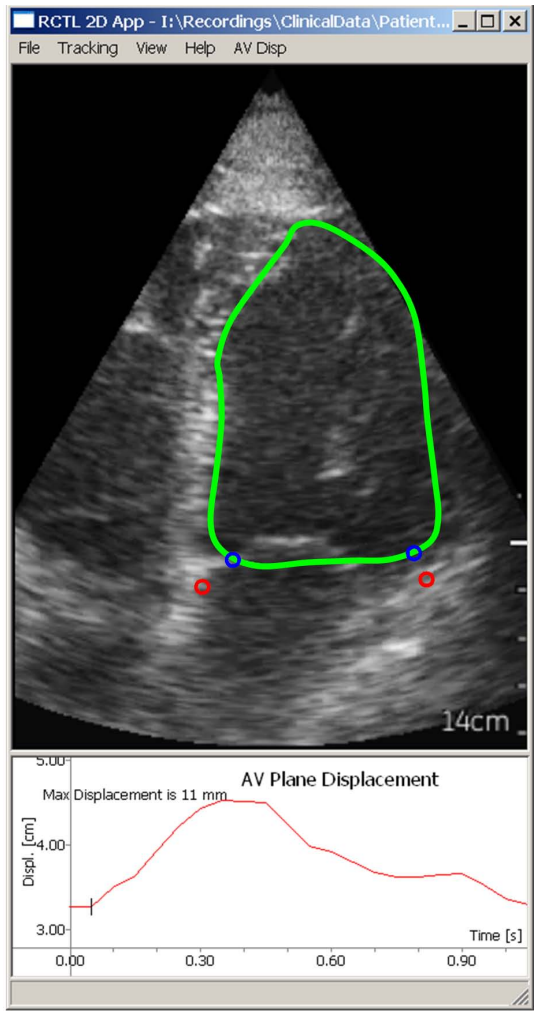

Figure 3.4: Example segmentation from a pocket-sized ultrasound recording. The circles in the basal region of the model correspond to $\mathbf{p}_{i,K}$ and the ones in the myocardium corresponds to $\mathbf{x}_{i,S}$.

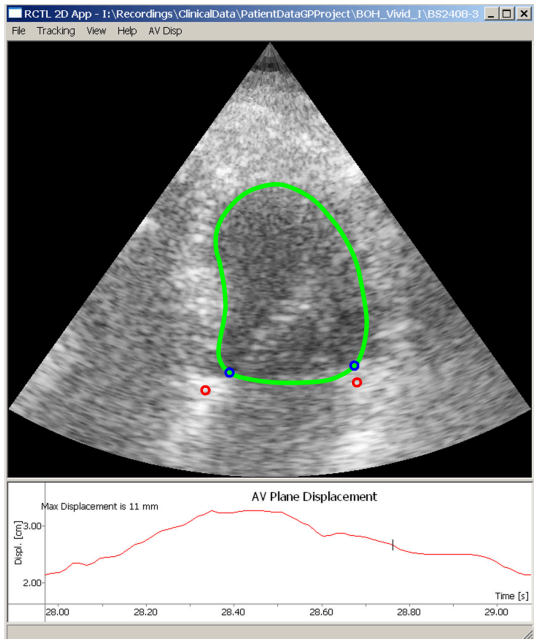

Figure 3.5: Example segmentation from a hand-carried ultrasound recording (same patient as in Fig. 4). The circles in the basal region of the model correspond to $\mathbf{p}_{i,K}$ and the ones in the myocardium corresponds to $\mathbf{x}_{i,S}$.

The Kalman tracking used on average 2.5ms/frame and the speckle tracking 1.2ms/frame on a regular laptop computer (1.17GHz Dual Core, 2GB ram). The frame rate for the PSU data was on average 20 frames per second and 55 frames per second for the HCU data.

3.4 Discussion

The results from the analysis of PSU data suggest that fully automatic assessment of MAE using a pocket-sized ultrasound scanner is feasible. The lateral tracking is most challenging. When the average of the septal and lateral excursions is used to calculate MAE, the lateral point introduces a negative bias of 1.8mm. By tracking the septal point only, the negative bias is reduced to 0.27mm and is no longer statistically significant. This is similar to the result in Hayashi et al. [21], who reported a statistically significant difference of (mean $\pm$ SD) 1.94 ± 3.96mm between anatomic m-mode measurements and speckle tracking on the lateral side. They did not get significant bias on the septal side. We found the 95% confidence interval of the error to be -2.53 to -1.07mm when using both points and a narrower -0.97 to 0.44mm when only using the septal point. The maximum absolute error was reduced from 5.5 to

Table 3.1: Table summarizing the mitral annulus excursion measurement results using pocket-sized ultrasound (PSU) and hand-carried ultrasound (HCU) data. Both fully automatic and semi-automatic results are presented. In case of automatic analysis, the results when only using septal measurements are also provided. The results are presented as maximum absolute error, mean absolute error, paired t-test results (mean ± SD), Peearsons correlation coefficient and 95% mean confidence interval. All values, except the correlation coefficient, are measured in millimetres.

Method	**Max Abs. Error [mm]**	**Mean Abs. Error [mm]**	**Paired t-test (mean±SD) [mm]**	**Pearsons r**	**95% Mean Confidence Interval. [mm]**
PSU	5.5	2.2	-1.80 ± 1.96 ($p < 0.001$)	0.62 ($p < 0.001$)	$[-2.53, -1.07]$
PSU(Septal)	3.0	1.6	-0.27 ± 1.89 ($p = 0.446$)	0.61 ($p < 0.001$)	$[-0.97, 0.44]$
HCU	5.5	2.1	-1.17 ± 2.32 ($p = 0.010$)	0.61 ($p < 0.001$)	$[-2.03, -0.30]$
HCU(Septal)	4.0	1.4	-0.13 ± 1.78 ($p = 0.684$)	0.69 ($p < 0.001$)	$[-0.80, 0.53]$
PSU(Semi-aut.)	4.5	2.0	-1.57 ± 1.72 ($p < 0.001$)	0.69 ($p < 0.001$)	$[-2.21, -0.92]$
HCU(Semi-aut.)	4.0	1.8	-1.40 ± 1.69 ($p < 0.001$)	0.64 ($p < 0.001$)	$[-2.04, -0.75]$

Table 3.2: Table listing the manual corrections performed during semi-automatic analysis using the 30 pocket-sized ultrasound (PSU) recordings and the 29 hand-carried ultrasound (HCU) recordings. The values are presented as number of cases and percentage.

	PSU	**HCU**
Uncorrected [Cases (%)]	15 (50%)	5 (17%)
Lateral point disabled [Cases (%)]	7 (23%)	7 (24%)
Lateral point adjusted [Cases (%)]	4 (13%)	10 (34%)
Septal point adjusted [Cases (%)]	8 (27%)	12 (41%)
Model adjusted vertically [Cases (%)]	3 (10%)	6 (21%)
Model adjusted horizontally [Cases (%)]	3 (10%)	4 (14%)

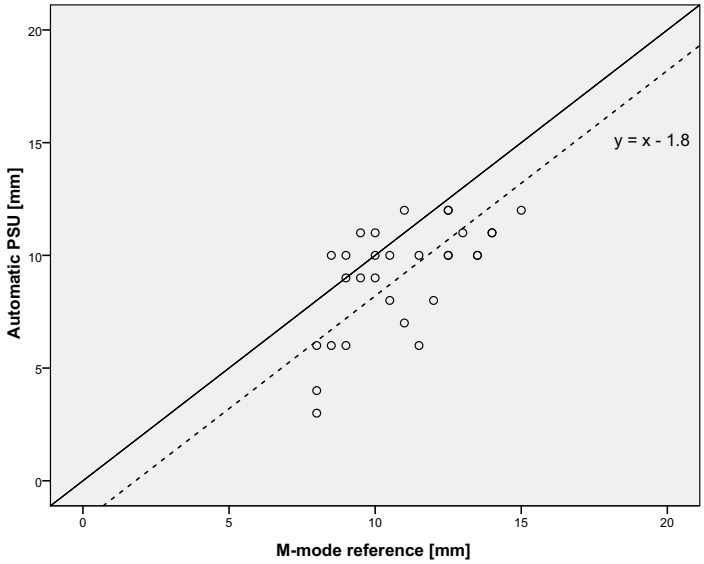

Figure 3.6: Scatter plot with the pocket-sized ultrasound (PSU) results along the vertical axis and the m-mode reference values along the horizontal axis. The solid line is the reference unity line (y = x). The dashed line represents the unity line corrected for the negative bias of 1.8mm (y = x - 1.8).

3mm when only the septal point was used. The poor lateral tracking is probably caused by inferior image quality on the lateral side, which often suffers from dropouts and out-of-plane motion.

Judging from the results, the algorithm performance seems less sensitive to frame rate. By using HCU data the overall results did improve, but the differences were almost negligble. We had expected a larger improvement for the HCU device. Several of the HCU images suffered from very high gain in the base. This caused saturation and poor visibility of the speckle pattern. Unfortunately, the saturation was also present in the raw data, so we could not resolve the problem offline. This may have influenced the tracking performance when the algorithm was used with HCU data.

When the algorithm was operated semi-automatically, the operator frequently corrected both the model and tracking point initialization. Only 50% of the PSU recordings and 17% of the HCU recordings were processed without interaction. The most frequent corrections for the PSU data were disabling the lateral point (23%) and correction of the septal point (24%). For the HCU data, both the lateral and septal points were frequently adjusted. The lateral point was disabled in 24% of the cases. In case of HCU data, the frequent repositioning of the tracking points can be partly explained by the gain problems in the base, as the clinician was instructed to

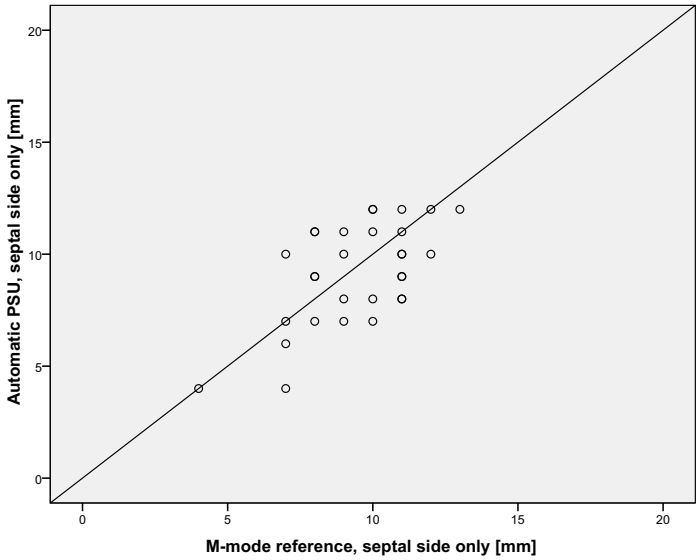

Figure 3.7: Scatter plot with the pocket-sized ultrasound (PSU) results, using only the septal value, along the vertical axis and the septal m-mode reference values along the horizontal axis. The solid line is the reference unity line (y = x).

move tracking points away from saturated regions. The correction process was very straightforward, only using two mouse clicks. It may be that the clinician did more of an optimization than a correction of the tracking points. This is supported by the limited gain from the user interaction. By introducing manual interaction, the maximum error was reduced from 5.5mm to 4.5mm for the PSU device and from 5.5 to 4mm for the HCU device. We also registered a drop in the mean absolute error (0.2mm for PSU and 0.3mm for HCU data) and the standard deviation of the error. It seems that the main effect of manual interaction is reduction of outliers. It is questionable whether these minor improvements can justify manual interaction when implemented on a PSU device.

The correlation coefficients range from $r = 0.61$ to $r = 0.69$ and are statistically significant. Hayashi et al. [21] reported a $r^2 = 0.55(r = 0.74)$ correlation between anatomic m-mode and speckle tracking for the septal side and a non-significant value for the lateral side. This is comparable to our results. We believe that the correlation coefficients would benefit from having data with a wider range in the excursion values. Our set has a value range from 6 to 14mm. Eto et al. [12] presented values ranging from 1.9 to 24.6mm and achieved a correlation of $r = 0.86$ when comparing their semi-automatic speckle tracking approach with manual atrioventricular plane tracing in 3D echo. They also reported a difference of (mean $\pm$ SD) $2.5 \pm 1.8mm$ compared

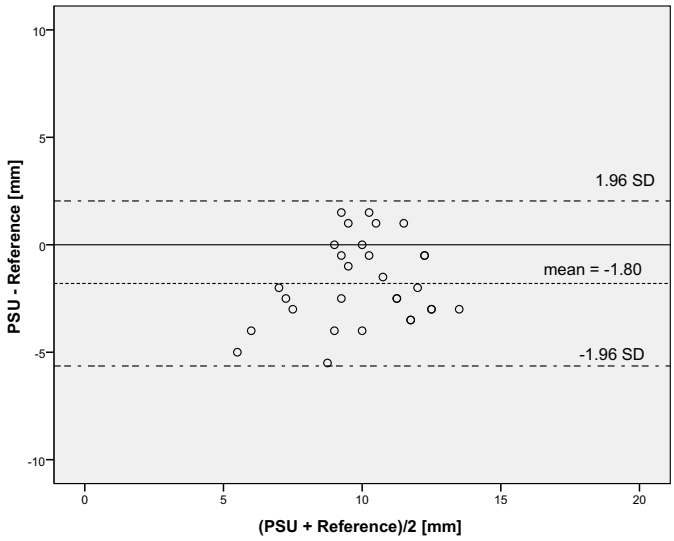

Figure 3.8: Bland-Altman plot of the measurement difference betweeen the automatic algorithm using pocket-sized ultrasound (PSU) and manual m-mode measurement on hand-carried ultrasound data (HCU). The dashed line represents the bias in the data, while the dash-dotted lines represent the 95% limits of agreement.

to the manual tracing.

The standard deviation of the error is relatively high, which can also be seen from the Bland-Altman plots. This can have several reasons. The size of the dataset is limited, and the patients were not from a healthy population. All patients had a previous history of myocardial infarction, known hypertension or systolic heart failure. The image quality was on the low side of the quality scale. The cardiologist judged 38.7% of the PSU recordings and 31.0% of the HCU recordings as having "Poor" image quality. As the patients were mostly more than 60 years of age, use of a conversion factor of 5 between MAE and EF [22] translates the standard deviation of the error to 9.8% for automatic PSU analysis and 11.6% for automatic HCU analysis, in terms of EF. By only using the septal point for MAE calculation, the numbers are 9.5% (PSU) and 8.9% (HCU). The review paper in [23] reported interobserver variabilities of EF using Simpsons rule, corresponding to standard deviations of the difference between the observers, ranging from 4.1% (a study on echogenic patients) to 10.7%. For intraobserver variability, the range was 3.1% to 6.6%. The algorithm does not perform much worse as an EF estimator than these reported numbers, even if these are studies with full-size scanners.

Nevo eta l. [11] presented a semi-automatic method for MAE measurement

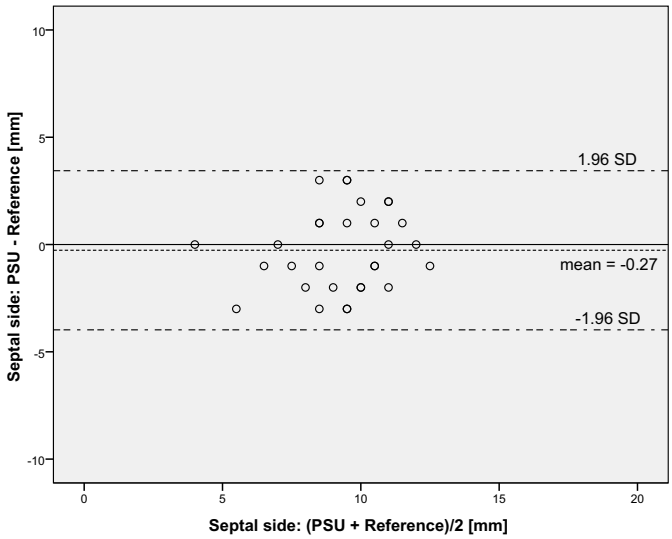

Figure 3.9: Bland-Altman plot of the measurement difference betweeen the automatic algorithm using only the septal point and pocket-sized ultrasound (PSU) and manual m-mode measurement on hand-carried ultrasound data (HCU). The dashed line represents the bias in the data, while the dash-dotted lines represent the 95% limits of agreement.

using low frame rate (25Hz) images. The disadvantage of this solution is the reported long computation time of (mean ± SD) 162.1 ±10.3 seconds. A pocket-sized scanner operating at 20 frames per second has a 50ms per frame time limit for real-time algorithm operation. The computation time of our algorithm of 3.7ms per frame suggests that a real-time PSU implementation is feasible, provided that the computational capacity of the PSU systems is approaching that of a regular laptop computer. This will further speed up the exam and completely avoid the need for post-processing.

3.4.1 Limitations and Future work

The goal of this work was to assess left ventricular systolic function by measurement of MAE using a pocket-sized device. It was chosen to use manual anatomic m-mode based MAE measurements as the reference. An alternative would be to use EF. For instance did DeCara et al. [7] present a study based on Philips QLab where they achieved a close correlation ($r^2 = 0.72$) between semi-automatic MAE and biplane EF, using multiple regression. A similar study, using Philips Qlab, was presented in

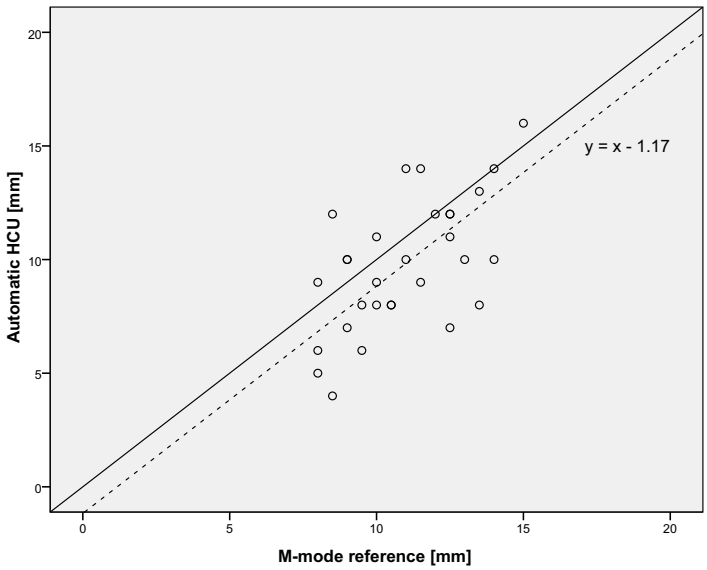

Figure 3.10: Scatter plot with the hand-carried ultrasound (HCU) results along the vertical axis and the m-mode reference values along the horizontal axis. The solid line is the reference unity line (y = x). The dashed line represents the unity line corrected for the negative bias of 1.17mm (y = x - 1.17).

[8]. Different regression formulas have also been presented in several other publications [9, 12]. Unfortunately, it does not seem to be a general agreement on which regression formula to use. In this work, it was thus chosen to use manual MAE directly as the reference. This can be seen as a limitation, as many still consider EF to be the gold standard when measuring cardiac systolic function.

MAE is often measured in several projections, and the MAE value is reported as the average excursion. In this work, only the apical four-chamber view has been used. Also, the best automatic results were achieved using the septal point only. This solution is sensitive to local variability in the excursion of the mitral annlus, for instance due to an infarction.

The tested HCU recordings suffered from gain and saturation issues. This may have influenced the HCU results. For the PSU device, the spatial resolution may have been limited by its output format, which was cartesian image of 240x320 pixels.

Our algorithm is intended to be operated also by less experienced users. In this work, the recordings were made by a cardiologist. This is a limitation, as the image quality is likely to be worse when the operator is a non-expert. The number of subjects in the feasability study is also limited. A larger clinical validation study should be conducted with data from a broader population and, preferably, include users with

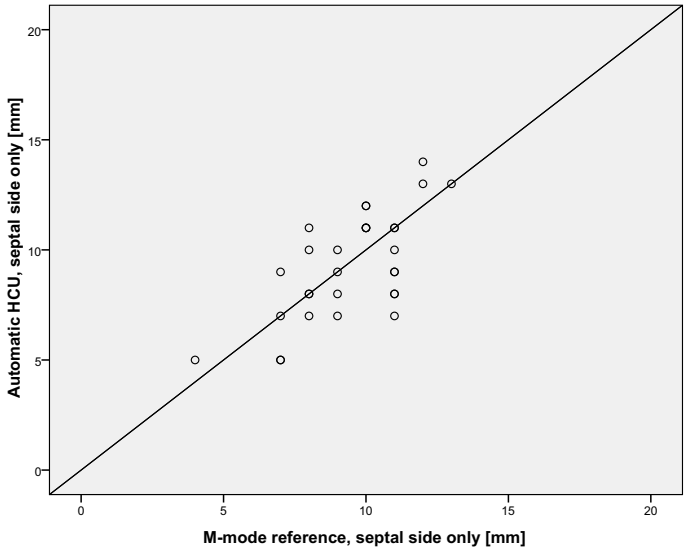

Figure 3.11: Scatter plot with the hand-carried ultrasound (HCU) results, using only the septal value, along the vertical axis and the septal m-mode reference values along the horizontal axis. The solid line is the reference unity line (y = x).

limited training.

Although our computation times suggest that a real-time implementation of the method on a pocket-sized device is feasible, we have not been able to physically verify this. A real-time implementation on a PSU device should be pursued.

In order to make the method more accurate, especially the lateral tracking scheme should be refined. One way of doing this could be to improve the accuracy of the model fit, for instance by developing new edge detectors and refining the parametric left ventricle model. By putting more weight on the model motion than the block matching, the lateral mitral annulus tracking could possibly be made more accurate.

3.5 Conclusions

We have presented a fully automatic algorithm for MAE measurement using low frame rate apical four-chamber images from a pocket-sized ultrasound device. The algorithm is highly efficient, and the measured computation times strongly suggest that real-time operation is feasible. The accuracy of the algorithm should be suitable for successfully separating poor ventricles from normal ones and is comparable to previously reported numbers comparing anatomic m-mode and semi-automatic regular frame rate speckle tracking. The MAE values are on average underestimated. This effect is reduced

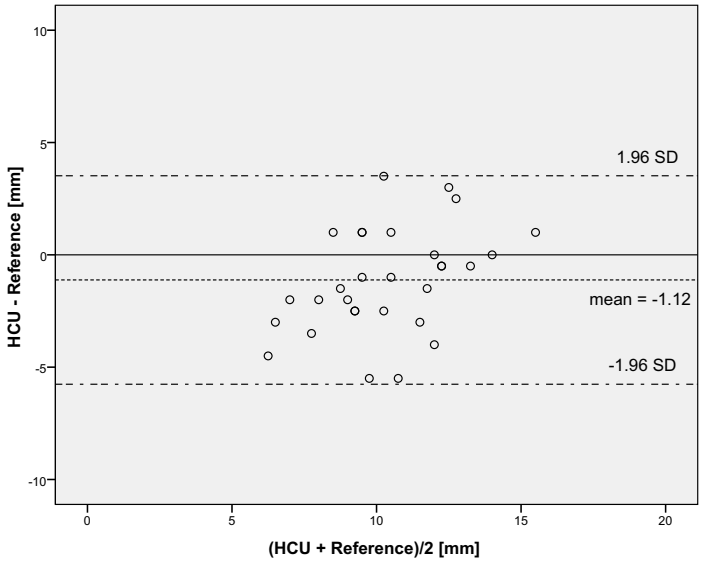

Figure 3.12: Bland-Altman plot of the measurement difference betweeen the automatic algorithm and manual m-mode measurement. Both the automatic results and reference measurements were made using hand-carried ultrasound data (HCU). The dashed line represents the bias in the data, while the dash-dotted lines represent the 95% limits of agreement.

by only using the septal point for MAE calculation. We believe that the presented algorithm is a promising method for rapid assessment of systolic function using PSU systems.

Acknowledgment

The authors would like to thank MD Håvard Dalen for providing training data and Program Manager Sigmund Frigstad (GE Vingmed Ultrasound) for providing access to the Vscan. We would also like to thank the Norwegian Research Council for funding the project.

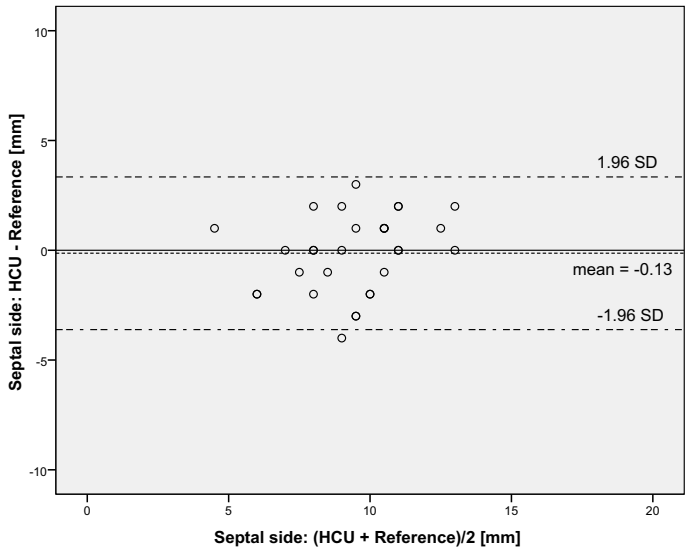

Figure 3.13: Bland-Altman plot of the measurement difference betweeen the automatic algorithm using only the septal point and manual m-mode measurement. Both the automatic results and reference measurements were made using hand-carried ultrasound data (HCU). The dashed line represents the bias in the data, while the dash-dotted lines represent the 95% limits of agreement.

Appendix: Technical notes - Model-based segmentation

This appendix covers the detailled description of the model-based segmentation algorithm, using a Kalman filter.

Calculating model points. The parametric model used in this work is based on Non Uniform Rational B-Splines (NURBS). This is a generalization of the commonly used nonrational B-splines. A k'th degree NURBS curve is defined by:

$$\mathbf{p}_l(u) = \frac{\sum_{i=0}^{n} N_{i,k}(u) w_i \mathbf{q_i}}{\sum_{i=0}^{n} N_{i,k}(u) w_i}, a \leq u \leq b \tag{3.6}$$

$N_{i,k}(u)$ are the k'th-degree B-spline basis functions. $\mathbf{q_i}$ are the control points for the spline. Lastly, w_i are the weights of the NURBS curve. The constants a and b are upper and lower bounds for the parametric coordinate, u. We denote points on the NURBS curve as $\mathbf{p}_l(u)$ for reasons which will become clear later. We define the rational basis functions as:

$$b_{i,k}(u) = \frac{N_{i,k}(u) w_i}{\sum_{j=0}^{n} N_{j,k}(u) w_j}, a \leq u \leq b \tag{3.7}$$

which allows us to write:

$$\mathbf{p}_l(u) = \sum_{i=0}^{n} b_{i,k}(u) \mathbf{q_i}, a \leq u \leq b \tag{3.8}$$

The basis functions are defined on the knot vector:

$$U = a, \ldots, a, u_{k+1}, \ldots, u_{m-k-1}, b, \ldots, b \tag{3.9}$$

We note that the NURBS curves are linear in their control points, which make them well suited for parameter estimation. In this work, the knot vector has been chosen such that $a = 0$, $b = 1$ and $u_{k+1}, \ldots, u_{m-k-1}$ are uniformly distributed. The left ventricle model is designed in a custom made Matlab (v2008a, The MathWorks, Inc.) environment, where it is possible to freely select control points, knots, weights and parametric coordinates for edge and speckle tracking measurements. The weights have been adjusted to preserve the corner between the AV plane and the LV walls.

System states. A Kalman filter requires the model or system to be described by states. We choose to denote the normal displacement of the control vertices as the local states, $\mathbf{x}_l$. The control point is written as:

$$\mathbf{q}_i = \bar{\mathbf{q}}_i + x_{l,i} \mathbf{n}_i \tag{3.10}$$

where $\mathbf{n}_i$ is the normal displacement vector for the control vertex and $\bar{\mathbf{q}}_i$ is the mean position of the control vertex. The pose parameters (translation, rotation and scale) are used as global states, $\bar{\mathbf{x}}_\mathbf{g}$. Combining the local and global states results in one state vector suitable for the Kalman filter framework, $\mathbf{x} = \mathbf{x}_l + \mathbf{x}_g$. Control points in

the base center should not be moved, as no significant shape alternations are expected in this region. These points are thus not included in the state vector.

The relation between the system states and the points on the deformable model is described by a local (T_l) and global transform (T_g). We denote the points on the final contour as $\mathbf{p}$. For simplicity, we write the points on the contour prior to application of the global pose as $\mathbf{p}_l$. We define a vector $\mathbf{u}$ with length N_c where $0 \leq u_i \leq 1$. This yields:

$$\mathbf{p}_l = [p_l(u_0), p_l(u_1), \ldots, p_l(u_{N_c-1})] \tag{3.11}$$

where $p_l(u_i)$ is evaluated using equation 3.8 for each element in $\mathbf{u}$. Equation 3.8 thus defines the local transformation T_l. $\mathbf{p}_l$ is then transformed by the global pose transform, T_g to get the correct position of the model.

$$\mathbf{p} = T_g(\mathbf{p}_l, \mathbf{x_g}) \tag{3.12}$$

The composite deformation model, T includes both the local and global transforms. It is necessary to calculate the Jacobian of T. The local Jacobian matrix is found by multiplying the displacement vectors with their respecitve basis functions:

$$\mathbf{J}_l = [b_{i_0}\mathbf{n}_{i_0}, b_{i_1}\mathbf{n}_{i_1}, \ldots] \tag{3.13}$$

This can be precomputed, and thus eases the real-time operation.

The global T_g transform is directly applied to curve points, as in equation 3.12. This is not the case with the curve normals, where the curve normal transformation rule must be applied [13, 24]:

$$\mathbf{n}_g = \left|\frac{\partial T_g(\mathbf{p}_l, \mathbf{x}_g)}{\partial \mathbf{p}_l}\right| \left(\frac{\partial T_g(\mathbf{p}_l, \mathbf{x}_g)}{\partial \mathbf{p}_l}\right)^{-T} \mathbf{n}_l \tag{3.14}$$

The overall Jacobian matrix is derived applying the chain-rule of multivariate calculus:

$$\mathbf{J}_g = \left[\frac{\partial T_g(\mathbf{p}_l, \mathbf{x}_g)}{\partial \mathbf{x}_g}, \frac{\partial T_g(\mathbf{p}_l, \mathbf{x}_g)}{\partial \mathbf{p}_l} J_l\right] \tag{3.15}$$

Prediction step. During the prediction step, the state estimates are predicted based on the posterior estimates from last iteration. It is also possible to expand this model to model motion. We use a bar above the variable to indicate the a priori value and a hat for the posterior value.

$$\bar{\mathbf{x}}_{\mathbf{k+1}} - \mathbf{x_0} = \mathbf{A}(\hat{\mathbf{x}}_{\mathbf{k}} - \mathbf{x_0}) \tag{3.16}$$

Measurements. As measurement input to the Kalman filter, we have used simple edge measurements and block matching. The edge measurements are made using *normal displacements*. N_p edge points are distributed around the NURBS model. For each edge point, it is searched for an intensity transition along a normal, $\mathbf{n}$, to the NURBS curve in this point. We use a *step* detector based on minimization of the sum of square errors (SSE) between a perfect step function and the sample vector taken normal to the model. Weak edges are discarded using a thresholding of the intensity

difference across the detected edge or the distance from the neigboring edge detector results. The distance from the edge point to the measured measured edge point is called a *normal displacement* measurement v. The inverse of the mean intensity difference across the detected edge point, is used as a measure of edge confidence, r.

$$v = \mathbf{n^T}(\mathbf{p_{obs}} - \mathbf{p}) \tag{3.17}$$

This measurement must be projected to state space, in order to be useful for the state update. The measurement model must be linear to fit in the Kalman filter framework. This is done using the normal vector projection of the Jacobian.

$$\mathbf{h^T} = \mathbf{n^T J} \tag{3.18}$$

The normal displacement measurements are thus now related to the state vector through $\mathbf{h^T}$. This implies a separate measurement vector, h for each normal displacement measurement.

In addition to the edge measurements, block matching has been used as *Kalman filter input*. N_t points on the NURBS model are selected as centres for the block matching blocks. In frame k, a single kernel block is extracted around each center point. In frame *k+1* a kernel block of the same size is moved within a search window centered around the model center point from the previous frame, and a SAD fit to the previous frame is calculated, defining the new kernel center position for frame *k+1*. The normal component of the vector from the kernel position in frame k to frame *k+1* defines a normal displacement vector, and is used as a filter input in the same manner as for edge detection. This use of block matching is not strictly necessary, but adds to the robustness of the method.

Assimilation. Calculating the regular Kalman gain using the standard equations will in this case be computationally intensive because there are many more measurements than there are states. The measurements are thus instead assimilated into *information space*. If the measurements can be considered uncorrelated, this gives a very efficient processing, as the measurement covariance matrix, $\mathbf{R}$ becomes diagonal:

$$\mathbf{H^T R^{-1} v} = \sum_i \mathbf{h_i} r_i^{-1} v_i \tag{3.19}$$

$$\mathbf{H^T R^{-1} H} = \sum_i \mathbf{h_i} r_i^{-1} \mathbf{h_i^T} \tag{3.20}$$

This avoids inversion of matrices with dimension larger than the dimension of the state vector.

Update. The Kalman gain, $\mathbf{K_k}$, is given by

$$\mathbf{K_k} = \hat{\mathbf{P}}_\mathbf{k} \mathbf{H^T R^{-1}} \tag{3.21}$$

where $\mathbf{P}$ means the error covariance matrix. The update step becomes:

$$\hat{\mathbf{x}}_\mathbf{k} = \bar{\mathbf{x}}_\mathbf{k} + \hat{\mathbf{P}}_\mathbf{k} \mathbf{H^T R^{-1} v_k} \tag{3.22}$$

The updated error covariance matrix using information space becomes:

$$\hat{\mathbf{P}}_{\mathbf{k}}^{-\mathbf{1}} = \bar{\mathbf{P}}_{\mathbf{k}}^{-\mathbf{1}} + \mathbf{H}^{\mathbf{T}}\mathbf{R}^{-\mathbf{1}}\mathbf{H} \tag{3.23}$$

By applying equations 3.8, 3.12 and 3.10, it is now possible to calculate the model points.

References

[1] K. Spencer, "Hand-carried cardiac ultrasound," *Current Cardiovascular Imaging Reports*, vol. 1, no. 1, pp. 66–71, 2008.

[2] J. J. Atherton, "Screening for left ventricular systolic dysfunction: Is imaging a solution," *J. Am. Coll. Cardiol. Img.*, vol. 3, no. 4, pp. 421 – 428, 2010.

[3] B. C. Culp, J. D. Mock, C. D. Chiles, and W. C. Culp, "The pocket echocardiograph: Validation and feasibility," *Echocardiography*, pp. 1–6, 2010. doi:10.1111/j.1540-8175.2009.01125.x, E-publication ahead of print.

[4] E. C. Vourvouri, A. F. Schinkel, J. R. Roelandt, F. Boomsma, G. Sianos, M. Bountioukos, F. B. Sozzi, V. Rizzello, J. J. Bax, H. I. Karvounis, and D. Poldermans, "Screening for left ventricular dysfunction using a hand-carried cardiac ultrasound device," *Eur J Heart Fail*, vol. 5, no. 6, pp. 767–74, 2003.

[5] M. Egan and A. Ionescu, "The pocket echocardiograph: a useful new tool?," *Eur J Echocardiogr*, vol. 9, no. 6, pp. 721–5, 2008.

[6] D. M. Spevack, D. M. Spevack, P. A. Tunick, and I. Kronzon, "Hand carried echocardiography in the critical care setting," *Echocardiography*, vol. 20, no. 5, pp. 455–61, 2003.

[7] J. M. DeCara, E. Toledo, O. S. Salgo, G. Lammertin, L. Weinert, and R. M. Lang, "Evaluation of left ventricular systolic function using angle-independent motion tracking of mitral annular displacement," *J AM Soc Echocardiogr*, vol. 18, no. 12, pp. 1266–1269, 2005.

[8] W. Tsang, H. Ahmad, A. R. Patel, L. Sugeng, I. S. Salgo, L. Weinert, V. Mor-Avi, and R. M. Lang, "Rapid estimation of left ventricular function using echocardiographic speckle-tracking of mitral annular displacement," *J Am Soc Echocardiogr*, vol. 23, no. 5, pp. 511–515, 2010.

[9] K. Emilsson, M. Alam, and B. Wandt, "The relation between mitral annulus motion and ejection fraction: A nonlinear function," *J AM Soc Echocardiogr.*, vol. 13, no. 10, pp. 896 – 901, 2000.

[10] M. F. Elnoamany and A. K. Abdelhameed, "Mitral annular motion as a surrogate for left ventricular function: Correlation with brain natriuretic peptide levels," *Eur J Echocardiogr*, vol. 7, no. 3, pp. 187–198, 2006.

[11] S. T. Nevo, M. van Stralen, A. M. Vossepoel, J. H. Reiber, N. de Jong, A. F. van der Steen, and J. G. Bosch, "Automated tracking of the mitral valve annulus motion in apical echocardiographic images using multidimensional dynamic programming," *Ultrasound in Medicine & Biology*, vol. 33, no. 9, pp. 1389 – 1399, 2007.

[12] Y. Eto, H. Yamada, J.-H. Shin, D. A. Agler, H. Tsujino, J.-X. Quin, G. Saracino, N. L. Greenberg, J. D. Thomas, and T. Shiota, "Automated mitral annular tracking: A novel method for evaluating mitral annular motion using two-dimensional echocardiography," *J AM Soc Echocardiogr*, vol. 18, no. 4, pp. 306–312, 2005.

[13] F. Orderud and S. I. Rabben, "Real-time 3d segmentation of the left ventricle using deformable subdivision surfaces," in *Computer Vision and Pattern Recognition, IEEE Computer Society Conference on*, (Los Alamitos, CA, USA), pp. 1–8, IEEE Computer Society, June 24-26 2008.

[14] F. Orderud, G. Kiss, S. Langeland, E. Remme, H. Torp, and S. Rabben, "Real-time left ventricular speckle-tracking in 3d echocardiography with deformable subdivision surfaces," in *MICCAI workshop on Analysis of Medical Images*, pp. 41–48, 2008.

[15] A. Blake, R. Curwen, and A. Zisserman, "A framework for spatio-temporal control in the tracking of visual contours," *Int. J. Comput. Vis.*, vol. 11, no. 2, pp. 127–145, 1993.

[16] A. Blake, M. Isard, and D. Reynard, "Learning to track the visual motion of contours," *Artificial Intelligence*, vol. 78, pp. 179–212, Oct 1995.

[17] G. Jacob, J. A. Noble, M. Mulet-Parada, and B. A., "Evaluating a robust contour tracker on echocardiographic sequences," *Med. Image Anal.*, vol. 3, pp. 63–75, 1999.

[18] G. Jacob, J. A. Noble, A. D. Kelion, and A. P. Banning, "Quantitative regional analysis of myocardial wall motion," *Ultrasound in medicine & biology*, vol. 27, no. 6, pp. 773–84, 2001. 0301-5629.

[19] G. Jacob, J. Noble, C. Behrenbruch, A. Kelion, and A. Banning, "A shape-space-based approach to tracking mycordial borders and quantifying regional left-ventricular function applied in echocardiography," *IEEE Trans. Med. Imag.*, vol. 21, pp. 226–238, Mar 2002.

[20] J. B. Seward, P. S. Douglas, R. Erbel, R. E. Kerber, I. Kronzon, H. Rakowski, L. D. Sahn, E. J. Sisk, A. J. Tajik, and S. Wann, "Hand-carried cardiac ultrasound

(hcu) device: recommendations regarding new technology. a report from the echocardiography task force on new technology of the nomenclature and standards committee of the american society of echocardiography," *J Am Soc Echocardiogr*, vol. 15, no. 4, pp. 369–73, 2002.

[21] S. Y. Hayashi, B. I. Lind, A. Seeberger, M. M. do Nascimento, B. J. Lindholm, and L. A. Brodin, "Analysis of mitral annulus motion measurements derived from m-mode, anatomic m-mode, tissue doppler displacement, and 2-dimensional strain imaging," *J Am Soc Echocardiogr*, vol. 19, no. 9, pp. 1092–101, 2006.

[22] K. Emilsson and B. Wandt, "The relation between mitral annulus motion and ejection fraction changes with age and heart size," *Clinical Physiology*, vol. 20, no. 1, pp. 38–43, 2000. 10.1046/j.1365-2281.2000.00221.x.

[23] J. H. McGowan and J. G. Cleland, "Reliability of reporting left ventricular systolic function by echocardiography: a systematic review of 3 methods," *Am Heart J*, vol. 146, no. 3, pp. 388–97, 2003. Journal Article Review United States.

[24] A. H. Barr, "Global and local deformations of solid primitives," *ACM SIGGRAPH Computer Graphics*, vol. 18, pp. 21–30, Jul 1984.

Chapter 4

Automated Septum Thickness Measurement - A Kalman Filter Approach

Sten Roar Snare[1], Ole Christian Mjølstad[1,2], Fredrik Orderud[3], Håvard Dalen[4] and Hans Torp[1]
[1] Dept. Circulation and Medical Imaging, NTNU
[2] Dept. Cardiology, St. Olav Hospital, Trondheim, Norway
[3] GE Vingmed Ultrasound, Horten, Norway
[4] Levanger Hospital, Nord-Trøndelag Health Trust, Levanger, Norway

Interventricular septum thickness in end-diastole (IVSd) is one of the key parameters in cardiology. This paper presents a fast algorithm, suitable for pocket-sized ultrasound devices, for measurement of IVSd using 2D B-mode parasternal long axis images.
The algorithm is based on a deformable model of the septum and the mitral valve. The model shape is estimated using an extended Kalman filter.
A feasibility study using 32 unselected recordings is presented. The recordings originate from a database consisting of subjects from a normal healthy population. Five patients with suspected hypertrophy were included in the study. Reference B-mode measurements were made by two cardiologists.
A paired t-test revealed a non-significant mean difference, compared to the B-mode reference, of (mean ± SD) $0.14mm \pm 1.36mm$ (p=0.532). Pearson's correlation coefficient was 0.79 ($p < 0.001$). The results are comparable to the variability between the two cardiologists, which was found to be $1.29mm \pm 1.23mm$ ($p < 0.001$). The results indicate that the method has potential as a tool for rapid assessment of IVSd.

4.1 Introduction and Literature

With the advent of pocket-sized and low cost ultrasound devices, new and less experienced user groups are expected. For the less experienced ultrasound user,

automation is likely to improve the robustness and repeatability of the clinical measurements.

The interventricular septum wall thickness in end-diastole (IVSd) is a frequently used measurement in echocardiography. In arterial hypertension, left ventricular hypertrophy (LVH) is associated with increased risk of both cardiovascular morbidity and mortality [1]. The American Society of Echocardiography [2] mentions the septal and posterior wall thickness alone as a an easy way to detect LVH. The guidelines [2] suggest a normal range for IVSd of 0.6-0.9cm for women and 0.6-1.0cm for men. A septum is considered moderately abnormal when IVSd is measured between 1.3-1.5cm for women and 1.4-1.6cm for men. Measurements above these values are considered severely abnormal.

Current guidelines [2], recommend a parasternal long axis view in combination with 2D B-mode or 2D targeted M-mode when measuring IVSd. The measurement should be made at the level of the mitral valve leaflet tips. Targeted M-mode has the advantage that it is easier to separate the septum from other structures such as the moderator band, tricuspid apparatus or false tendons. On the other hand, it can sometimes be difficult to place the M-mode cursor exactly perpendicular to the septum, especially for untrained users. The image in 2D B-mode is visually more intuitive than the M-mode, but the septal border can be blurred or completely missing in single frames. On several pocket-sized devices, M-mode is not available, leaving 2D B-mode as the only option.

This work aims to present a fast, automated lightweight system for IVSd measurement, suitable for pocket-sized systems. Among the few publications on this topic is a study by Moladoust et al. [3] that published a semi-automatic approach using an adaptive thresholding algorithm. The motivation for automating the IVSd measurement is to:

- Ease operation of pocket-sized systems, where manual image measurements are unpractical
- Get more consistent results when the system is operated by less experienced personnel

In this paper, the algorithm is first described in detail. Then, the results from a feasibility study are presented and discussed.

4.2 Materials and Method

The proposed algorithm is based on contour tracking in 2D B-mode images using coupled Non-Uniform Rational B-spline (NURBS) models and an extended Kalman filter. The tracking scheme is based on the method proposed in [4]. Deformable model segmentation using a Kalman filter framework has been previously published in [5–8]. We take the approach one step further by combining several parametric NURBS contours in a hierarchy. The algorithm enables the use of information from several frames when doing septum segmentation, thus making the algorithm less sensitive to

the image quality in the end-diastolic (ED) frame. The system is implemented in C++ and uses Matlab (v2008a, The Mathworks Inc.) for model design. The system loads raw ultrasound beam data from dicom files and uses an in-house scan converter to create cartesian images.

4.2.1 Deformable model

The algorithm utilizes a deformable model of the interventricular septum and the mitral valve. The recording is assumed to be a standard parasternal long-axis view. The deformable model is constructed using four NURBS curves which are *coupled* using geometric transforms. A NURBS curve is a generalization of the commonly used non-rational B-spline. It has the advantage of being linear in its parameters and is thus suitable for parameter estimation. In addition, using NURBS instead of regular B-splines offers more flexibility for shape preservation in the model. A thorough description of NURBS is found in [9]. A point on a k'th degree NURBS curve is denoted as $\mathbf{p}_l(u)$ and found by:

$$\mathbf{p}_l(u) = \frac{\sum_{i=0}^{n} N_{i,k}(u) w_i \mathbf{q_i}}{\sum_{i=0}^{n} N_{i,k}(u) w_i}, u_{low} \leq u \leq u_{high} \tag{4.1}$$

$N_{i,k}(u)$ are the k'th-degree B-spline basis functions, $\mathbf{q_i}$ are the spline control points and w_i are the weights assigned to each control point. u_{high} and u_{low} are upper and lower bounds for the parametric coordinate, u. The rational basis functions are defined as:

$$b_{i,k}(u) = \frac{N_{i,k}(u) w_i}{\sum_{j=0}^{n} N_{j,k}(u) w_j}, u_{low} \leq u \leq u_{high} \tag{4.2}$$

which allow us to write:

$$\mathbf{p}_l(u) = \sum_{i=0}^{n} b_{i,k}(u) \mathbf{q_i}, u_{low} \leq u \leq u_{high} \tag{4.3}$$

The basis functions are defined on the knot vector:

$$U = u_{low}, \ldots, u_{low}, u_{k+1}, \ldots, u_{m-k-1}, u_{high}, \ldots, u_{high} \tag{4.4}$$

The knot vector has been chosen such that $u_{low} = 0$, $u_{high} = 1$ and $u_{k+1}, \ldots, u_{m-k-1}$ are uniformly distributed.

The complete model consists of four submodels. There is one submodel for the left ventricle (LV) side of the septum, one for the right ventricle (RV) side, one for the aortic outlet (AO) tract and one for the mitral valve (MV) leaflet. The submodels are designed using Matlab (v2008a, The MathWorks, Inc.), and they are updated by adjusting a subset of the control points.

The complete model is found by rotating (Rz), scaling (S) and translating (Tx, Ty) the submodels relative to each other using basic two-dimensional geometric transforms [10]. We denote the similarity transforms, allowing both rotation, scale and translation, by $\mathcal{T}$. Four similarity transforms are used. These are the LV side

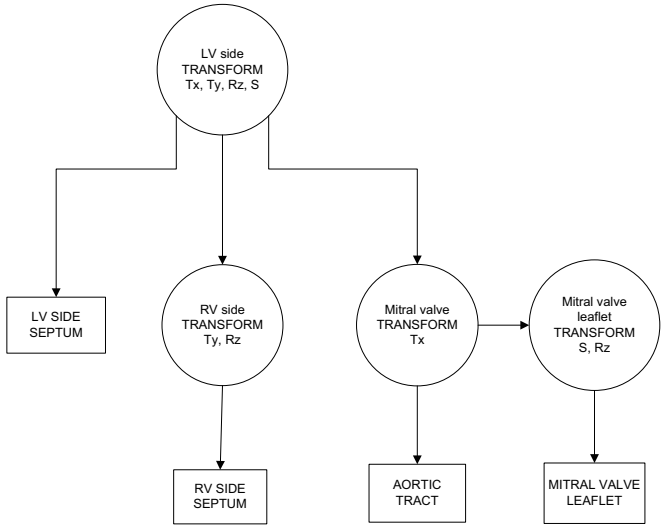

Figure 4.1: The transform hierarchy for the automated septum thickness measurement system. RV = right ventricle. LV = left ventricle. The dynamic transformation parameters for each similarity transform (circles) are indicated. (Tx = horizontal translation, Ty = vertical translation , S = scale, Rz = rotation). The NURBS submodels are represented by the squares.

transform ($\mathcal{T}_{LV}$), RV side transform ($\mathcal{T}_{RV}$), MV transform ($\mathcal{T}_{MV}$) and mitral valve leaflet (MVL) transform ($\mathcal{T}_{MVL}$). These transforms are arranged in a hierarchy, see Fig.4.1. The combined geometric transformations can be written as:

$$\begin{aligned} \mathbf{p}_{LV}(u) &= \mathcal{T}_{LV}(\mathbf{p}_{l,LV}(u)) \\ \mathbf{p}_{RV}(u) &= \mathcal{T}_{LV}(\mathcal{T}_{RV}(\mathbf{p}_{l,RV}(u))) \\ \mathbf{p}_{AO}(u) &= \mathcal{T}_{LV}(\mathcal{T}_{MV}(\mathbf{p}_{l,AO}(u))) \\ \mathbf{p}_{MV}(u) &= \mathcal{T}_{LV}(\mathcal{T}_{MV}(\mathcal{T}_{MVL}(\mathbf{p}_{l,MV}(u)))) \end{aligned} \tag{4.5}$$

where $\mathbf{p}(u)$ represents a point on the final contour and $\mathbf{p}_l(u)$ a point on the contour, prior to the transformations.

The initial points on the submodel contours, prior to application of transforms, are found using the initial control points, $\mathbf{q}_{0,i}$, and (4.3). The complete initial model is configured by manually tuning the transforms in (4.5). The left screenshot in Fig.4.2 shows how the four models are connected, and how the transforms have been used to orient the models to an initial shape.

Some of the transform parameters are also used as variables in the segmentation

scheme, as indicated in Fig. 4.1. This ensures that the different models are allowed to move and scale relative to each other during tracking. As an example, the RV side septum model can rotate and translate along the y-axis, relative to the LV side septum model. Note that there is no relationship between the parameters in the different similarity transforms, $\mathcal{T}$. By defining a vector $\mathbf{x}_g$ containing the nine dynamic transformation parameters as:

$$\mathbf{x}_g = [Tx_{LV}, Ty_{LV}, S_{LV}, Rz_{LV}, Ty_{RV}, Rz_{RV}, Tx_{MV}, S_{MVL}, Rz_{MVL}] \tag{4.6}$$

the transforms in (4.5) can be used to introduce the term *global transform*, T_g:

$$\begin{aligned} T_{g,LV}(\mathbf{p}_{l,LV}(u), \mathbf{x}_g) &= \mathcal{T}_{LV}(\mathbf{p}_{l,LV}(u), \mathbf{x}_g) \\ T_{g,RV}(\mathbf{p}_{l,RV}(u), \mathbf{x}_g) &= \mathcal{T}_{LV}(\mathcal{T}_{RV}(\mathbf{p}_{l,RV}(u), \mathbf{x}_g), \mathbf{x}_g) \\ T_{g,AO}(\mathbf{p}_{l,AO}(u), \mathbf{x}_g) &= \mathcal{T}_{LV}(\mathcal{T}_{MV}(\mathbf{p}_{l,AO}(u), \mathbf{x}_g), \mathbf{x}_g) \\ T_{g,MV}(\mathbf{p}_{l,MV}(u), \mathbf{x}_g) &= \mathcal{T}_{LV}(\mathcal{T}_{MV}(\mathcal{T}_{MVL}(\mathbf{p}_{l,MV}(u), \mathbf{x}_g), \mathbf{x}_g), \mathbf{x}_g) \end{aligned} \tag{4.7}$$

Based on the initial transform parameters and the continuously updated transform parameters in $\mathbf{x}_g$, the global transforms convert points on each contour, prior to geometric transformations, to the final model contour points.

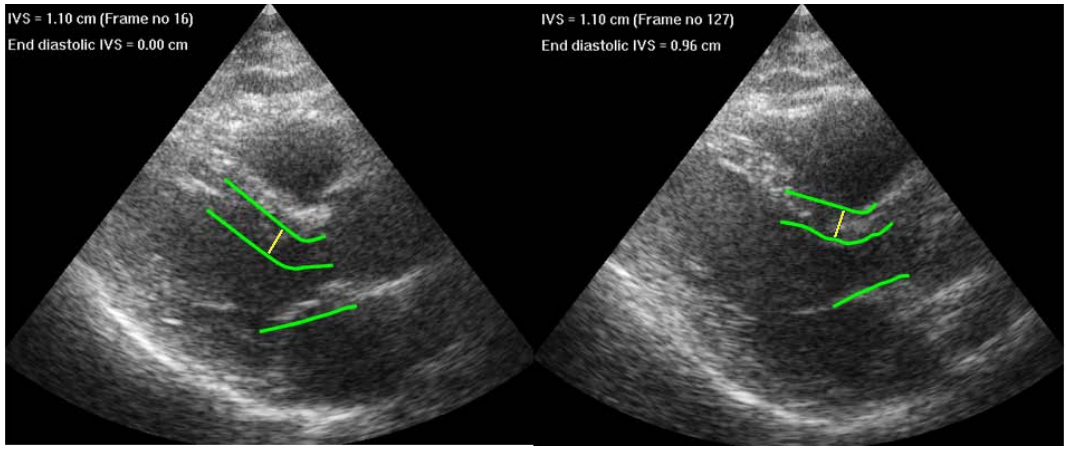

Figure 4.2: The image to the left shows a screenshot of the initial model defined by the four NURBS submodels and the transform hierarchy. To the right is the same model after convergence

Each NURBS submodel is equipped with a predetermined number of parametric edge detector and block-matching points. In this work, the N edge or block-matching points for each model are uniformly distributed in the parametric space:

$$\mathbf{u}_{edge/block} = \frac{1}{N-1}[0, 1, \ldots, N-1] \tag{4.8}$$

The edge detection and block matching are used as input to the Kalman filter.

The septum models are designed as lines with a small bend in the basal region. The purpose of these bends is to aid the model in correctly locating in the apex-base direction. On the left side, the bend hooks onto the aortic outlet tract. The transition from the septum to the aortic tract functions as a landmark for the model.

The LV side septum model is designed using 16 control points and a cubic NURBS curve. The first four control points in the apical region are not allowed to change the shape of the model. This is done due to the inferior image quality often seen in the apical region. The septum model will preserve its shape even in poor images. This is done at the cost of not being able to represent local deformations of the septum in this region. As the measurement is to be taken at the mitral valve tip level, this is not considered a problem for the accuracy. The NURBS weights are higher in the basal region, in order to preserve the above mentioned bend. A number of 25 block-matching and 40 edge detector points are distributed along the model. The LV side septum model is shown in Fig.4.3a.

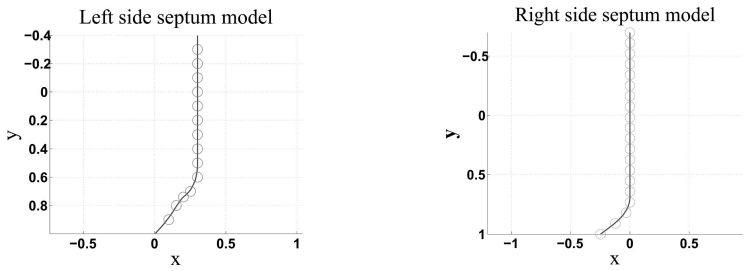

(a) Left Ventricle Side (b) Right Ventricle Side

Figure 4.3: Illustration of the septum models including control points (circles) and the bends used to correctly locating the models in the apex-base direction. Models are shown in model space, prior to transformations

The RV side model is more complex. It has 20 control points, of which 11 are allowed to change the model shape. The first seven and the last two control points are fixed. The seven fixed points are in the apical region, and they are fixed as an aid to get the model to behave correctly in cases with poor image quality and trabeculae/moderator band. Again, this reduces the ability to follow local septal deformations in this region. The last two control points are also fixed to support the NURBS weights in preserving the sharp transition between the septum and the bend. The model is equipped with 40 edge detectors and 20 block matching points. The RV side model is shown in Fig.4.3b.

The septum thickness measurement is done at the level of the MV tip. In order to achieve this, a hinge model of the MV and aortic tract is used. This is created using the $\mathcal{T}_{MVL}$ transform, which allows the mitral valve leaflet model to rotate around one tip of the aortic tract model. The aortic outlet tract model is also cubic and consists of 13 control points of which every second is movable. It uses 20 edge detection points

and 20 block-matching points. The leaflet model consists of 13 control points, of which only the first one is movable.

4.2.2 Kalman tracking

Based on the framework from [4], the Kalman tracking scheme will now be discussed. The IVSd measurement is made at the ED frame. Still, by using the Kalman filter, temporal information is incorporated into the solution. By running the Kalman filter through the heart cycle, it is possible to get a reasonable measurement, even though the image quality in the ED frame is inferior. Edge detection and block matching between successive frames are used to predict septum thickness based on the previous frames. The prediction is then combined with measurements in the ED frame to get the final IVSd value.

A Kalman filter requires the system to be based on a state vector representation. Here, one part of the state vector is defined as the movement of the movable control points along the curve normal. This part of the state vector is denoted local states, $\mathbf{x}_l$.

$$\mathbf{q}_i = \mathbf{q}_{0,i} + x_{l,i}\mathbf{n}_i \tag{4.9}$$

where $\mathbf{q}_{0,i}$ is the mean/initial position of the control point and $\mathbf{n}_i$ is the corresponding normal displacement vector.

The dynamic transform parameters $\mathbf{x_g}$ in (4.6) are used as global states. Combining the local and global states yields a complete state vector, $\mathbf{x} = [\mathbf{x}_l^T, \mathbf{x}_g^T]^T$.

The system states and the points on the deformable model are related by the local (T_l) and global transforms (T_g). The local transformation, T_l, converts the control points to model points prior to application of geometric transforms. It is defined by (4.3) and varies with the local states, $\mathbf{x}_l$. By considering each submodel separately (omitting model subscripts) and splitting the control points into sets of movable ($\mathcal{M}$) and static ($\mathcal{S}$) points, this can be written as:

$$\begin{aligned} \mathbf{p}_l(u) &= \sum_{i=\mathcal{M}} b_{i,k}(u)(\mathbf{q}_{0,i} + x_{l,i}\mathbf{n}_i) + \sum_{i=\mathcal{S}} b_{i,k}(u)\mathbf{q}_{0,i} \\ \mathbf{p}_l(u) &= T_l(\mathbf{x}_l, u) \end{aligned} \tag{4.10}$$

$\mathbf{p}_l(u)$ is then transformed by the global transform to get the final position of the curve point. The global transform is defined by (4.7) for each of the NURBS models. In practice, it is found by multiplying basic geometric transformations on matrix form [10]. For simplicity and readability, the model subscripts from (4.7) and the parametric coordinate u are ommited in the following description.

$$\mathbf{p} = T_g(\mathbf{p}_l, \mathbf{x_g}) \tag{4.11}$$

The complete deformation model, T, contains both the local and global transforms. The extended Kalman filter requires knowledge of the Jacobian of T. The local Jacobian matrix is derived from (4.10) and is found by multiplying the displacement vectors with their respective basis functions:

$$\mathbf{J}_l = [b_{i_0}\mathbf{n}_{i_0}, b_{i_1}\mathbf{n}_{i_1}, \ldots] \tag{4.12}$$

This is a very efficient calculation and adds to the efficiency of the algorithm.

The global T_g transform is applied directly to curve points, as in 4.11. This is not the case with the curve normals, where the curve normal transformation rule must be applied [4, 11]:

$$\mathbf{n}_g = \left| \frac{\partial T_g(\mathbf{p}_l, \mathbf{x}_g)}{\partial \mathbf{p}_l} \right| \left(\frac{\partial T_g(\mathbf{p}_l, \mathbf{x}_g)}{\partial \mathbf{p}_l} \right)^{-T} \mathbf{n}_l \tag{4.13}$$

The overall Jacobian matrix is derived by applying the chain-rule of multivariate calculus:

$$\mathbf{J}_g = \left[\frac{\partial T_g(\mathbf{p}_l, \mathbf{x}_g)}{\partial \mathbf{x}_g}, \frac{\partial T_g(\mathbf{p}_l, \mathbf{x}_g)}{\partial \mathbf{p}_l} J_l \right] \tag{4.14}$$

Note that T_g is only differentiated with respect to the dynamic transformation parameters.

During the prediction step, the state estimates are predicted based on the posterior estimates from the last iteration. In this paper, the nomenclature of using a bar above the variable to indicate the a priori value and a hat for the posterior value is used. A model predicting the state vector for time $k+1$, based on the deviation from the mean state $\mathbf{x_0}$ is given as:

$$\bar{\mathbf{x}}_{\mathbf{k+1}} - \mathbf{x_0} = \mathbf{A}(\hat{\mathbf{x}}_{\mathbf{k}} - \mathbf{x_0}) \tag{4.15}$$

This is just the assumption that the model is unchanged between frames. The regularization of the model is adjusted using the coefficients in the $\mathbf{A}$ matrix.

The NURBS curve points, normals and Jacobian matrix are now calculated based on the prediction $\bar{\mathbf{x}}_{\mathbf{k}}$.

As input to the Kalman filter, edge measurements and block matching have been used. The edge measurements are based on *normal displacements*. N_p edge points are distributed around the NURBS model. For each edge point on the model, an intensity transition is searched for along the contour normal in this point. The distance from the model point, $\mathbf{p}$, to the measured edge point, $\mathbf{p_{obs}}$, is called a normal displacement measurement v:

$$v = \mathbf{n}^{\mathbf{T}}(\mathbf{p_{obs}} - \mathbf{p}) \tag{4.16}$$

In order to make this useful for the Kalman filter, it is necessary to take the normal projection of the normal displacement measurement:

$$\mathbf{h}^{\mathbf{T}} = \mathbf{n}^{\mathbf{T}}\mathbf{J} \tag{4.17}$$

This implies a separate measurement vector, $\mathbf{h}$, for each normal displacement value. Each measurement is also connected to a measurement noise value r_i, which is calculated as the inverse of the mean intensity difference across the detected edge point. This is used to weight the influence of each edge detection measurement.

To correctly handle the regions on the RV side of the septum, different parts on the model use different edge detectors. The normal displacement measurement and the different edge detectors are illustrated in Fig.4.4. The purpose is to automatically separate structures such as moderator band and trabeculae.

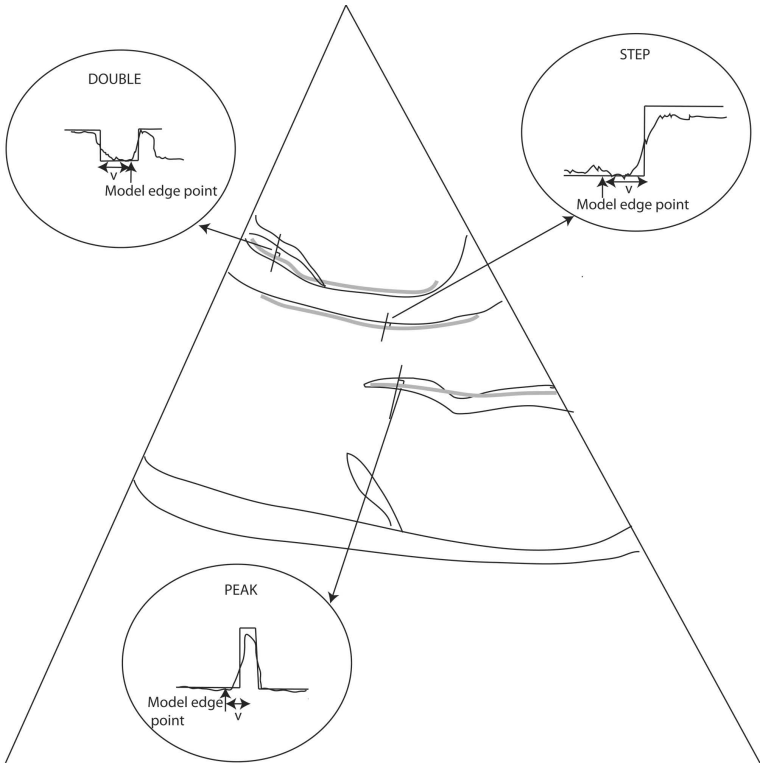

Figure 4.4: Illustration of the normal displacement measurement and the three different types of edge detection criteria.

The LV side model and the basal part of the RV side model use a *step* detector. The detector is based on the minimization of the sum of square errors (SSE) between a perfect step function and the sample vector taken normal to the model. Weak edges are discarded using a thresholding of the intensity difference across the edge transition or the distance from the neighboring edge detector results.

The apical and middle part of the RV side of septum use a *double* edge detector, which searches for the narrow low intensity region between the septum and the moderator band often present in the right ventricle. The edge detector identifies this region and pulls the model towards the septum, avoiding convergence towards the moderator band. The detector uses windowing with overlap. For each windowed segment, the center pixel becomes the candidate location for the low intensity region. Then two linear regression lines are fitted to the data, one to the left of the candidate point and one to the right. The SSE between these regression lines and the sample vector segment is calculated. This is done for all possible windows. The window containing the solution with the highest SSE is most likely the correct segment covering

the low intensity region. The septum itself is now found by thresholding, starting out from the identified point. The method is illustrated in Fig.4.5. Cases where there is no visible moderator band are handled by checking the intensity difference between the identified low intensity region and the the high intensity region. If the difference is small, the edge detection is discarded.

The mitral valve leaflet uses an edge detector tailored to detect peaks in the sample vector. It detects a transition from a low intensity to high intensity and back again, using a threshold. The threshold is set to 25% of the sample length.

In addition to the edge measurements, block matching is applied. A set of N_t points on the NURBS model defines the points that are tracked. The actual points selected for tracking are taken 2mm into the tissue along the curve normal in the N_t model points. The matching is based on the sum of absolute differences (SAD). The normal component of the vector from the position of the matching points in frame k to frame $k+1$ is used as a displacement vector, just as for edge detection.

Using the standard equations to calculate the Kalman gain would be computationally intensive, because there are many more measurements than there are states. Therefore, the measurements are instead assimilated into *information space*. By assuming that the measurements can be considered uncorrelated, the processing is made very efficient, as the measurement covariance matrix, $\mathbf{R}$ becomes diagonal:

$$\mathbf{H^T R^{-1} v} = \sum_i \mathbf{h_i} r_i^{-1} v_i \tag{4.18}$$

$$\mathbf{H^T R^{-1} H} = \sum_i \mathbf{h_i} r_i^{-1} \mathbf{h_i^T} \tag{4.19}$$

The Kalman gain, $\mathbf{K_k}$ used is given by:

$$\mathbf{K_k} = \hat{\mathbf{P}}_\mathbf{k} \mathbf{H^T R^{-1}} \tag{4.20}$$

where $\mathbf{P}$ means the error covariance matrix. The posteriori estimate is found as:

$$\hat{\mathbf{x}}_\mathbf{k} = \bar{\mathbf{x}}_\mathbf{k} + \hat{\mathbf{P}}_\mathbf{k} \mathbf{H^T R^{-1} v_k} \tag{4.21}$$

The updated error covariance matrix using information space becomes:

$$\hat{\mathbf{P}}_\mathbf{k}^{-1} = \bar{\mathbf{P}}_\mathbf{k}^{-1} + \mathbf{H^T R^{-1} H} \tag{4.22}$$

4.2.3 Setting model depth

In order to initialize the model at the correct depth, an algorithm based on a template fit has been used. The algorithm uses a template of a transition from low to high intensity, then, after 1cm, a transition from high to low. This template is then fitted to a vector containing the merged beams from the centermost part of the image sector. The best fitting position is then used as the septum location. The procedure is illustrated in Fig.4.6.

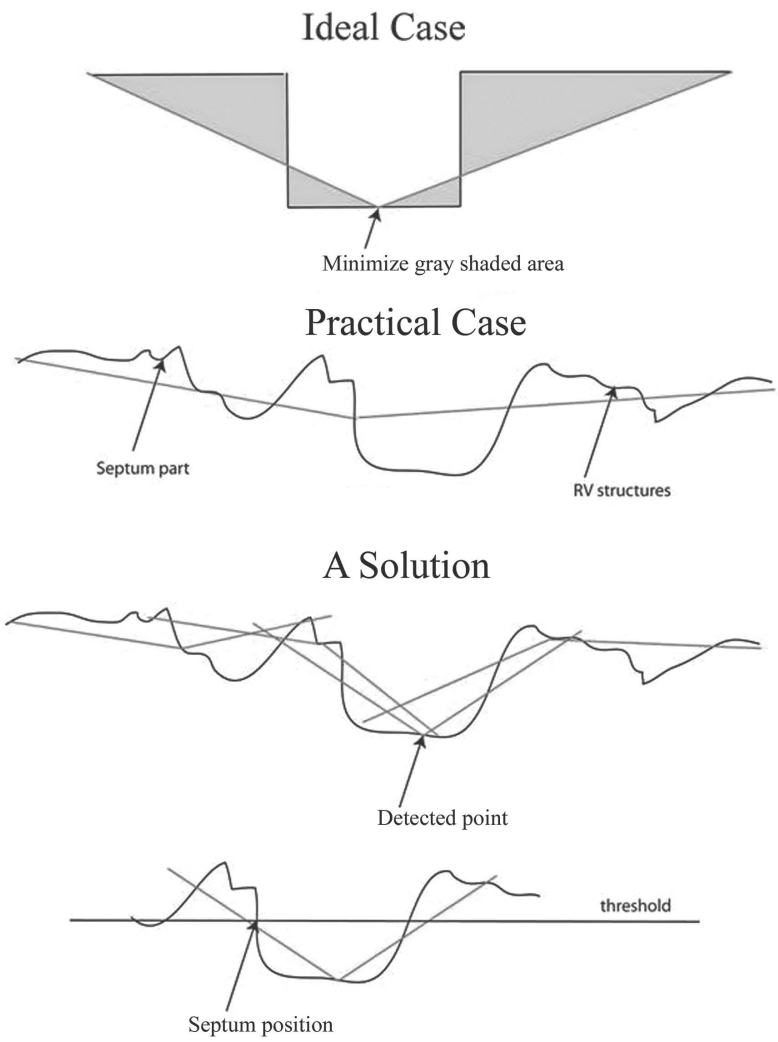

Figure 4.5: Illustration of the double edge criterion. The upper figure shows the overall idea where minimizing the gray shaded area yields the center of the low intensity region. The second figure shows the problem that occurs with noisy images, where minimization of the area can not be used to directly detect the point of interest. The two lower figures shows the practical solution. The line fitting is conducted in a sliding window manner, each line detecting a local intensity drop using minimization of the error, as in the ideal case. Among each local solution, the one with the highest error, is most likely the point to of interest. Detection of septum is then done using thresholding, as in the lower figure.

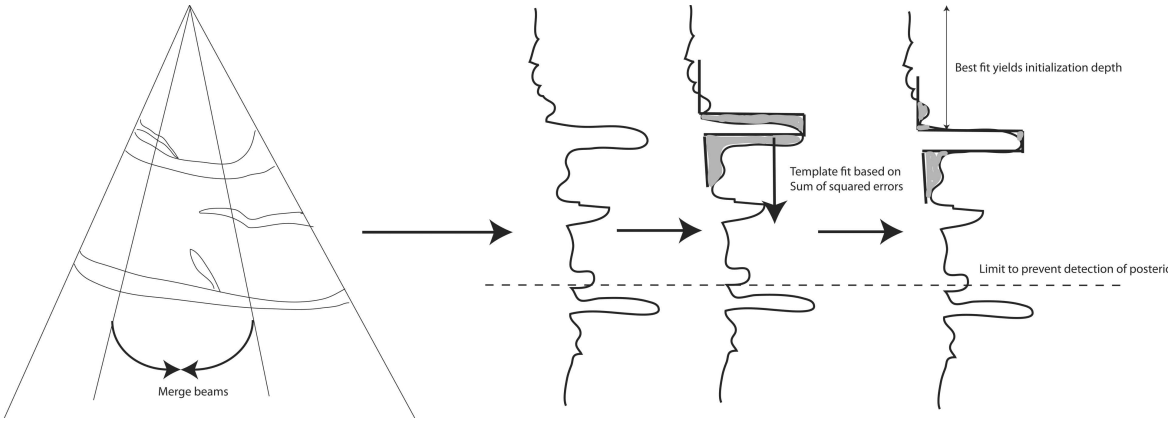

Figure 4.6: Illustration of the depth initialization procedure by template fitting.

4.3 Test material

A dataset of 36 randomly selected recordings and 5 recordings with suspected septal hypertrophy was collected from the Norwegian HUNT database [12]. The HUNT database consists of volunteers from a normal population, without previously diagnosed cardiovascular illnesses, hypertension or diabetes. An ethical committee approval was obtained and informed consent for the study was obtained from all human subjects per the WORLD Medical Association Declaration of Helsinki: Ethical principles for medical research involving human subjects. All recordings were made by a cardiologist using a Vivid 7 (GE Vingmed Ultrasound, Horten, Norway). M-mode septum thickness measurement was a part of the protocol. Reproduceability data for these M-mode measurements was published in [13]. 2D B-mode caliper measurements were chosen as the reference method for the algorithm to enable use of the same image data for reference and algorithm measurements. A brief comparison to the available M-mode measurements was also made, as M-mode is the most frequently used method for measuring IVSd.

Two cardiologists did B-mode reference measurements using the caliper function in the EchoPac software (GE Vingmed Ultrasound, Horten, Norway). The first cardiologist rated the quality of the recordings as "good", "moderate", "poor" or "very poor". In four of the cases, the image quality was so poor that the clinician was unable to measure the septum thickness using B-mode. These four recordings, all from the group of 36 random cases, were discarded. The second cardiologist then did B-mode reference measurements on the remaining 37 recordings. The reference measurements from the two cardiologists were compared using a paired t-test and correlation analysis. The average of the two reference measurements was used as the reference for the IVSd algorithm test.

The algorithm was first run autonomously, analyzing all recordings as a batch. For

each case, an image of the segmentation was stored together with the measurement value for the last ED in the recording. The ECG trace was available, and the onset of the QRS complex was used as a marker for ED. Each recording typically had 3 complete heart cycles. In cases where the images revealed failing depth initialization, the analysis was run again semi-automatically with manual correction of the depth initialization using arrow up and down on the computer keyboard. The automatic analysis was run on all the 37 recordings where reference B-mode measurements were made. The analysis was done using a regular laptop computer (1.17GHz Dual Core, 2GB ram), and a computation time of 7.7ms per frame was achieved.

The reference and algorithm measurements were tested for normality. To compare the values, a paired t-test was applied and the Pearson's correlation coefficient was calculated. The results are presented as mean ± SD. A 5% significance level was used. Bland and Altman plots were generated.

4.4 Results

Examples of IVSd measurements in "poor", "moderate" and "good" image quality recordings are provided in Fig.4.7. The references and automatic measurements both tested successfully for normality. The difference between the two cardiologists' B-mode measurements was found to be $1.29mm \pm 1.23mm$ ($p < 0.001$). The correlation coefficient was 0.84 ($p < 0.001$).

A scatter plot of the automatic analysis versus the reference is found in Fig.4.8. The error between the automatic measurement and the reference was found to be $0.14 \pm 1.36mm$ (p=0.532). Pearson's correlation coefficient was 0.79 ($p < 0.001$). See Fig.4.9 for the Bland and Altman plot. The 95% limits of agreement were -2.53mm to 2.81mm. By excluding the 14 recordings labeled as "poor" or "very poor" image quality, the paired t-test yielded $0.32 \pm 1.27mm$ (p=0.197). The correlation increased to 0.83 ($p < 0.001$). In 8 of 37 (21.6%) cases, the initialization failed and had to be corrected by the user. From the group of 5 hypertrophic patients, 3 recordings needed correction.

Compared to the M-mode references, the automatic IVSd algorithm achieved a mean error of $-0.24 \pm 1.45mm$ (p=0.320). The correlation was 0.74 ($p < 0.001$).

4.5 Discussion

The difference between the automated algorithm and the reference was not found to be statistically significant. A close correlation (r=0.79) between the algorithm result and the reference was found. The correlation improved (r=0.83) when the poor image quality recordings were excluded. The maximum error exceeded the difference between a normal and a mildly hypertrophic septum [2], which is typically 2-3mm. The 95% limits of agreement suggest that the accuracy is suitable for separating betweeen a moderately hypertrophic and normal septum, according to the limits in [2].

The standard deviation of the error (1.36mm) is considerable, but comparable to the standard deviation of the difference between the cardiologists (1.23mm). The

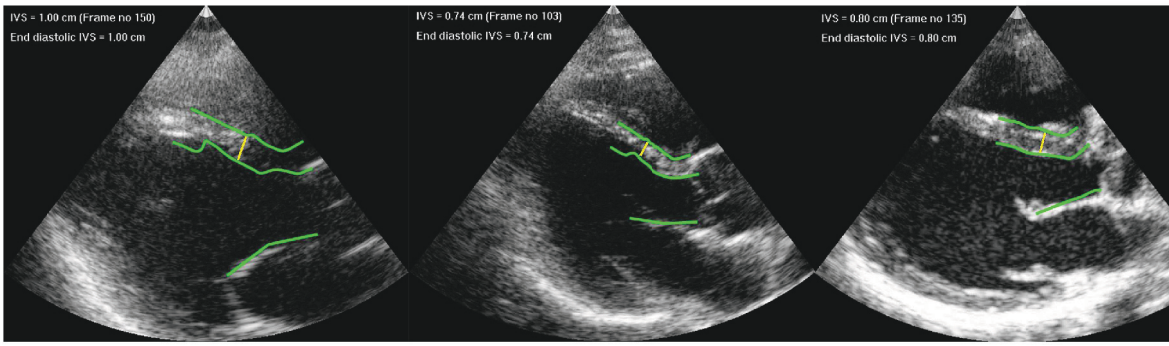

Figure 4.7: From the left to the right are examples of end-diastolic septum thickness measurements in "poor", "moderate" and "good" image quality recordings, yielding errors of -1.90mm, -1.00mm and -0.10mm respectively.

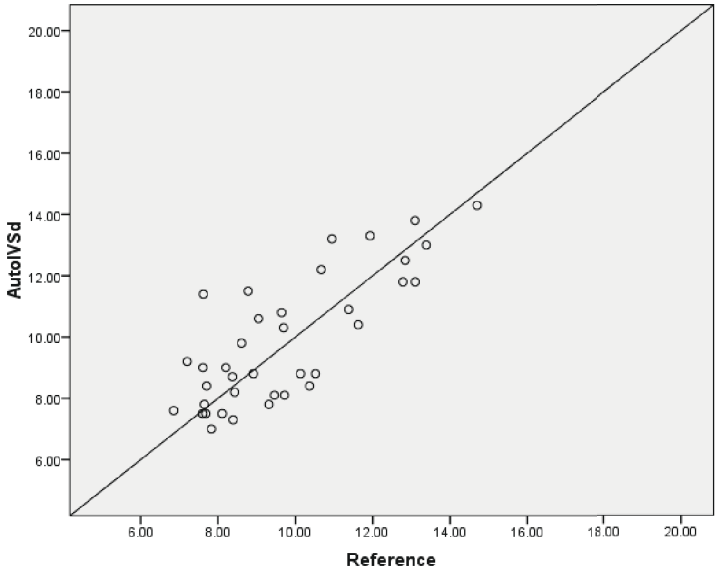

Figure 4.8: Scatter plot of the automatic IVSd algorithm versus the cardiologist B-mode reference

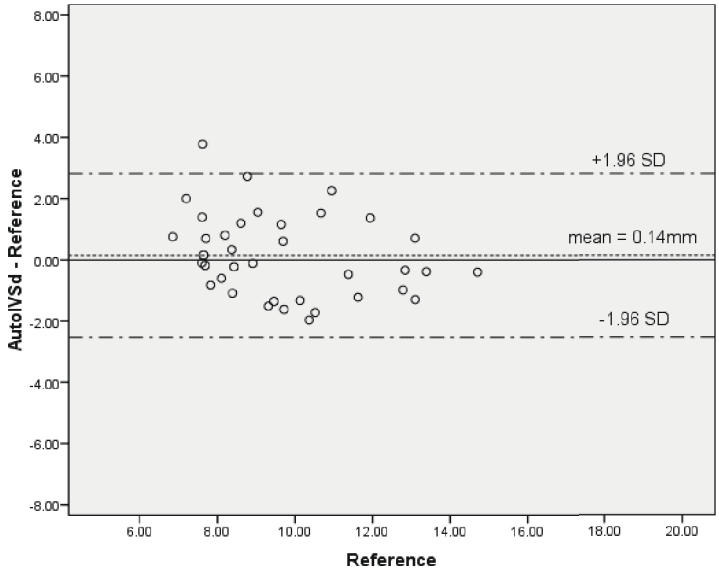

Figure 4.9: Bland and Altman plot illustrating the difference between the automatic IVSd algorithm versus the cardiologist B-mode reference.

large standard deviation can have several explanations. The right ventricle structures are challenging both for the eye and the algorithm. The results indicate that the structures are not always handled correctly by the algorithm. Local changes in septum thickness can also occur, making the thickness sensitive for the measurement level. The measurement level relies on detection of the mitral valve, which is often poorly visible or noisy.

Even when comparing to the M-mode results, it was not possible to identify a statistically significant difference between the algorithm and the manual measurements. A small bias (-0.24mm) was found, and the standard deviation was only slightly higher (1.45mm) than when the B-mode references were used. In the literature, M-mode based septal thickness measurements have been reported to have interobserver errors of 12% [13] and 9.1% [14]. In [15], an even higher interobserver variability of 19.5% was reported, but this study was done with very old equipment and can not be directly compared to more recent results. Converting the mean error between the algorithm and the manual M-mode measurements to percentage yields 11.3%, and is thus in the same range as the numbers found in the literature. The interobserver error for the two cardiologists using B-mode was found to be 15%. This is slightly higher than the M-mode based numbers from the literature. Looking into the data, the variability in the B-mode references mainly originates from a few recordings, where the two cardiologists interpret differently the border definition on the right ventricle side of the septum. This

is in line with the recommendations [2], where this difficulty of correctly detecting the right ventricle side septal border in B-mode images is addressed by suggesting M-mode based analysis.

The semi-automatic method in [3] used apical images to measure septal thickness and reported a bias of 0.12mm and a standard deviation of the error of 0.72mm in the mid segments of the septum. It should be noted that the use of apical images is not recommended for measuring septal thickness [2], and the authors did not state whether the manual measurements were made by a cardiologist, nor how many observers there were. The authors used recordings from 12 healthy volunteers.

The algorithm performed fully automatically in 29 of the 37 cases (78.4%). In case of the hypertrophic data 3 of 5 cases needed correction. This suggests that the convergence radius of the model combined with the depth initializer does not work well enough to cover all anatomical variations.

The computation time suggests that real-time operation is feasible on laptop computers. Provided that the computational capacity of the pocket-sized systems is approaching that of a regular laptop computer, the algorithm is suitable for real-time operation also on these systems. If, instead, the algorithm is chosen as a post-processing tool, it is not necessary to process all frames. It would be sufficient to use the ED and some preceding frames.

This work has some limitations. One problem is that the results of the fully automatic operation were not separated from the total results. So even if a feasibility for automatic operation of 78.4% is claimed, the acurracy of the fully automatic numbers has not been presented separately. Another limitation is that the total number of patients in the feasibility study is limited, and only 5 cases with hypertrophy were found in the available data material. This is likely caused by previously diagnosed hypertension being an exclusion criterion in the HUNT study [12], and hypertension is the most frequent cause of septal hypertrophy [16]. Another limitation is that the septal thickness interobserver variability numbers found in the literature, are based on M-mode. Thus, there is some uncertainty how this translates to B-mode measurements. In addition, even if the algorithm was designed for pocket-sized ultrasound devices, it has not yet been tested on such a device. The algorithm currently relies on ECG input to find end diastole. On truly pocket-sized devices, such as Acuson P10 or GE Vscan, no ECG is available and a different way of establishing end diastole must be considered. Moreover, the target user population of the algorithm is the group of inexperienced users of ultrasound, while in this work the images were acquired by a trained cardiologist.

Future work should focus on improving the initialization procedure. A more robust method of detecting the septum position, or a landmark close to the septum, could possibly be developed to yield a fully automatic solution. Alternatively, other solvers than the extended Kalman filter, such as an unscented Kalman filter [17], could be explored, to see whether the convergence radius of the model can be increased without compromising the computational efficiency of the current solution.

4.6 Summary and Conclusions

The proposed algorithm was used to measure the septum thickness in randomly selected patients from a database containing imagery with similar quality as expected in a clinical practice. The algorithm has proven to be computationally efficient, and the accuracy is comparable to that of manual B-mode measurements performed by two cardiologists. It overcomes the problem of moderator band and/or trabeculae in the majority of the cases. It provides a fast indication of septal hypertrophy, but the IVSd measurement value should be presented together with an image of the measurement caliper line for visual approval, especially in patients for which the image quality is suboptimal. In principle, the algorithm is fully automatic. In practice, the automatic initialization failed in 21.6% of the cases and required manual re-initialization. As the error is easily corrected, this does not significantly alter the usability of the algorithm, even for inexperienced users.

Acknowledgment

The authors would like to thank the Norwegian Research Council for funding the project and the staff at GE Global Research in Bangalore and Niskayuna for fruitful discussions on the topic automatic septum thickness measurements.

Conflict of interest statement

Fredrik Orderud is now employed by GE Vingmed Ultrasound. Professor Hans Torp has been hired as a consultant for GE Vingmed Ultrasound.

References

[1] G. Mancia, G. De Backer, A. Dominiczak, R. Cifkova, R. Fagard, G. Germano, G. Grassi, A. M. Heagerty, S. E. Kjeldsen, S. Laurent, K. Narkiewicz, L. Ruilope, A. Rynkiewicz, R. E. Schmieder, H. A. Boudier, A. Zanchetti, A. Vahanian, J. Camm, R. De Caterina, V. Dean, K. Dickstein, G. Filippatos, C. Funck-Brentano, I. Hellemans, S. D. Kristensen, K. McGregor, U. Sechtem, S. Silber, M. Tendera, P. Widimsky, J. L. Zamorano, S. Erdine, W. Kiowski, E. Agabiti-Rosei, E. Ambrosioni, L. H. Lindholm, M. Viigimaa, S. Adamopoulos, E. Agabiti-Rosei, E. Ambrosioni, V. Bertomeu, D. Clement, S. Erdine, C. Farsang, D. Gaita, G. Lip, J. M. Mallion, A. J. Manolis, P. M. Nilsson, E. O'Brien, P. Ponikowski, J. Redon, F. Ruschitzka, J. Tamargo, P. van Zwieten, B. Waeber, and B. Williams, "2007 guidelines for the management of arterial hypertension: The task force for the management of arterial hypertension of the european society of hypertension (esh) and of the european society of cardiology (esc)," *J Hypertens*, vol. 25, no. 6, pp. 1105–87, 2007.

[2] R. Lang, M. Bierig, R. Devereux, F. Flachskampf, E. Foster, P. Pellikka, M. Picard, M. Roman, J. Seward, and J. Shanewise, "Recommendations for chamber quantification: A report from the american society of echocardiography's guidelines and standards committee and the chamber quantification writing group, developed in conjunction with the european association of echocardiography, a branch of the european society of cardiology," *Journal of the American Society of Echocardiography*, vol. 18, pp. 1440–1463, Dec 2005.

[3] H. Moladoust, M. Mokhtari-dizaji, Z. Ojaghi-haghighi, F. Noohi, A. Khaledifar, and H. Grailu, "Determination of instantaneous interventricular septum wall thickness by processing sequential 2d echocardiographic images," *Pakistan Journal of Biological Sciences*, vol. 10, pp. 454–461, Mar 2007.

[4] F. Orderud and S. I. Rabben, "Real-time 3d segmentation of the left ventricle using deformable subdivision surfaces," in *Computer Vision and Pattern Recognition, IEEE Computer Society Conference on*, (Los Alamitos, CA, USA), pp. 1–8, IEEE Computer Society, June 24-26 2008.

[5] A. Blake, R. Curwen, and A. Zisserman, "A framework for spatio-temporal control

in the tracking of visual contours," *Int. J. Comput. Vis.*, vol. 11, no. 2, pp. 127–145, 1993.

[6] A. Blake, M. Isard, and D. Reynard, "Learning to track the visual motion of contours," *Artificial Intelligence*, vol. 78, pp. 179–212, Oct 1995.

[7] G. Jacob, J. A. Noble, M.-P. M. , and B. A. , "Evaluating a robust contour tracker on echocardiographic sequences," *Med. Image Anal.*, vol. 3, pp. 63–75, 1999.

[8] G. Jacob, J. Noble, C. Behrenbruch, A. Kelion, and A. Banning, "A shape-space-based approach to tracking mycordial borders and quantifying regional left-ventricular function applied in echocardiography," *IEEE Trans. Med. Imag.*, vol. 21, pp. 226–238, Mar 2002.

[9] L. Piegl and W. Tiller, *The NURBS Book*. Springer Verlag, 1995.

[10] D. Hearn and P. Baker, *Computer Graphics with OpenGL*. Pearson Prentice Hall, 3rd ed., 2004.

[11] A. H. Barr, "Global and local deformations of solid primitives," *ACM SIGGRAPH Computer Graphics*, vol. 18, pp. 21–30, Jul 1984.

[12] H. Dalen, A. Thorstensen, S. A. Aase, C. B. Ingul, H. Torp, L. J. Vatten, and A. Stoylen, "Segmental and global longitudinal strain and strain rate based on echocardiography of 1266 healthy individuals: the hunt study in norway," *Eur J Echocardiogr*, vol. 11, no. 2, pp. 176–83, 2010.

[13] A. Thorstensen, H. Dalen, B. H. Amundsen, S. A. Aase, and A. Stoylen, "Reproducibility in echocardiographic assessment of the left ventricular global and regional function, the hunt study," *Eur J Echocardiogr*, vol. 11, no. 2, pp. 149–56, 2010.

[14] J. S. Gottdiener, S. V. Livengood, P. S. Meyer, and G. A. Chase, "Should echocardiography be performed to assess effects of antihypertensive therapy? test-retest reliability of echocardiography for measurement of left ventricular mass and function," *Journal of the American College of Cardiology*, vol. 25, no. 2, pp. 424 – 430, 1995.

[15] D. J. Sahn, A. DeMaria, J. Kisslo, and A. Weyman, "Recommendations regarding quantitation in m-mode echocardiography: results of a survey of echocardiographic measurements," *Circulation*, vol. 58, no. 6, pp. 1072–1083, 1978.

[16] D. Harpaz, T. Rosenthal, E. Peleg, and A. Shamiss, "The correlation between isolated interventricular septal hypertrophy and 24-h ambulatory blood pressure monitoring in apparently healthy air crew," *Blood Pressure Monitoring*, vol. 7, no. 4, pp. 225–229, 2002.

[17] S. Julier and J. Uhlmann, "A new extension of the Kalman filter to nonlinear systems," in *Int. Symp. Aerospace/Defense Sensing, Simul. and Controls*, pp. 182–193, 1997.

Chapter 5

Echocardiography without ECG

Svein Arne Aase[1], Sten Roar Snare[1], H˚avard Dalen[1,4],

Asbjørn Støylen[1,2], Fredrik Orderud[3] and Hans Torp[1]

[1] Dept. Circulation and Medical Imaging, NTNU
[2] Dept. Cardiology, St. Olav Hospital, Trondheim, Norway
[3] GE Vingmed Ultrasound, Horten, Norway
[4] Levanger Hospital, Nord-Trøndelag Health Trust, Levanger, Norway

Chapter 6

Automatic Real-time View Detection

Sten Roar Snare[1], Svein Arne Aase[1], Ole Christian Mjølstad[1,2], Håvard Dalen[4], Fredrik Orderud[3], and Hans Torp[1]
[1] Dept. Circulation and Medical Imaging, NTNU
[2] Dept. Cardiology, St. Olav Hospital, Trondheim, Norway
[3] GE Vingmed Ultrasound, Horten, Norway
[4] Levanger Hospital, Nord-Trøndelag Health Trust, Levanger, Norway

This work presents an algorithm capable of classifying an echocardiographic view as either an apical two chamber view, four chamber view or long axis view. It also provides a score on the overall image quality.
The algorithm is based on a deformable non uniform rational B-spline (NURBS) model updated in an extended Kalman filter framework. Models are constructed for each of the three standard views. Each model is updated using a combination of edge and speckle-tracking measurements, where weak edges and edges strongly deviating from their neighbor edges are discarded. The most probable standard view is found using feature detection and general successfulness in detecting edges. This is also used as a measure of overall view quality.
The algorithm was trained and validated using 68 recordings from the Norwegian HUNT database. An echocardiographer classified each recording as one of three standard views. 33 randomly chosen recordings, with approximately 10 of each view, were used for training. The other 35 recordings were used for validation. The algorithm successfully classified the view in 32 of 37 cases (86.5%). Each classification is accompanied by a score, which can be used to assess image quality.

6.1 Background

When a non-experienced user of ultrasound is to do an examination, he will run into three main challenges

- Getting a standard view of acceptable image quality

- Extracting qualitative information from the image
- Extracting reliable and repeatable quantitative information from the image

The future ultrasound systems should aid the user in overcoming these challenges. Getting the correct view can here be said to be the fundamental problem and acts as a preequisute for the other two challenges.

This work targets to aid the user in recognizing a standard view and to give the automatic algorithms a way to recognize when they have an image acceptable for analysis. The approach is model-based using non-uniform rational b-splines and an extended Kalman filter. It works by fitting models of the common standard views to real-time image data.

6.1.1 Prior Work

Some prior work has been presented on automatic view detection for cardiac images. In [1], the authors present an algorithm based on a model template fit using parts-based representation. The different parts are described using appearance modeling and they are interconnected by spring-like models. They apply the Gray-Level Symmetric Axis Transform to identify the chambers and use Markov Random Fields to model how the chambers are related to each other. The classification itself is done using a support vector machine classifier and leave-one-out cross validation. They achieved an accuracy up to 88.35%.

The authors in [2] present an algorithm based on multiresolution elastic registration. When merging the apical two chamber and four chamber views, they achieve an accuracy of 93%. Classification into all four classes (apical two and four chamber, parasternal short and long axis) yielded an accuracy of 90%. Their algorithm may need several templates for each view, in order to cover all the variations in anatomy and operator skills.

Otey et al. [3] use a hierarchical classification approach where they first classify the imaging window (apical, parasternal) and then do a second classification for each imaging window. The overall accuracy on their test data is 90.9%.

The, to our best knowledge, most recent publication addressing cardiac view detection, is the work by Park et al. [4]. They have published a solution based on machine learning from an annotated database. The results are impressive with a classification accuracy of 96% and a computation time of less than one second on a desktop computer.

This work is based on Orderud et al [5], who published work on automatic alignment of standard views in 3D using an extended Kalman filter. It also has some similarities to the work by [1]. The advantage of this solution is that it operates in real time, and that the number of models/templates will be exactly the same as the number of views to classify.

6.2 Algorithm

6.2.1 Parametric model

The applied parametric models are based on Non-Uniform Rational B-splines (NURBS). This is a generalization of the commonly used nonrational B-splines, [6].

$$\mathbf{p}_l(u) = \frac{\sum_{i=0}^{n} N_{i,k}(u) w_i \mathbf{q_i}}{\sum_{i=0}^{n} N_{i,k}(u) w_i}, a \leq u \leq b \tag{6.1}$$

$N_{i,k}(u)$ are the k'th-degree B-spline basis functions. $\mathbf{q_i}$ are the control points for the spline. Lastly, w_i are the weights of the NURBS curve. We denote points on the NURBS curve as $\mathbf{p}_l(u)$.

By carefully selecting the control points, weights and knot vector, it is possible to represent a large variety of curves. The knot vector has been chosen such that $u_{k+1}, \ldots, u_{m-k-1}$ are linearly distributed.

Complex models are made by combining different NURBS curves. The three considered standard views are apical four chamber (A4CH), apical two chamber (A2CH) and apical long axis (APLAX). The views are described in [7] and [8].

An A4CH is identified by the presence of four cavities. These are the left atrium (LA), right atrium (RA), left ventricle (LV) and right ventricle (RV). Each of the cavities is modeled by a closed cubic NURBS curve, using 12 control points of which 8 are allowed to move. An example of the LV model is shown in figure 6.1. The presence of RV is a strong marker for this view, and this has been reflected in the view scoring system.

The A2CH consists of LA and LV. There are no easy markers for this view, and the model may very well fit both to APLAX and A4CH views.

The APLAX is best identified by the presence of an aortic outlet tract. Thus, this model consists of LA and LV, as well as a model of the outlet tract.

6.2.2 Kalman tracking framework

The Kalman filter contour tracking framework is based on an extension of the software published by Orderud et. al, [9], supporting NURBS.

System states

A Kalman filter requires the model or system to be described by states. We choose to denote the normal displacement of the control vertices as the local states, $\mathbf{x}_l$. A control point can be written as:

$$\mathbf{q}_i = \bar{\mathbf{q}}_i + x_{l,i}\mathbf{n}_i \tag{6.2}$$

where $\mathbf{n}_i$ is the normal displacement vector for the control vertex and $\bar{\mathbf{q}}_i$ is the mean position of the control vertex. The pose parameters (translation, rotation and scale) are used as global states, $\bar{\mathbf{x}}_\mathbf{g}$. Combining the local and global states, yields $\mathbf{x} = [\mathbf{x}_l\, \mathbf{x}_g]$.

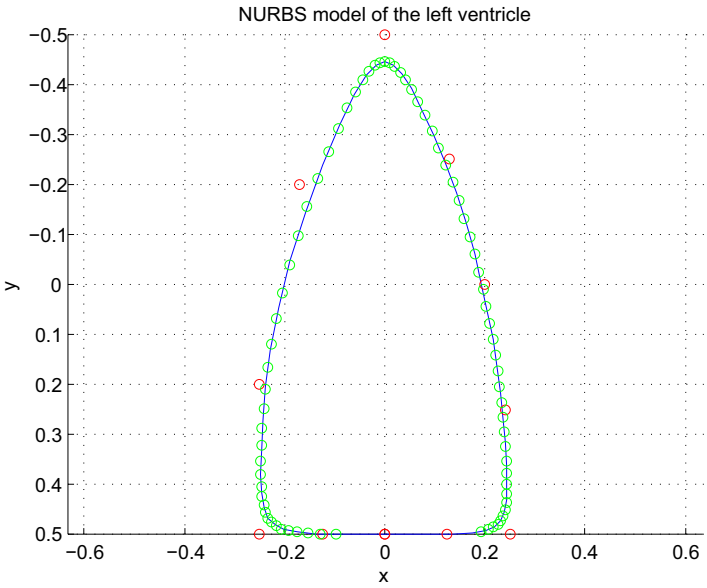

Figure 6.1: NURBS model of the left ventricle, using 12 control points of which 8 are allowed to move

The relation between the system states and the points on the deformable model is likewise described by a local (T_l) and global transform (T_g). We denote the points on the final contour as $\mathbf{p}$. Points on the contour prior to application of the global pose are written as $\mathbf{p}_l$. We define a vector $\mathbf{u}$ with length N_c where $0 \leq u_i \leq 1$. This yields:

$$\mathbf{p}_l = [p_l(u_0), p_l(u_1), \ldots, p_l(u_{N_c-1})] \tag{6.3}$$

where $p_l(u_i)$ is evaluated using equation 6.1. This defines the local transformation T_l. $\mathbf{p}_l$ is then transformed by the global pose transform, T_g to get the correct position of the model.

$$\mathbf{p} = T_g(\mathbf{p}_l, \mathbf{x_g}) \tag{6.4}$$

The composite deformation model, $\mathbf{T}$ includes both the local and global transforms. It is necessary to calculate the Jacobian of T. The local Jacobian matrix can easily be found by multiplying the displacement vectors with their respecitve basis functions:

$$\mathbf{J}_l = [b_{i_0}\mathbf{n}_{i_0}, b_{i_1}\mathbf{n}_{i_1}, \ldots] \tag{6.5}$$

This can be precomputed, and thus eases the real-time operation. The global T_g transform can be applied directly to curve points, as in 6.4. The overall Jacobian

matrix can be derived applying the chain-rule of multivariate calculus:

$$\mathbf{J}_g = \left[\frac{\partial T_g(\mathbf{p}_l, \mathbf{x}_g)}{\partial \mathbf{x}_g}, \frac{\partial T_g(\mathbf{p}_l, \mathbf{x}_g)}{\partial \mathbf{p}_l} J_l \right] \tag{6.6}$$

Prediction

During the prediction step, the state estimates are predicted based on the posterior estimates from last iteration.

$$\bar{\mathbf{x}}_{k+1} = A\hat{\mathbf{x}}_k \tag{6.7}$$

Measurements

As input to the Kalman filter, a combination of edge measurements and block matching has been used. The edge measurements are performed along the curve normals. N_p edge points are distributed around the NURBS model. For each edge point, it is searched for an intensity transition along a normal to the NURBS curve in this point. The distance from the edge point to the measured measured edge point is called a *normal displacement* measurement v. The displacements are also weighted by a measure of edge confidence. The measure used is the mean-square error (MSE) between the transition model (step) and the sample data. Edge measurements with a very high MSE are marked as invalid and discarded.

$$v = \mathbf{n}^T(\mathbf{p}_{obs} - \mathbf{p}) \tag{6.8}$$

This measurement must be converted to state space, in order to be useful for the state update. The measurement model must be linear to fit in the Kalman filter framework. This is done using the normal vector projection of the Jacobian:

$$\mathbf{h}^T = \mathbf{n}^T\mathbf{J} \tag{6.9}$$

The normal displacement measurements are thus now related to the state vector through $\mathbf{h}^T$.

In addition to the edge measurements, block matching has been used to track movement. N_t points on the NURBS model are selected as centres for the block matching blocks. These points are tracked using regular SAD block matching. The normal component of the displacement vector between consecutive frames is used as a measurement in a same manner as for edge detection. This is very similar to the work in [10], except that the control points again are restricted to move in the normal direction only. This use of block matching is not strictly necessary, but adds to the robustness of the method.

Assimilation and update

The measurements are assimilated into *information space* to save computation time. The Kalman gain and the update step is then calculated. See for instance [9] or [11] for more details.

6.3 View scoring

The scoring is based on the number of failing edge detections during a heart cycle. If the model has a poor fit, more of the edge detection search normals will fail to include an edge. If the edge detector fail more often in some regions than others, this can be used to assess regional fit. As explained in the Parametric model section 6.2.1, the different models are identified by some features. For the A4CH, the model score is first calculated individually for each chamber, $S_{LA}, S_{RA}, S_{LV}, S_{RV}$. The score is calculated using the number of failing edges Nf divided by the number of edge detection points in each model Ne. In addition, a set of rules is applied to the scores. Poorly visible atria are thresholded to zero, to allow for zoomed images:

$$\begin{aligned} S_X &= \begin{cases} 1 - \frac{Nf_X}{Ne_X} & \text{if } 1 - \frac{Nf_X}{Ne_X} > T_X \\ 0 & \text{otherwise} \end{cases} \\ X &= \{LA, RA\} \end{aligned} \tag{6.10}$$

A fairly well visible RV is given priority by adding a gain to the score, K_{RV}, when the score is above a certain threshold, T_{RV}:

$$S_{RV} = \begin{cases} 1 - \frac{Nf_{RV}}{Ne_{RV}} + K_{RV} & \text{if } 1 - \frac{Nf_{RV}}{Ne_{RV}} > T_{RV} \\ 1 - \frac{Nf_{RV}}{Ne_{RV}} & \text{otherwise} \end{cases} \tag{6.11}$$

The LV is not given special priority as it is present in all standard views:

$$S_{LV} = 1 - \frac{Nf_{LV}}{Ne_{LV}} \tag{6.12}$$

The total A4CH score is then given by:

$$S_{A4CH} = min \begin{cases} 0.5\,(S_{LV} + S_{RV}) + S_{LA} + S_{RA} \\ 1 \end{cases} \tag{6.13}$$

The APLAX is handled in a similar manner. The LV and LA scores are calculated as for the four chamber case. In addition, there is an aortic outlet tract model. Detection of the tract adds to the score, while lack of detection reduces score:

$$S_{AO} = \begin{cases} -K_{AO} & \text{if } 1 - \frac{Nf_{AO}}{Ne_{AO}} < T_{AO} \\ K_{AO} & \text{otherwise} \end{cases} \tag{6.14}$$

The total score is then calculated as:

$$S_{APLAX} = min \begin{cases} 0.7\,S_{LV} + 0.3\,S_{LA} + S_{AO} \\ 1 \end{cases} \tag{6.15}$$

For the A2CH view, the LV and LA score are calculated as for the other models. The total score is calculated as:

$$S_{APLAX} = 0.7\,S_{LV} + 0.3\,S_{LA} \tag{6.16}$$

Table 6.1: Parameters for the view detection algorithm

Model	Parameter	Value
A4CH	T_{LA}	0.50
	T_{RA}	0.20
	T_{RV}	0.50
	K_{RV}	0.50
APLAX	T_{LA}	0.00
	T_{RA}	0.00
	T_{AO}	0.40
	K_{AO}	0.33
A4CH	T_{LA}	0.00
	T_{RV}	0.00

Table 6.2: Overall results shown as percentage successfull classifications.

Total Performance	86.5 %
A4CH Performance	86.7 %
A2CH Performance	90.9 %
APLAX Performance	81.8 %

6.4 Results

The algorithm has been tested and validated using 68 recordings from the Norwegian HUNT database. The data are from volunteers (age 31-79 years)free from known cardiovascular disease, diabetes or hypertension. A cardiologist examined the 68 recordings and classified them as one of the three standard apical views. 33 randomly chosen recordings from the set, were used as training set. The algorithm was tuned to perform well on the training set. The parameters chosen are shown in table 6.1. The computation time per view model is less than 6ms on a desktop computer and is thus suitable for realtime implementation. It should also be possible to achieve a total running time of less than N*6ms where N is the number of view templates.

The algorithm was then tested using a test set of 37 recordings. No tuning was done using these data. The results are presented in table 6.2 and 6.3.

6.5 Discussion

The overall success rate of the algorithm was 86.5%. In this test, it failed most often for the APLAX. The data material is not large enough to decide whether this will always be the case. The algorithm has a challenging task of correctly identifying

Table 6.3: Classification results. Bold numbers indicate the number of correct classifications.

		Model		
		A4CH	A2CH	APLAX
View	A4CH	**13**	2	0
	A2CH	1	**10**	0
	APLAX	0	2	**9**

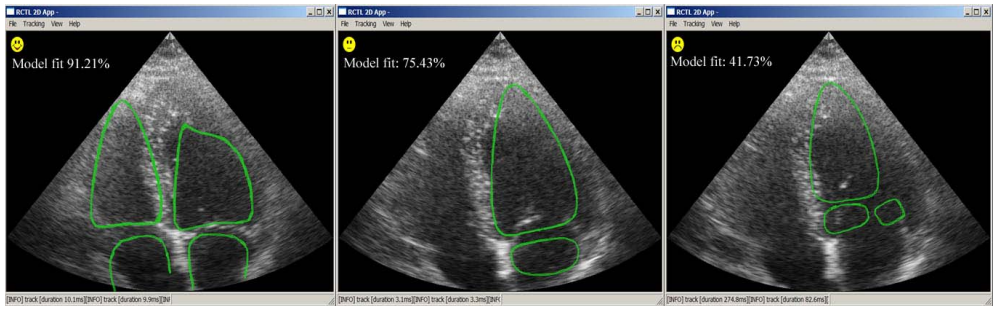

Figure 6.2: Example of an A4CH classification. The A4CH is 91.2%, the A2CH score is 75.4% and the APLAX score is 41.7%. The view is classified as A4CH, and the score of 91% indicates a good image quality

the A2CH. The scores for the A2CH views are typically lower than for APLAX and A4CH. This is due to the lack of landmarks to be used in the calculation of the scores. The difference between scores is lower for the A2CH identification than for the other models. Still, the algorithm only failed for one A2CH recording.

For A4CH and APLAX, the correct view most often has a score much higher than for the other models. The identification typically fails when a landmark is not detected, for instance when the image quality in the basal region of an APLAX image is so poor that the aortic outlet tract is not detected. The other failure mode is when another model incorrectly detects a landmark which is not present. This may occur for instance in the A2CH or APLAX views, when sometimes there is a hypoechoic region to the left of the pericardium. This region is occasionally identified as RV, causing the view to be classed as A4CH. As it has been chosen to allow incomplete atria, this situation can not directly be avoided using the presence of RA.

When it comes to judging the quality of the view, the scores give a repeatable indication. The emphasis is on landmarks. That means a view is given a higher score the more landmarks that are detected. This will give priority to the positioning of the view and less priority to the overall image quality. This can easily be changed to suit the particular needs of each application. A challenge still remaining is to successfully

differ between a correct view of poor image quality and an incorrect view with good image quality. This is especially the case for the A2CH views.

The method should easily expand to fit parasternal views, by fitting new models. Because these models will look different from the apical models, it is less likely that they will have large impact on the success rate on the apical views.

6.6 Conclusions

A novel method for automatic detection of the imaging view in cardiac ultrasound using the apical probe position has been presented. The system has a success rate of 86.5% when tested with realistic ultrasound data. The algorithm is extendable to other probe positions. The system may be used as feedback to the user, or as a preprocessing step for automatic algorithms supporting diagnosis.

References

[1] S. Ebadollahi, S.-F. Chang, and H. Wu, "Automatic view recognition in echocardiogram videos using parts-based representation," in *IEEE Conference on Computer Vision and Pattern Recognition, 2004*, pp. 2–9, 2004.

[2] S. V. Aschkenasy, C. Jansen, R. Osterwalder, A. Linka, M. Unser, S. Marsch, and P. Hunziker, "Unsupervised image classification of medical ultrasound data by multiresolution elastic registration," *Ultrasound in Medicine and Biology*, vol. 32, pp. 1047–1054, 2006.

[3] M. E. Otey, J. Bi, S. Krishnan, B. Rao, J. Stoeckel, A. Katz, J. Han, and S. Parthasarathy, "Automatic view recognition for cardiac ultrasound images," in *Proceedings of Int'l Workshop on Computer Vision for Intravascular and Intracardiac Imaging*, pp. 187–194, 2006.

[4] J. Park, S. Zhou, C. Simopoulos, J. Otsuki, and D. Comaniciu, "Automatic cardiac view classification of echocardiogram," in *Computer Vision, 2007. ICCV 2007. IEEE 11th International Conference on*, pp. 1–8, Oct. 2007.

[5] F. Orderud, H. Torp, and S. I. Rabben, "Automatic alignment of standard views in 3d echocardiograms using real-time tracking," vol. 7265, pp. 72650D+, SPIE, 2009.

[6] L. Piegl and W. Tiller, *The NURBS book*. London, UK: Springer-Verlag, 1995.

[7] S. D. Solomon and B. E. Bulwer, *Essential echocardiography: a practical handbook with DVD*. Totowa, N.J.: Humana Press, 2007. Title from e-book title screen (viewed October 15, 2007).

[8] E. Braunwald and D. P. Zipes, *Braunwald's heart disease: a textbook of cardiovascular medicine*. Philadelphia: Elsevier Saunders, 2005. 7th ed.

[9] F. Orderud and S. I. Rabben, "Real-time 3d segmentation of the left ventricle using deformable subdivision surfaces," in *Computer Vision and Pattern Recognition, IEEE Computer Society Conference on*, (Los Alamitos, CA, USA), pp. 1–8, IEEE Computer Society, June 24-26 2008.

[10] F. Orderud, G. Kiss, S. Langeland, E. Remme, H. Torp, and S. Rabben, "Real-time left ventricular speckle-tracking in 3d echocardiography with deformable subdivision surfaces," in *MICCAI workshop on Analysis of Medical Images*, pp. 41–48, 2008.

[11] Y. Bar-Shalom and X.-R. Li, *Estimation with Applications to Tracking and Navigation*. New York, NY, USA: John Wiley & Sons, Inc., 2001.

Chapter 7

Real-time Scan Assistant for Echocardiography

Sten Roar Snare[1], Hans Torp[1], Fredrik Orderud[3], and Bjørn Olav Haugen[1,2]
[1] Dept. Circulation and Medical Imaging, NTNU
[2] Dept. Cardiology, St. Olav Hospital, Trondheim, Norway
[3] GE Vingmed Ultrasound, Oslo, Norway

A real-time scan assistant (SA) for use with echocardiography is presented. The motivation is to aid non-expert users to capture apical 4-chamber views (A4CH) during echocardiography.
The algorithm is based on a parametric multi-chamber model of the A4CH view, updated in an extended Kalman filter framework. The regional model goodness of fit is used to calculate a score, which together with an icon (emoticon), is provided in real-time to the user, indicating whether the current view is acceptable or not.
The SA was implemented on a commercially available scanner. A feasibility test was performed using two healthy volunteers as models and 10 medical students to act as non-expert users. The students examined the models at two occasions, separated more than four days in time. Half of the students used the SA during the first exam and no SA at the second exam. The other half did it the other way around. The recordings were later rated by a cardiologist. A Wilcoxon Signed Pair Rank test revealed a statistically significant improvement when using SA. Nine cases were rated as poor without using the SA. In eight (89%) of these cases, view quality improved to acceptable when the SA was used.

7.1 Introduction

Because of the increasing number of small, portable and low-cost ultrasound systems emerging on the market, it is expected that future scanners will be operated also by less experienced users of ultrasound. When a non-expert user of ultrasound is to do a cardiac examination, he will run into three main challenges:

- Getting a standard view of acceptable image quality.
- Extracting qualitative information from the image.
- Extracting reliable and repeatable quantitative information from the image.

Future ultrasound systems should aid the user in overcoming these challenges. Getting a good view is the fundamental problem. This work has focused on acquisition of the apical 4-chamber view (A4CH), traversing both ventricles and atria through the mitral and tricuspidal valves, as this is one of the most informative views in echocardiography.

Little work has been published on real-time user feedback for image improvement during ultrasound scanning. In [1], the authors presented an indicator for the acoustic contact between the probe and the object of interest. This approach can be used to warn the user of a poor acoustic window due to ribs or lack of acoustic gel, but no information about the view is provided.

View detection is a topic frequently encountered in the echocardiographic research literature. The target is to automatically differentiate between standard views for sorting databases of recordings, or for use with measurement and analysis software. These are typically offline solutions based on classification schemes [2], often combined with image registration [3] or template fitting [4]. The approach in [5] was based on machine learning from an annotated database.

The authors in [6] published work on a highly efficient algorithm for automatic alignment of standard views in 3D echocardiography using an extended Kalman filter. This approach was modified to suit 2D view detection in [7], where it was also forecasted that a real-time implementation was feasible.

In this work we modify the approach in [7] and present a scan assistant (SA) algorithm for aiding the user *during acquisition*. In the following, the algorithm is presented in detail. Results from a feasibility test where 10 medical students used the SA when scanning two healthy volunteers are also provided.

7.2 Algorithm

The algorithm is based on a real-time adaption of a template view model to the image data. During acquisition, the user is shown a score for how close the current view resembles a standard A4CH view. The score is derived by measuring the model's quality of fit. In the following sections we present the parametric model, the Kalman filter framework used for updating the model and the view scoring scheme.

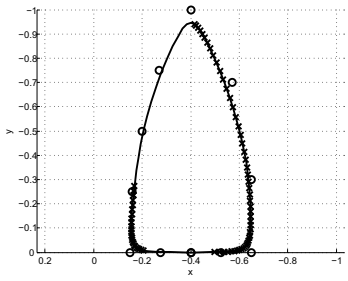

(a) Right Ventricle Model

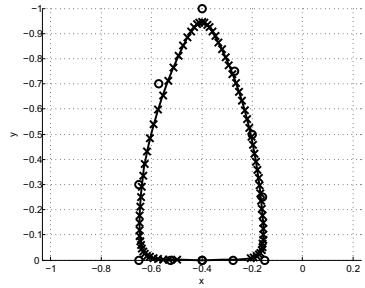

(b) Left Ventricle Model

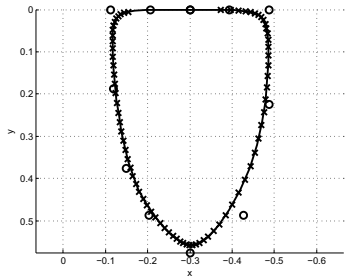

(c) Atrium Model

Figure 7.1: NURBS models of the cardiac chambers. All models are using 12 control points, of which 8 are allowed to move. The densely spaced x-marks represent edge detector points. Note that the base of the models and the right ventricular free wall do not have edge detectors

7.2.1 Parametric model

The applied parametric models are based on Non-Uniform Rational B-splines (NURBS). This is a generalization of the commonly used nonrational B-splines [8].

$$b_{i,k}(u) = \frac{N_{i,k}(u)w_i}{\sum_{j=0}^{n} N_{j,k}(u)w_j}, u_{low} \leq u \leq u_{high} \tag{7.1}$$

$$\mathbf{p}_l(u) = \sum_{i=0}^{n} b_{i,k}(u)\mathbf{q_i}, u_{low} \leq u \leq u_{high} \tag{7.2}$$

$b_{i,k}$ are the rational basis functions. $N_{i,k}(u)$ are the k'th-degree B-spline basis functions. The control points for the spline are denoted $\mathbf{q_i}$, the weights of the NURBS curve as w_i and the points on the NURBS curve as $\mathbf{p}_l(u)$. The knot vector has been chosen such that $u_{low} = 0$, $u_{high} = 1$ and $u_{k+1}, \ldots, u_{m-k-1}$ are uniformly distributed.

A more complex view model is made by combining different curves. The A4CH view is described in [9, 10]. It is mainly characterized by the presence of four cavities. These

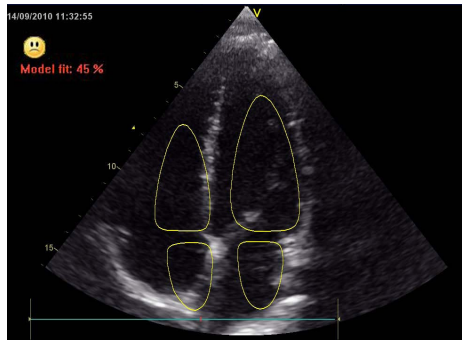

Figure 7.2: Initial fit of the apical 4-chamber view model.

are the left atrium (LA), right atrium (RA), left ventricle (LV) and right ventricle (RV). Each of the cavities is modeled by a closed cubic NURBS curve using 12 control points, of which 8 are allowed to move. The first and last control points are in the middle of the base. The control points in the base are fixed in order to preserve the shape. The same model is used for the left and right atrium. The cavity models are illustrated in Fig. 7.1. The NURBS models are joined by similarity transforms, combining translation, rotation and uniform scaling [11], into a complete *view model*. The LV similarity transform, $\mathcal{T}_{LV}$, is the main transform. The other models each have a dedicated similarity transform positioning them relative to the LV model. This can be written:

$$\begin{aligned} \mathbf{p}_{LV}(u) &= \mathcal{T}_{LV}(\mathbf{p}_{l,LV}(u)) \\ \mathbf{p}_{RV}(u) &= \mathcal{T}_{LV}(\mathcal{T}_{RV}(\mathbf{p}_{l,RV}(u))) \\ \mathbf{p}_{LA}(u) &= \mathcal{T}_{LV}(\mathcal{T}_{LA}(\mathbf{p}_{l,LA}(u))) \\ \mathbf{p}_{RA}(u) &= \mathcal{T}_{LV}(\mathcal{T}_{RA}(\mathbf{p}_{l,RA}(u))) \end{aligned} \tag{7.3}$$

An example of the complete initial model is provided in Fig. 7.2.

7.2.2 Kalman tracking framework

The Kalman filter contour tracking framework is based on an extension of the method published in [12], supporting NURBS.

System states

A Kalman filter requires the model or system to be described by states. The displacement component, normal to the curve, of the control points are denoted as the local states, $\mathbf{x}_l$. A control point can be written as:

$$\mathbf{q}_i = \bar{\mathbf{q}}_i + x_{l,i}\mathbf{n}_i. \tag{7.4}$$

where $\mathbf{n}_i$ is the normal displacement vector and $\bar{\mathbf{q}}_i$ is the mean position of the control point. Some of the similarity transforms parameters are defined as dynamic and used as global states, $\mathbf{x_g}$. More detailled, all the LV similarity transform parameters (translation, rotation, scale) are dynamic, as well as the scale parameters of the atrial similarity transforms ($\mathcal{T}_{RA}, \mathcal{T}_{LA}$). Combining the local and global states, yields $\mathbf{x} = [\mathbf{x}_l^T, \mathbf{x}_g^T]^T$.

The system states and the points on the deformable model are related by the local (T_l) and global transforms (T_g). The local transformation, T_l, converts the control points to model points prior to application of geometric transforms. By considering each cavity model separately and splitting the control points into sets of movable ($\mathcal{M}$) and static ($\mathcal{S}$) points, T_l can be derived from (7.2) as:

$$\begin{aligned} \mathbf{p}_l(u) &= \sum_{i=\mathcal{M}} b_{i,k}(u)(\mathbf{q}_{0,i} + x_{l,i}\mathbf{n}_i) + \sum_{i=\mathcal{S}} b_{i,k}(u)\mathbf{q}_{0,i} \\ \mathbf{p}_l(u) &= T_l(\mathbf{x}_l, u) \end{aligned} \tag{7.5}$$

$\mathbf{p}_l(u)$ is then transformed by the global transform to get the final position of the curve point. The global transform is defined by (7.3) for each of cavity models. In practice, it is found by multiplying basic geometric transformations on matrix form [11]. For simplicity and readability, the model subscripts and the parametric coordinate u are ommited in the following description.

$$\mathbf{p} = T_g(\mathbf{p}_l, \mathbf{x_g}) \tag{7.6}$$

The complete deformation model, T, contains both the local and global transforms. The extended Kalman filter requires knowledge of the Jacobian of T. The local Jacobian matrix is derived from (7.5) and is found by multiplying the displacement vectors with their respective basis functions:

$$\mathbf{J}_l = [b_{i_0}\mathbf{n}_{i_0}, b_{i_1}\mathbf{n}_{i_1}, \ldots]. \tag{7.7}$$

This is precomputed, and thus eases the real-time operation. The global T_g transform is applied directly to curve points, as in (7.6). The overall Jacobian matrix is derived by applying the chain-rule of multivariate calculus:

$$\mathbf{J}_g = \left[\frac{\partial T_g(\mathbf{p}_l, \mathbf{x}_g)}{\partial \mathbf{x}_g}, \frac{\partial T_g(\mathbf{p}_l, \mathbf{x}_g)}{\partial \mathbf{p}_l} J_l \right]. \tag{7.8}$$

Prediction

During the prediction step, the state estimates are predicted based on the posterior estimates from the last iteration:

$$\bar{\mathbf{x}}_{k+1} - \mathbf{x}_0 = \mathbf{A}(\hat{\mathbf{x}}_k - \mathbf{x}_0). \tag{7.9}$$

The $\mathbf{A}$ matrix defines the regularization of the view model.

Measurements

The Kalman filter takes edge measurements performed along curve normals as input. N_p edge points are distributed around each of the NURBS curves. This is illustrated by the densely spaced x-marks in Fig. 7.1. There are no edge detectors in the regions where the valves are expected. The apical part of the right ventricle free wall often suffer from dropouts, and thus the edge detectors in this region have been removed.

For each edge point, it is searched for an intensity transition along a normal to the NURBS curve. The length of the edge search normal implicitly defines the convergence radius of the model. Two different edge detectors have been applied. Most regions of the models use a *step* detector, based on minimization of the sum of square errors (SSE) between a perfect step function and the sample vector taken normal to the model. The lateral wall of the left ventricle and the free wall of the right ventricle are using a *gradient* edge detector, which detects a peak in the derivative of the search vector intensity. The distance from the edge point to the measured measured edge point is called a *normal displacement* measurement v:

$$v = \mathbf{n}^T(\mathbf{p}_{obs} - \mathbf{p}). \tag{7.10}$$

Weak edges are discarded using thresholding of the intensity difference across the detected edge or the distance from the neighboring edge detector results. The inverse of the mean intensity difference across the detected edge point, is used as a measure of edge confidence. The edge measurement must be converted to state space, in order to be useful for the state update. The measurement model must be linear to fit in the Kalman filter framework. This is achieved by using the normal vector projection of the Jacobian:

$$\mathbf{h}^T = \mathbf{n}^T\mathbf{J}. \tag{7.11}$$

The normal displacement measurements are thus now related to the state vector by $\mathbf{h}^T$.

Assimilation and update

The measurements are assimilated into *information space* to save computation time. The Kalman gain and the update step are then calculated as described in [12, 13].

7.2.3 View scoring

The scoring system is based on the number of failing edge detections. If the model has a poor fit, more of the edge detection search normals will fail to include a valid edge. If the edge detection fails more often in some regions than others, this can be used to assess regional fit. As explained in the Parametric model section 7.2.1, the A4CH model consists of four NURBS curves, each representing a cardiac chamber. A model score is first calculated individually for each cavity, $S_{LV}, S_{RV}, S_{LA}, S_{RA}$. The score is calculated using the number of failing edges, Nf, divided by the total number of edge

detection points in each model, Ne:

$$\begin{aligned} S_X &= \begin{cases} 1 - \frac{Nf_X}{Ne_X} & \text{if } 1 - \frac{Nf_X}{Ne_X} > T \\ -K_X & \text{otherwise} \end{cases} \\ X &= \{LV, RV, LA, RA\} \\ K_X &\geq 0 \end{aligned} \tag{7.12}$$

The score is thresholded to a zero or negative number if the result is too poor. This is used to penalize missing or poorly visible cavities. One of the major challenges when acquiring an A4CH view, is to prevent foreshortening of the view. Missing or poorly visible atria is a sign of an oblique cut of the ventricle and should be penalized. This is achieved by increasing the penalty K_{LA} and/or K_{RA}. The total A4CH score is given by a weighted sum:

$$\begin{aligned} S_{A4CH} &= \sum C_X S_X \\ X &= \{LV, RV, LA, RA\} \end{aligned} \tag{7.13}$$

7.3 Implementation and evaluation

The scan assistant was implemented on a GE Vivid E9 (GE Vingmed Ultrasound, Horten, Norway). For visualization, in addition to displaying the score value, an emoticon ("smiley-face") was added to aid the user deciding whether the view was *poor, fair* or *good*. Scores lower than the T_{poor} threshold are reported as poor (sad face). Scores larger than or equal to T_{poor}, but lower than the T_{fair} threshold, are reported as fair (straight face). Scores above T_{fair} are considered good (smiling face). A user option whether or not to display the view template model during acquisition was also included.

The algorithm was tuned using 35 recordings of various quality. Both good A4CH recordings and completely erroneous recordings were used. The view model was adjusted to be stiff. A flexible model would better fit to the cavities, but would also be more prone to error by more easily adapting to faulty views. Two cardiologists scored the recordings as having good, fair or poor quality. The thresholds for the emoticon was set to give a good correspondence with the clinicians judgment. Fair view quality should be interpreted as clinically useful images having some minor defects. The Scan Assistant (SA) parameters identified after tuning are found in Table 7.1.

An example of a good score is given in Fig. 7.3a. Examples of foreshortened and erroneous views are provided in Fig. 7.3b and Fig. 7.3c.

In order to test the assistant for feasibility, 10 medical students from the Medical Faculty (Norwegian University of Science and Technology (NTNU), Trondheim, Norway) were invited to examine two healthy volunteers acting as ultrasound models. The students had previously been through a brief 1-day introductory course in echocardiography with sparse practical training, but were otherwise unfamiliar with use of ultrasound. The first model had easy to moderate acoustic access, while the second had difficult acoustic access. The project was cleared by the local regional

Table 7.1: Parameters for the scan assistance algorithm.

Parameter	Value
T	0.30
K_{LV}	0.00
K_{RV}	0.00
K_{LA}	0.30
K_{RA}	0.00
C_{LV}	0.33
C_{RV}	0.22
C_{LA}	0.22
C_{RA}	0.22
T_{poor}	55
T_{fair}	70

ethics committee. Each of the students examined the models at two different occasions, separated more than 4 days in time.

The first time the students were given a brief theoretical repetition on how to obtain an A4CH view. Half of the students were allowed to use the scan assistant. The other half did a regular scan with the assistant running in the background (hidden from the user). During the second examination, it was done the other way around. After finishing the exams, all students had made recordings with and without use of the scan assistant. When the students used the assistant, they made two recordings. One without displaying the view model, only using the score value and emoticon, and one recording where also the view model was displayed. Upon image store, the score values generated by the view assistant were stored to the dicom file.

An experienced cardiologist scored the stored recordings from 0 to 100%. Scores below 60% were rated poor. Scores from 60 to 70% were rated as fair, while values from 70% and above were considered good. The sequence of recordings was randomized, and the cardiologist was blinded to which of the recordings were taken with the assistant. In order to register the effects of the assistant, the most important defects with each recording were also registered. The improvement in cardiologist scores when using the scan assistant was tested using the exact Wilcoxon Signed Pair Rank test.

7.4 Results

Overall, using the SA with display of the model improved the view quality in 12 of 20 cases (60%). When the model was not displayed, the SA improved the results in 8 of 20 cases (40%). The Wilcoxon Signed Pair Rank test found the improvement when using SA to be significant both when SA was used with ($p = 0.05$) and without

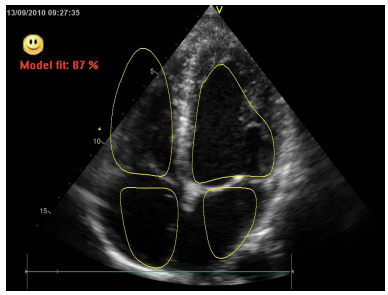

(a) Good view

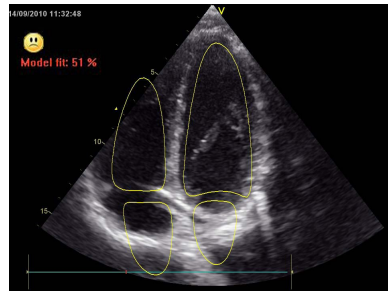

(b) Foreshortened

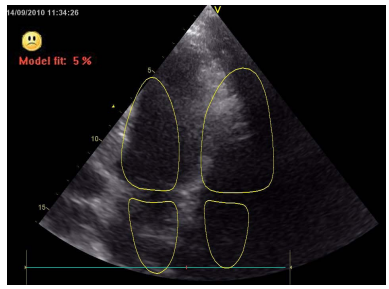

(c) Erroneous view

Figure 7.3: Illustration of one good and two faulty 4-chamber views using the SA with model display. Fig. 7.3a shows a good, convergent view with a score of 87%. In Fig. 7.3b, a foreshortened view is shown, where the atria are missing, and the ventricle is too short. This results in a score of 51%, which is not acceptable. Fig. 7.3c shows another view, which is clearly not a 4-chamber, resulting in a score of only 5%.

($p = 0.029$) model display.

The results of using the SA with displayed model are shown in Fig. 7.4. Eight of nine (89%) cases of poor quality improved to good (3) or fair (5) quality. Another 5 cases improved from fair to good. In five cases, use of SA did not affect the results. In one case the quality remained at the poor level. A degradation of view quality when using SA was observed in 3 cases, whereof one case was from good to poor. All four cases where there was a degradation or continued poor view quality when using the SA, happened with subject 2 when the SA was used during the first session. By only looking at the cases where the SA was used during the second session, the results improved in eight of ten (80%) cases, and the remaining two cases were unchanged at the fair level. Eight of eight (100%) cases of poor quality improved to acceptable quality. The SA generally performed better on patient 1, where there was an improvement in 9 of 10 (90%) cases. One recording stayed unchanged at the good level.

The results when using the SA without showing the model are provided in Fig. 7.5. Five of the nine (55.6%) poor cases improved to fair or good. Three cases improved from fair to good. Elleven cases achieved the same rating with and without use of

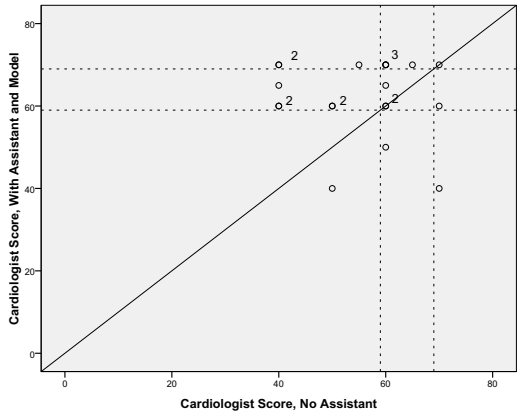

(a) Total

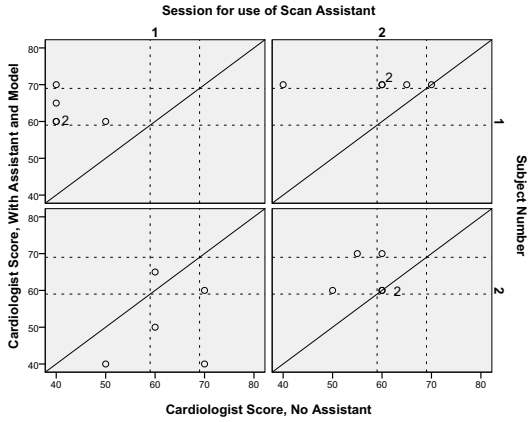

(b) Detailed

Figure 7.4: Improvements when using the Scan Assistant with shown model. Fig. 7.4a presents the overall results. In Fig. 7.4b, the results are split into the two sessions and the two subjects. The stapled lines at 59% and 69% represent the cardiologist limits between poor/fair and fair/good quality.

SA. There was only one case of degradation, which was from good to fair. Four cases remained poor, even when the SA was used. Unlike the results when using SA with shown model, there were no clear differences in SA performance when splitting the results into the different sessions and subjects. Without showing the model, the effect of using SA was similar for both subjects in both sessions.

A summary of the errors in the recordings is presented in Fig. 7.6. There were

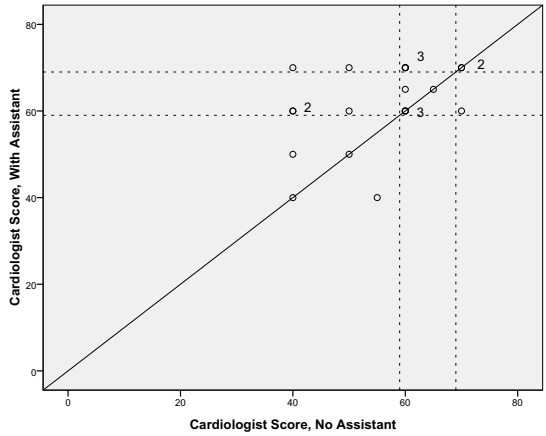

(a) Total

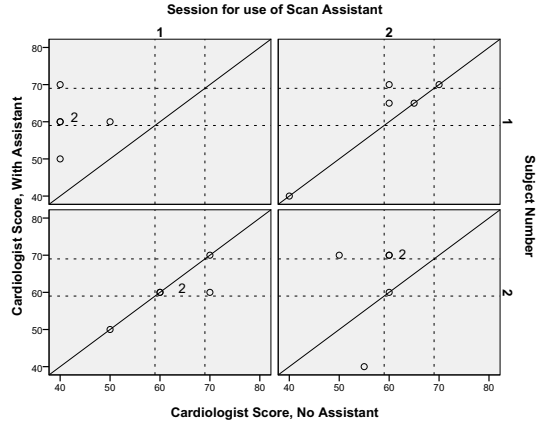

(b) Detailed

Figure 7.5: Improvements when using the Scan Assistant without shown model. Fig. 7.5a presents the overall results. In Fig. 7.5b, the results are split into the two sessions and the two subjects. The stapled lines at 59% and 69% represent the cardiologist limits between poor/fair and fair/good quality.

more reported errors for the SA without the model being shown, compared to SA with shown model. Table 7.2 summarizes the correspondence between the algorithm and cardiologist view rating. It was noted that the time used for an exam frequently increased when the scan assistant was used.

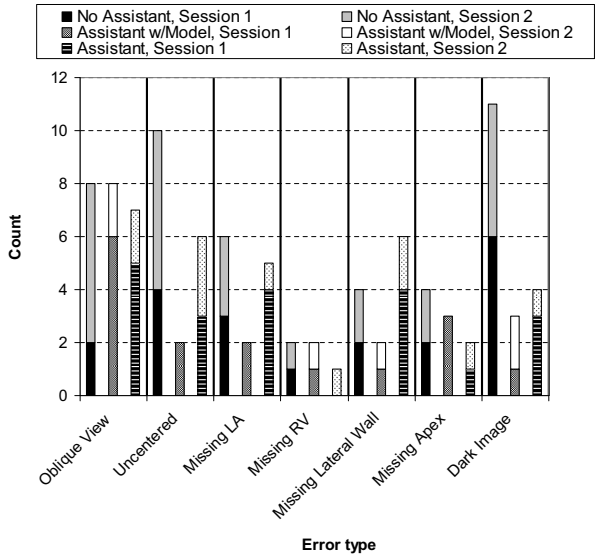

Figure 7.6: Bar diagram illustrating the errors of the recordings.

Table 7.2: Cardiologist versus Assistant evaluation of quality

		Cardiologist		
Assistant		Good	Fair	Poor
	Good	**13 (21.7%)**	11 (18.3%)	3 (5%)
	Fair	5 (8.3%)	**12 (20%)**	4 (6.7%)
	Poor	0	3 (5%)	**9 (15%)**

7.5 Discussion

The view quality improvement in 60% of the cases when showing the model and 40% when not showing the model, indicates that the SA can be a useful tool for non-expert users when acquiring A4CH views. This is also supported by the Wilcoxon Signed Pair Rank test results. In particular the improvements to acceptable views in 89% of the poor cases when showing the model (55.6% without the model), are promising. The students were able to capture acceptable recordings in 85% of the cases with and 80% without showing the model. Without SA, only 55% were considered acceptable.

The four cases where SA with shown model caused a degraded or continued poor view quality were further investigated. The SA recording which caused the worst degradation, from good to poor, was oblique and uncentered. After anonymizing the recording, the cardiologist was confronted with this recording again. He then re-rated it to have fair view quality (60%). Still being a reduction from good quality without SA, the result is less disturbing. The case of reduction from fair to poor was caused by

a SA recording which was oblique and missed the LA. It was also classified as being poor by the algorithm, so a sad face was showing on the screen when the student chose to store the recording. The case of degradation from good to fair view quality was caused by a slightly oblique SA recording. This was not detected by the SA, as the atrial models had adapted to the somewhat deformed atrial cavities present in the recording. In the last case, where the view quality remained poor, the SA recording was oblique, uncentered and missed both the LA and RV. The image was far from an A4CH view, but the models had succeded in partly adapting to cardiac structures/cavities and the SA reported a score of 62%, or fair view quality.

The poor results encountered when examining subject 2 with SA and shown model during the first session were not replicated when using SA without model display. Subject 2 had more difficult acoustic access, and the students struggled to find an acoustic window. It may be that showing the model in this case disturbed the users, who were stressed and put in a new situation. The students who used the SA during the second session knew approximately where to look for the acoustic window and were more familiar with the situation. In this case, display of the model seemed to improve the results. The most frequent error when using SA with shown model, was acquisition of oblique views. Even if the left atrium was missing in only two recordings, eight recordings were labeled as oblique. This indicates that missing atria alone is not sufficient to detect oblique views. Recordings captured using SA without showing the model were more frequently uncentered and missed the LA or LV lateral wall, compared to when the model was shown, see Fig. 7.6. The results related to missing lateral walls can be explained by the differences in centering. When the view template model was shown centered on the screen, the students were focusing more closely on centering the view. In most cases, the resulting view would then also contain the LV lateral wall. The difference in the number of missing left atrias can be related to the students working harder to detect atrial cavities when seeing atrial models on the screen. Unfortunately, as previously discussed, this alone is no guarantee for avoiding foreshortening.

The experiment was expected to be affected by a learning effect, which is why it was chosen to split the group in two, and to wait several days between the sessions. It is not possible to identify any clear learning effect from the results. For subject 1, the students without the assistant made better recordings during the first session. This might have been caused by the varying amount of manual guidance provided during the first session.

Using the SA score values, it can be seen from Table 7.2 that 34 of 60 (56.7%) recordings were correctly classified. All of the seven (11.7%) cases where recordings were considered fair (4) or good (3) by the algorithm and poor by the cardiologist, were related to failed detection of oblique views. The most frequent misclassification occured where the algorithm score indicated good image quality, whereas the cardiologist rating was fair. This happened for elleven recordings, and were mainly caused by failed detection of dark or slightly foreshortened views.

The main challenge for the SA algorithm was correct identification of oblique views. The detection of oblique cuts is a difficult challenge when only using 2D imaging. The algorithm currently fits a stiff atrial model to the image data. When an atrial cavity is

present, the atrial model score will increase and indicate a correct cut of the ventricle volume. In practice, even though the atrial model is stiff, it frequently adapts to deformed or partly visible atria. This causes the SA to mislead the users by reporting a too high score value, and in some cases even misclassify the view quality. Such faulty adaption of atrial models typically occured when the images had good image quality with respect to gain and edge clarity. This is likely related to the fundamental challenge of differing between *view quality* and *image quality*. The SA relies on intensity based information to provide knowledge about the view. The edge detectors either fail because the edge is not present within the range of the model, or because the edge is too weak to be correctly detected. The first situation is view related, while the latter typically occurs when the general image quality is low. The system must be designed to approve a good view having medium image quality. This involves accepting that a number of edges are discarded due to image quality, and puts an upper bound on the discard threshold T. When the system processes a poor view having excellent image quality, edges are only discarded due to the view. In some cases the edge detectors find sufficient spurious edges to overcome the discard threshold, causing an erroneous cavity detection. In addition, the cavities which really are present in the view achieve a very high score. The result is that some foreshortened/oblique views having a high image quality may achieve the same score as a good view having medium image quality.

To the authors knowledge, no similar studies on real-time view assistance have been published, although some of the schemes applied in view classification could perhaps be modified to suit this application. First of all, that would require real-time processing efficiency. Second, a scoring method of each view is needed. The methods in [2–5] are all aiming to classify recordings and do not directly provide knowledge about the "standardness" of the view, nor are they running in real-time.

7.5.1 Limitations and further work

There are some uncertainties related to the pilot study setup. The number of subjects and non-experts was limited. The students were not familiar with echocardiography, except for a one hour mandatory course during their medical education. It was found necessary to provide the students with some repetition and initial guidance during the first session, as some of the students had no practical training. Some of the findings suggest that this may have affected the results. The subjects in this study were healthy volunteers. For future studies it would be interesting to also include patients with pathology, to see whether this influences on the results.

Future algorithmic work should focus on improving the detection of foreshortening/oblique cuts. It would also be interesting to extend the algorithm to the other standard views. An assistant for the parasternal views would be of great interest, in order to prevent non-experts from capturing oblique cuts, causing erroneous visualizations with too small cavities and thick walls.

7.6 Conclusion

A novel method for assisting non-expert users in capturing the apical 4-chamber view in echocardiography has been presented. A Wilcoxon Signed Pair Rank test yielded a statistically significant improvement of the view quality when the scan assistant was used. This was independent of whether the view template model was displayed or not. When displaying the model, use of the scan assistant improved the view quality from poor to fair/good in 8 of 9 (89%) cases. The assistant performed well in all cases except when examining subject two during the first session. This can be an indication that display of the model provided too much information when the users were stressed and unfamiliar with the situation. The results from session two and from subject one, who had easier acoustic access, suggested that showing the model can be beneficial. The results improved from poor to fair/good in 8 of 8 (100%) of the cases. When using the scan assistant and showing the template model, the non-experts captured clinically acceptable recordings in 85% of the cases, compared to 55% without assistance. Although there are still some challenges remaining, in particular with respect to detection of oblique views, the results suggest that use of a real-time scan assistant can improve the results when non-experts are acquiring apical 4-chamber echocardiographic views.

Acknowledgment

The authors would like the medical students who agreed to participate in the study. We would also like to thank GE Vingmed Ultrasound for access to the scanner and its software.

References

[1] L. Løvstakken, F. Orderud, and H. Torp, "Real-time Indication of Acoustic Window for Phased-Array Transducers in Ultrasound Imaging," in *IEEE Ultrasonics symposium - 2007*, (New York), pp. 1549–1552, Citeseer, 2007.

[2] M. E. Otey, J. Bi, S. Krishnan, B. Rao, J. Stoeckel, A. Katz, J. Han, and S. Parthasarathy, "Automatic view recognition for cardiac ultrasound images," in *Proceedings of Int'l Workshop on Computer Vision for Intravascular and Intracardiac Imaging*, pp. 187–194, 2006.

[3] S. V. Aschkenasy, C. Jansen, R. Osterwalder, A. Linka, M. Unser, S. Marsch, and P. Hunziker, "Unsupervised image classification of medical ultrasound data by multiresolution elastic registration," *Ultrasound in Medicine and Biology*, vol. 32, pp. 1047–1054, 2006.

[4] S. Ebadollahi, S.-F. Chang, and H. Wu, "Automatic view recognition in echocardiogram videos using parts-based representation," in *IEEE Conference on Computer Vision and Pattern Recognition, 2004*, pp. 2–9, 2004.

[5] J. Park, S. Zhou, C. Simopoulos, J. Otsuki, and D. Comaniciu, "Automatic cardiac view classification of echocardiogram," in *Computer Vision, 2007. ICCV 2007. IEEE 11th International Conference on*, pp. 1–8, Oct. 2007.

[6] F. Orderud, H. Torp, and S. I. Rabben, "Automatic alignment of standard views in 3d echocardiograms using real-time tracking," vol. 7265, p. 72650D, SPIE, 2009.

[7] S. R. Snare, S. A. Aase, O. C. Mjølstad, H. Dalen, F. Orderud, and H. Torp, "Automatic real-time view detection," in *IEEE Ultrasonics symposium - 2009*, (Rome), pp. 2304–2307, 2009.

[8] L. Piegl and W. Tiller, *The NURBS book*. London, UK: Springer-Verlag, 1995.

[9] S. D. Solomon and B. E. Bulwer, *Essential echocardiography: a practical handbook with DVD*. Totowa, N.J.: Humana Press, 2007. Title from e-book title screen (viewed October 15, 2007).

[10] E. Braunwald and D. P. Zipes, *Braunwald's heart disease: a textbook of cardiovascular medicine*. Philadelphia: Elsevier Saunders, 2005. 7th ed.

[11] D. Hearn and P. Baker, *Computer Graphics with OpenGL*. Pearson Prentice Hall, 3rd ed., 2004.

[12] F. Orderud and S. I. Rabben, "Real-time 3d segmentation of the left ventricle using deformable subdivision surfaces," in *Computer Vision and Pattern Recognition, IEEE Computer Society Conference on*, (Los Alamitos, CA, USA), pp. 1–8, IEEE Computer Society, June 24-26 2008.

[13] Y. Bar-Shalom and X.-R. Li, *Estimation with Applications to Tracking and Navigation*. New York, NY, USA: John Wiley & Sons, Inc., 2001.

Dissertations at the Faculty of Medicine, NTNU

1977

1. Knut Joachim Berg: EFFECT OF ACETYLSALICYLIC ACID ON RENAL FUNCTION
2. Karl Erik Viken and Arne Ødegaard: STUDIES ON HUMAN MONOCYTES CULTURED *IN VITRO*

1978

3. Karel Bjørn Cyvin: CONGENITAL DISLOCATION OF THE HIP JOINT.
4. Alf O. Brubakk: METHODS FOR STUDYING FLOW DYNAMICS IN THE LEFT VENTRICLE AND THE AORTA IN MAN.

1979

5. Geirmund Unsgaard: CYTOSTATIC AND IMMUNOREGULATORY ABILITIES OF HUMAN BLOOD MONOCYTES CULTURED IN VITRO

1980

6. Størker Jørstad: URAEMIC TOXINS
7. Arne Olav Jenssen: SOME RHEOLOGICAL, CHEMICAL AND STRUCTURAL PROPERTIES OF MUCOID SPUTUM FROM PATIENTS WITH CHRONIC OBSTRUCTIVE BRONCHITIS

1981

8. Jens Hammerstrøm: CYTOSTATIC AND CYTOLYTIC ACTIVITY OF HUMAN MONOCYTES AND EFFUSION MACROPHAGES AGAINST TUMOR CELLS *IN VITRO*

1983

9. Tore Syversen: EFFECTS OF METHYLMERCURY ON RAT BRAIN PROTEIN.
10. Torbjørn Iversen: SQUAMOUS CELL CARCINOMA OF THE VULVA.

1984

11. Tor-Erik Widerøe: ASPECTS OF CONTINUOUS AMBULATORY PERITONEAL DIALYSIS.
12. Anton Hole: ALTERATIONS OF MONOCYTE AND LYMPHOCYTE FUNCTIONS IN REALTION TO SURGERY UNDER EPIDURAL OR GENERAL ANAESTHESIA.
13. Terje Terjesen: FRACTURE HEALING AND STRESS-PROTECTION AFTER METAL PLATE FIXATION AND EXTERNAL FIXATION.
14. Carsten Saunte: CLUSTER HEADACHE SYNDROME.
15. Inggard Lereim: TRAFFIC ACCIDENTS AND THEIR CONSEQUENCES.
16. Bjørn Magne Eggen: STUDIES IN CYTOTOXICITY IN HUMAN ADHERENT MONONUCLEAR BLOOD CELLS.
17. Trond Haug: FACTORS REGULATING BEHAVIORAL EFFECTS OG DRUGS.

1985

18. Sven Erik Gisvold: RESUSCITATION AFTER COMPLETE GLOBAL BRAIN ISCHEMIA.
19. Terje Espevik: THE CYTOSKELETON OF HUMAN MONOCYTES.
20. Lars Bevanger: STUDIES OF THE Ibc (c) PROTEIN ANTIGENS OF GROUP B STREPTOCOCCI.
21. Ole-Jan Iversen: RETROVIRUS-LIKE PARTICLES IN THE PATHOGENESIS OF PSORIASIS.
22. Lasse Eriksen: EVALUATION AND TREATMENT OF ALCOHOL DEPENDENT BEHAVIOUR.
23. Per I. Lundmo: ANDROGEN METABOLISM IN THE PROSTATE.

1986

24. Dagfinn Berntzen: ANALYSIS AND MANAGEMENT OF EXPERIMENTAL AND CLINICAL PAIN.
25. Odd Arnold Kildahl-Andersen: PRODUCTION AND CHARACTERIZATION OF MONOCYTE-DERIVED CYTOTOXIN AND ITS ROLE IN MONOCYTE-MEDIATED CYTOTOXICITY.
26. Ola Dale: VOLATILE ANAESTHETICS.

1987

27. Per Martin Kleveland: STUDIES ON GASTRIN.
28. Audun N. Øksendal: THE CALCIUM PARADOX AND THE HEART.
29. Vilhjalmur R. Finsen: HIP FRACTURES

1988

30. Rigmor Austgulen: TUMOR NECROSIS FACTOR: A MONOCYTE-DERIVED REGULATOR OF CELLULAR GROWTH.

31. Tom-Harald Edna: HEAD INJURIES ADMITTED TO HOSPITAL.
32. Joseph D. Borsi: NEW ASPECTS OF THE CLINICAL PHARMACOKINETICS OF METHOTREXATE.
33. Olav F. M. Sellevold: GLUCOCORTICOIDS IN MYOCARDIAL PROTECTION.
34. Terje Skjærpe: NONINVASIVE QUANTITATION OF GLOBAL PARAMETERS ON LEFT VENTRICULAR FUNCTION: THE SYSTOLIC PULMONARY ARTERY PRESSURE AND CARDIAC OUTPUT.
35. Eyvind Rødahl: STUDIES OF IMMUNE COMPLEXES AND RETROVIRUS-LIKE ANTIGENS IN PATIENTS WITH ANKYLOSING SPONDYLITIS.
36. Ketil Thorstensen: STUDIES ON THE MECHANISMS OF CELLULAR UPTAKE OF IRON FROM TRANSFERRIN.
37. Anna Midelfart: STUDIES OF THE MECHANISMS OF ION AND FLUID TRANSPORT IN THE BOVINE CORNEA.
38. Eirik Helseth: GROWTH AND PLASMINOGEN ACTIVATOR ACTIVITY OF HUMAN GLIOMAS AND BRAIN METASTASES - WITH SPECIAL REFERENCE TO TRANSFORMING GROWTH FACTOR BETA AND THE EPIDERMAL GROWTH FACTOR RECEPTOR.
39. Petter C. Borchgrevink: MAGNESIUM AND THE ISCHEMIC HEART.
40. Kjell-Arne Rein: THE EFFECT OF EXTRACORPOREAL CIRCULATION ON SUBCUTANEOUS TRANSCAPILLARY FLUID BALANCE.
41. Arne Kristian Sandvik: RAT GASTRIC HISTAMINE.
42. Carl Bredo Dahl: ANIMAL MODELS IN PSYCHIATRY.

1989

43. Torbjørn A. Fredriksen: CERVICOGENIC HEADACHE.
44. Rolf A. Walstad: CEFTAZIDIME.
45. Rolf Salvesen: THE PUPIL IN CLUSTER HEADACHE.
46. Nils Petter Jørgensen: DRUG EXPOSURE IN EARLY PREGNANCY.
47. Johan C. Ræder: PREMEDICATION AND GENERAL ANAESTHESIA IN OUTPATIENT GYNECOLOGICAL SURGERY.
48. M. R. Shalaby: IMMUNOREGULATORY PROPERTIES OF TNF-α AND THE RELATED CYTOKINES.
49. Anders Waage: THE COMPLEX PATTERN OF CYTOKINES IN SEPTIC SHOCK.
50. Bjarne Christian Eriksen: ELECTROSTIMULATION OF THE PELVIC FLOOR IN FEMALE URINARY INCONTINENCE.
51. Tore B. Halvorsen: PROGNOSTIC FACTORS IN COLORECTAL CANCER.

1990

52. Asbjørn Nordby: CELLULAR TOXICITY OF ROENTGEN CONTRAST MEDIA.
53. Kåre E. Tvedt: X-RAY MICROANALYSIS OF BIOLOGICAL MATERIAL.
54. Tore C. Stiles: COGNITIVE VULNERABILITY FACTORS IN THE DEVELOPMENT AND MAINTENANCE OF DEPRESSION.
55. Eva Hofsli: TUMOR NECROSIS FACTOR AND MULTIDRUG RESISTANCE.
56. Helge S. Haarstad: TROPHIC EFFECTS OF CHOLECYSTOKININ AND SECRETIN ON THE RAT PANCREAS.
57. Lars Engebretsen: TREATMENT OF ACUTE ANTERIOR CRUCIATE LIGAMENT INJURIES.
58. Tarjei Rygnestad: DELIBERATE SELF-POISONING IN TRONDHEIM.
59. Arne Z. Henriksen: STUDIES ON CONSERVED ANTIGENIC DOMAINS ON MAJOR OUTER MEMBRANE PROTEINS FROM ENTEROBACTERIA.
60. Steinar Westin: UNEMPLOYMENT AND HEALTH: Medical and social consequences of a factory closure in a ten-year controlled follow-up study.
61. Ylva Sahlin: INJURY REGISTRATION, a tool for accident preventive work.
62. Helge Bjørnstad Pettersen: BIOSYNTHESIS OF COMPLEMENT BY HUMAN ALVEOLAR MACROPHAGES WITH SPECIAL REFERENCE TO SARCOIDOSIS.
63. Berit Schei: TRAPPED IN PAINFUL LOVE.
64. Lars J. Vatten: PROSPECTIVE STUDIES OF THE RISK OF BREAST CANCER IN A COHORT OF NORWEGIAN WOMAN.

1991

65. Kåre Bergh: APPLICATIONS OF ANTI-C5a SPECIFIC MONOCLONAL ANTIBODIES FOR THE ASSESSMENT OF COMPLEMENT ACTIVATION.

66. Svein Svenningsen: THE CLINICAL SIGNIFICANCE OF INCREASED FEMORAL ANTEVERSION.
67. Olbjørn Klepp: NONSEMINOMATOUS GERM CELL TESTIS CANCER: THERAPEUTIC OUTCOME AND PROGNOSTIC FACTORS.
68. Trond Sand: THE EFFECTS OF CLICK POLARITY ON BRAINSTEM AUDITORY EVOKED POTENTIALS AMPLITUDE, DISPERSION, AND LATENCY VARIABLES.
69. Kjetil B. Åsbakk: STUDIES OF A PROTEIN FROM PSORIATIC SCALE, PSO P27, WITH RESPECT TO ITS POTENTIAL ROLE IN IMMUNE REACTIONS IN PSORIASIS.
70. Arnulf Hestnes: STUDIES ON DOWN´S SYNDROME.
71. Randi Nygaard: LONG-TERM SURVIVAL IN CHILDHOOD LEUKEMIA.
72. Bjørn Hagen: THIO-TEPA.
73. Svein Anda: EVALUATION OF THE HIP JOINT BY COMPUTED TOMOGRAMPHY AND ULTRASONOGRAPHY.

1992

74. Martin Svartberg: AN INVESTIGATION OF PROCESS AND OUTCOME OF SHORT-TERM PSYCHODYNAMIC PSYCHOTHERAPY.
75. Stig Arild Slørdahl: AORTIC REGURGITATION.
76. Harold C Sexton: STUDIES RELATING TO THE TREATMENT OF SYMPTOMATIC NON-PSYCHOTIC PATIENTS.
77. Maurice B. Vincent: VASOACTIVE PEPTIDES IN THE OCULAR/FOREHEAD AREA.
78. Terje Johannessen: CONTROLLED TRIALS IN SINGLE SUBJECTS.
79. Turid Nilsen: PYROPHOSPHATE IN HEPATOCYTE IRON METABOLISM.
80. Olav Haraldseth: NMR SPECTROSCOPY OF CEREBRAL ISCHEMIA AND REPERFUSION IN RAT.
81. Eiliv Brenna: REGULATION OF FUNCTION AND GROWTH OF THE OXYNTIC MUCOSA.

1993

82. Gunnar Bovim: CERVICOGENIC HEADACHE.
83. Jarl Arne Kahn: ASSISTED PROCREATION.
84. Bjørn Naume: IMMUNOREGULATORY EFFECTS OF CYTOKINES ON NK CELLS.
85. Rune Wiseth: AORTIC VALVE REPLACEMENT.
86. Jie Ming Shen: BLOOD FLOW VELOCITY AND RESPIRATORY STUDIES.
87. Piotr Kruszewski: SUNCT SYNDROME WITH SPECIAL REFERENCE TO THE AUTONOMIC NERVOUS SYSTEM.
88. Mette Haase Moen: ENDOMETRIOSIS.
89. Anne Vik: VASCULAR GAS EMBOLISM DURING AIR INFUSION AND AFTER DECOMPRESSION IN PIGS.
90. Lars Jacob Stovner: THE CHIARI TYPE I MALFORMATION.
91. Kjell Å. Salvesen: ROUTINE ULTRASONOGRAPHY IN UTERO AND DEVELOPMENT IN CHILDHOOD.

1994

92. Nina-Beate Liabakk: DEVELOPMENT OF IMMUNOASSAYS FOR TNF AND ITS SOLUBLE RECEPTORS.
93. Sverre Helge Torp: *erb*B ONCOGENES IN HUMAN GLIOMAS AND MENINGIOMAS.
94. Olav M. Linaker: MENTAL RETARDATION AND PSYCHIATRY. Past and present.
95. Per Oscar Feet: INCREASED ANTIDEPRESSANT AND ANTIPANIC EFFECT IN COMBINED TREATMENT WITH DIXYRAZINE AND TRICYCLIC ANTIDEPRESSANTS.
96. Stein Olav Samstad: CROSS SECTIONAL FLOW VELOCITY PROFILES FROM TWO-DIMENSIONAL DOPPLER ULTRASOUND: Studies on early mitral blood flow.
97. Bjørn Backe: STUDIES IN ANTENATAL CARE.
98. Gerd Inger Ringdal: QUALITY OF LIFE IN CANCER PATIENTS.
99. Torvid Kiserud: THE DUCTUS VENOSUS IN THE HUMAN FETUS.
100. Hans E. Fjøsne: HORMONAL REGULATION OF PROSTATIC METABOLISM.
101. Eylert Brodtkorb: CLINICAL ASPECTS OF EPILEPSY IN THE MENTALLY RETARDED.
102. Roar Juul: PEPTIDERGIC MECHANISMS IN HUMAN SUBARACHNOID HEMORRHAGE.
103. Unni Syversen: CHROMOGRANIN A. Phsysiological and Clinical Role.

1995

104. Odd Gunnar Brakstad: THERMOSTABLE NUCLEASE AND THE *nuc* GENE IN THE DIAGNOSIS OF *Staphylococcus aureus* INFECTIONS.

105. Terje Engan: NUCLEAR MAGNETIC RESONANCE (NMR) SPECTROSCOPY OF PLASMA IN MALIGNANT DISEASE.
106. Kirsten Rasmussen: VIOLENCE IN THE MENTALLY DISORDERED.
107. Finn Egil Skjeldestad: INDUCED ABORTION: Timetrends and Determinants.
108. Roar Stenseth: THORACIC EPIDURAL ANALGESIA IN AORTOCORONARY BYPASS SURGERY.
109. Arild Faxvaag: STUDIES OF IMMUNE CELL FUNCTION *in mice infected with* MURINE RETROVIRUS.

1996

110. Svend Aakhus: NONINVASIVE COMPUTERIZED ASSESSMENT OF LEFT VENTRICULAR FUNCTION AND SYSTEMIC ARTERIAL PROPERTIES. Methodology and some clinical applications.
111. Klaus-Dieter Bolz: INTRAVASCULAR ULTRASONOGRAPHY.
112. Petter Aadahl: CARDIOVASCULAR EFFECTS OF THORACIC AORTIC CROSS-CLAMPING.
113. Sigurd Steinshamn: CYTOKINE MEDIATORS DURING GRANULOCYTOPENIC INFECTIONS.
114. Hans Stifoss-Hanssen: SEEKING MEANING OR HAPPINESS?
115. Anne Kvikstad: LIFE CHANGE EVENTS AND MARITAL STATUS IN RELATION TO RISK AND PROGNOSIS OF CANCER.
116. Torbjørn Grøntvedt: TREATMENT OF ACUTE AND CHRONIC ANTERIOR CRUCIATE LIGAMENT INJURIES. A clinical and biomechanical study.
117. Sigrid Hørven Wigers: CLINICAL STUDIES OF FIBROMYALGIA WITH FOCUS ON ETIOLOGY, TREATMENT AND OUTCOME.
118. Jan Schjøtt: MYOCARDIAL PROTECTION: Functional and Metabolic Characteristics of Two Endogenous Protective Principles.
119. Marit Martinussen: STUDIES OF INTESTINAL BLOOD FLOW AND ITS RELATION TO TRANSITIONAL CIRCULATORY ADAPATION IN NEWBORN INFANTS.
120. Tomm B. Müller: MAGNETIC RESONANCE IMAGING IN FOCAL CEREBRAL ISCHEMIA.
121. Rune Haaverstad: OEDEMA FORMATION OF THE LOWER EXTREMITIES.
122. Magne Børset: THE ROLE OF CYTOKINES IN MULTIPLE MYELOMA, WITH SPECIAL REFERENCE TO HEPATOCYTE GROWTH FACTOR.
123. Geir Smedslund: A THEORETICAL AND EMPIRICAL INVESTIGATION OF SMOKING, STRESS AND DISEASE: RESULTS FROM A POPULATION SURVEY.

1997

124. Torstein Vik: GROWTH, MORBIDITY, AND PSYCHOMOTOR DEVELOPMENT IN INFANTS WHO WERE GROWTH RETARDED *IN UTERO*.
125. Siri Forsmo: ASPECTS AND CONSEQUENCES OF OPPORTUNISTIC SCREENING FOR CERVICAL CANCER. Results based on data from three Norwegian counties.
126. Jon S. Skranes: CEREBRAL MRI AND NEURODEVELOPMENTAL OUTCOME IN VERY LOW BIRTH WEIGHT (VLBW) CHILDREN. A follow-up study of a geographically based year cohort of VLBW children at ages one and six years.
127. Knut Bjørnstad: COMPUTERIZED ECHOCARDIOGRAPHY FOR EVALUTION OF CORONARY ARTERY DISEASE.
128. Grethe Elisabeth Borchgrevink: DIAGNOSIS AND TREATMENT OF WHIPLASH/NECK SPRAIN INJURIES CAUSED BY CAR ACCIDENTS.
129. Tor Elsås: NEUROPEPTIDES AND NITRIC OXIDE SYNTHASE IN OCULAR AUTONOMIC AND SENSORY NERVES.
130. Rolf W. Gråwe: EPIDEMIOLOGICAL AND NEUROPSYCHOLOGICAL PERSPECTIVES ON SCHIZOPHRENIA.
131. Tonje Strømholm: CEREBRAL HAEMODYNAMICS DURING THORACIC AORTIC CROSSCLAMPING. An experimental study in pigs.

1998

132. Martinus Bråten: STUDIES ON SOME PROBLEMS REALTED TO INTRAMEDULLARY NAILING OF FEMORAL FRACTURES.
133. Ståle Nordgård: PROLIFERATIVE ACTIVITY AND DNA CONTENT AS PROGNOSTIC INDICATORS IN ADENOID CYSTIC CARCINOMA OF THE HEAD AND NECK.

134. Egil Lien: SOLUBLE RECEPTORS FOR **TNF** AND **LPS**: RELEASE PATTERN AND POSSIBLE SIGNIFICANCE IN DISEASE.
135. Marit Bjørgaas: HYPOGLYCAEMIA IN CHILDREN WITH DIABETES MELLITUS
136. Frank Skorpen: GENETIC AND FUNCTIONAL ANALYSES OF DNA REPAIR IN HUMAN CELLS.
137. Juan A. Pareja: SUNCT SYNDROME. ON THE CLINICAL PICTURE. ITS DISTINCTION FROM OTHER, SIMILAR HEADACHES.
138. Anders Angelsen: NEUROENDOCRINE CELLS IN HUMAN PROSTATIC CARCINOMAS AND THE PROSTATIC COMPLEX OF RAT, GUINEA PIG, CAT AND DOG.
139. Fabio Antonaci: CHRONIC PAROXYSMAL HEMICRANIA AND HEMICRANIA CONTINUA: TWO DIFFERENT ENTITIES?
140. Sven M. Carlsen: ENDOCRINE AND METABOLIC EFFECTS OF METFORMIN WITH SPECIAL EMPHASIS ON CARDIOVASCULAR RISK FACTORES.

1999

141. Terje A. Murberg: DEPRESSIVE SYMPTOMS AND COPING AMONG PATIENTS WITH CONGESTIVE HEART FAILURE.
142. Harm-Gerd Karl Blaas: THE EMBRYONIC EXAMINATION. Ultrasound studies on the development of the human embryo.
143. Noèmi Becser Andersen:THE CEPHALIC SENSORY NERVES IN UNILATERAL HEADACHES. Anatomical background and neurophysiological evaluation.
144. Eli-Janne Fiskerstrand: LASER TREATMENT OF PORT WINE STAINS. A study of the efficacy and limitations of the pulsed dye laser. Clinical and morfological analyses aimed at improving the therapeutic outcome.
145. Bård Kulseng: A STUDY OF ALGINATE CAPSULE PROPERTIES AND CYTOKINES IN RELATION TO INSULIN DEPENDENT DIABETES MELLITUS.
146. Terje Haug: STRUCTURE AND REGULATION OF THE HUMAN UNG GENE ENCODING URACIL-DNA GLYCOSYLASE.
147. Heidi Brurok: MANGANESE AND THE HEART. A Magic Metal with Diagnostic and Therapeutic Possibilites.
148. Agnes Kathrine Lie: DIAGNOSIS AND PREVALENCE OF HUMAN PAPILLOMAVIRUS INFECTION IN CERVICAL INTRAEPITELIAL NEOPLASIA. Relationship to Cell Cycle Regulatory Proteins and HLA DQBI Genes.
149. Ronald Mårvik: PHARMACOLOGICAL, PHYSIOLOGICAL AND PATHOPHYSIOLOGICAL STUDIES ON ISOLATED STOMACS.
150. Ketil Jarl Holen: THE ROLE OF ULTRASONOGRAPHY IN THE DIAGNOSIS AND TREATMENT OF HIP DYSPLASIA IN NEWBORNS.
151. Irene Hetlevik: THE ROLE OF CLINICAL GUIDELINES IN CARDIOVASCULAR RISK INTERVENTION IN GENERAL PRACTICE.
152. Katarina Tunòn: ULTRASOUND AND PREDICTION OF GESTATIONAL AGE.
153. Johannes Soma: INTERACTION BETWEEN THE LEFT VENTRICLE AND THE SYSTEMIC ARTERIES.
154. Arild Aamodt: DEVELOPMENT AND PRE-CLINICAL EVALUATION OF A CUSTOM-MADE FEMORAL STEM.
155. Agnar Tegnander: DIAGNOSIS AND FOLLOW-UP OF CHILDREN WITH SUSPECTED OR KNOWN HIP DYSPLASIA.
156. Bent Indredavik: STROKE UNIT TREATMENT: SHORT AND LONG-TERM EFFECTS
157. Jolanta Vanagaite Vingen: PHOTOPHOBIA AND PHONOPHOBIA IN PRIMARY HEADACHES

2000

158. Ola Dalsegg Sæther: PATHOPHYSIOLOGY DURING PROXIMAL AORTIC CROSS-CLAMPING CLINICAL AND EXPERIMENTAL STUDIES
159. xxxxxxxxx (blind number)
160. Christina Vogt Isaksen: PRENATAL ULTRASOUND AND POSTMORTEM FINDINGS – A TEN YEAR CORRELATIVE STUDY OF FETUSES AND INFANTS WITH DEVELOPMENTAL ANOMALIES.
161. Holger Seidel: HIGH-DOSE METHOTREXATE THERAPY IN CHILDREN WITH ACUTE LYMPHOCYTIC LEUKEMIA: DOSE, CONCENTRATION, AND EFFECT CONSIDERATIONS.
162. Stein Hallan: IMPLEMENTATION OF MODERN MEDICAL DECISION ANALYSIS INTO CLINICAL DIAGNOSIS AND TREATMENT.

163. Malcolm Sue-Chu: INVASIVE AND NON-INVASIVE STUDIES IN CROSS-COUNTRY SKIERS WITH ASTHMA-LIKE SYMPTOMS.
164. Ole-Lars Brekke: EFFECTS OF ANTIOXIDANTS AND FATTY ACIDS ON TUMOR NECROSIS FACTOR-INDUCED CYTOTOXICITY.
165. Jan Lundbom: AORTOCORONARY BYPASS SURGERY: CLINICAL ASPECTS, COST CONSIDERATIONS AND WORKING ABILITY.
166. John-Anker Zwart: LUMBAR NERVE ROOT COMPRESSION, BIOCHEMICAL AND NEUROPHYSIOLOGICAL ASPECTS.
167. Geir Falck: HYPEROSMOLALITY AND THE HEART.
168. Eirik Skogvoll: CARDIAC ARREST Incidence, Intervention and Outcome.
169. Dalius Bansevicius: SHOULDER-NECK REGION IN CERTAIN HEADACHES AND CHRONIC PAIN SYNDROMES.
170. Bettina Kinge: REFRACTIVE ERRORS AND BIOMETRIC CHANGES AMONG UNIVERSITY STUDENTS IN NORWAY.
171. Gunnar Qvigstad: CONSEQUENCES OF HYPERGASTRINEMIA IN MAN
172. Hanne Ellekjær: EPIDEMIOLOGICAL STUDIES OF STROKE IN A NORWEGIAN POPULATION. INCIDENCE, RISK FACTORS AND PROGNOSIS
173. Hilde Grimstad: VIOLENCE AGAINST WOMEN AND PREGNANCY OUTCOME.
174. Astrid Hjelde: SURFACE TENSION AND COMPLEMENT ACTIVATION: Factors influencing bubble formation and bubble effects after decompression.
175. Kjell A. Kvistad: MR IN BREAST CANCER – A CLINICAL STUDY.
176. Ivar Rossvoll: ELECTIVE ORTHOPAEDIC SURGERY IN A DEFINED POPULATION. Studies on demand, waiting time for treatment and incapacity for work.
177. Carina Seidel: PROGNOSTIC VALUE AND BIOLOGICAL EFFECTS OF HEPATOCYTE GROWTH FACTOR AND SYNDECAN-1 IN MULTIPLE MYELOMA.

2001

178. Alexander Wahba: THE INFLUENCE OF CARDIOPULMONARY BYPASS ON PLATELET FUNCTION AND BLOOD COAGULATION – DETERMINANTS AND CLINICAL CONSEQUENSES
179. Marcus Schmitt-Egenolf: THE RELEVANCE OF THE MAJOR hISTOCOMPATIBILITY COMPLEX FOR THE GENETICS OF PSORIASIS
180. Odrun Arna Gederaas: BIOLOGICAL MECHANISMS INVOLVED IN 5-AMINOLEVULINIC ACID BASED PHOTODYNAMIC THERAPY
181. Pål Richard Romundstad: CANCER INCIDENCE AMONG NORWEGIAN ALUMINIUM WORKERS
182. Henrik Hjorth-Hansen: NOVEL CYTOKINES IN GROWTH CONTROL AND BONE DISEASE OF MULTIPLE MYELOMA
183. Gunnar Morken: SEASONAL VARIATION OF HUMAN MOOD AND BEHAVIOUR
184. Bjørn Olav Haugen: MEASUREMENT OF CARDIAC OUTPUT AND STUDIES OF VELOCITY PROFILES IN AORTIC AND MITRAL FLOW USING TWO- AND THREE-DIMENSIONAL COLOUR FLOW IMAGING
185. Geir Bråthen: THE CLASSIFICATION AND CLINICAL DIAGNOSIS OF ALCOHOL-RELATED SEIZURES
186. Knut Ivar Aasarød: RENAL INVOLVEMENT IN INFLAMMATORY RHEUMATIC DISEASE. A Study of Renal Disease in Wegener's Granulomatosis and in Primary Sjögren's Syndrome
187. Trude Helen Flo: RESEPTORS INVOLVED IN CELL ACTIVATION BY DEFINED URONIC ACID POLYMERS AND BACTERIAL COMPONENTS
188. Bodil Kavli: HUMAN URACIL-DNA GLYCOSYLASES FROM THE UNG GENE: STRUCTRUAL BASIS FOR SUBSTRATE SPECIFICITY AND REPAIR
189. Liv Thommesen: MOLECULAR MECHANISMS INVOLVED IN TNF- AND GASTRIN-MEDIATED GENE REGULATION
190. Turid Lingaas Holmen: SMOKING AND HEALTH IN ADOLESCENCE; THE NORD-TRØNDELAG HEALTH STUDY, 1995-97
191. Øyvind Hjertner: MULTIPLE MYELOMA: INTERACTIONS BETWEEN MALIGNANT PLASMA CELLS AND THE BONE MICROENVIRONMENT
192. Asbjørn Støylen: STRAIN RATE IMAGING OF THE LEFT VENTRICLE BY ULTRASOUND. FEASIBILITY, CLINICAL VALIDATION AND PHYSIOLOGICAL ASPECTS

193. Kristian Midthjell: DIABETES IN ADULTS IN NORD-TRØNDELAG. PUBLIC HEALTH ASPECTS OF DIABETES MELLITUS IN A LARGE, NON-SELECTED NORWEGIAN POPULATION.
194. Guanglin Cui: FUNCTIONAL ASPECTS OF THE ECL CELL IN RODENTS
195. Ulrik Wisløff: CARDIAC EFFECTS OF AEROBIC ENDURANCE TRAINING: HYPERTROPHY, CONTRACTILITY AND CALCUIM HANDLING IN NORMAL AND FAILING HEART
196. Øyvind Halaas: MECHANISMS OF IMMUNOMODULATION AND CELL-MEDIATED CYTOTOXICITY INDUCED BY BACTERIAL PRODUCTS
197. Tore Amundsen: PERFUSION MR IMAGING IN THE DIAGNOSIS OF PULMONARY EMBOLISM
198. Nanna Kurtze: THE SIGNIFICANCE OF ANXIETY AND DEPRESSION IN FATIQUE AND PATTERNS OF PAIN AMONG INDIVIDUALS DIAGNOSED WITH FIBROMYALGIA: RELATIONS WITH QUALITY OF LIFE, FUNCTIONAL DISABILITY, LIFESTYLE, EMPLOYMENT STATUS, CO-MORBIDITY AND GENDER
199. Tom Ivar Lund Nilsen: PROSPECTIVE STUDIES OF CANCER RISK IN NORD-TRØNDELAG: THE HUNT STUDY. Associations with anthropometric, socioeconomic, and lifestyle risk factors
200. Asta Kristine Håberg: A NEW APPROACH TO THE STUDY OF MIDDLE CEREBRAL ARTERY OCCLUSION IN THE RAT USING MAGNETIC RESONANCE TECHNIQUES

2002

201. Knut Jørgen Arntzen: PREGNANCY AND CYTOKINES
202. Henrik Døllner: INFLAMMATORY MEDIATORS IN PERINATAL INFECTIONS
203. Asta Bye: LOW FAT, LOW LACTOSE DIET USED AS PROPHYLACTIC TREATMENT OF ACUTE INTESTINAL REACTIONS DURING PELVIC RADIOTHERAPY. A PROSPECTIVE RANDOMISED STUDY.
204. Sylvester Moyo: STUDIES ON STREPTOCOCCUS AGALACTIAE (GROUP B STREPTOCOCCUS) SURFACE-ANCHORED MARKERS WITH EMPHASIS ON STRAINS AND HUMAN SERA FROM ZIMBABWE.
205. Knut Hagen: HEAD-HUNT: THE EPIDEMIOLOGY OF HEADACHE IN NORD-TRØNDELAG
206. Li Lixin: ON THE REGULATION AND ROLE OF UNCOUPLING PROTEIN-2 IN INSULIN PRODUCING ß-CELLS
207. Anne Hildur Henriksen: SYMPTOMS OF ALLERGY AND ASTHMA VERSUS MARKERS OF LOWER AIRWAY INFLAMMATION AMONG ADOLESCENTS
208. Egil Andreas Fors: NON-MALIGNANT PAIN IN RELATION TO PSYCHOLOGICAL AND ENVIRONTENTAL FACTORS. EXPERIENTAL AND CLINICAL STUDES OF PAIN WITH FOCUS ON FIBROMYALGIA
209. Pål Klepstad: MORPHINE FOR CANCER PAIN
210. Ingunn Bakke: MECHANISMS AND CONSEQUENCES OF PEROXISOME PROLIFERATOR-INDUCED HYPERFUNCTION OF THE RAT GASTRIN PRODUCING CELL
211. Ingrid Susann Gribbestad: MAGNETIC RESONANCE IMAGING AND SPECTROSCOPY OF BREAST CANCER
212. Rønnaug Astri Ødegård: PREECLAMPSIA – MATERNAL RISK FACTORS AND FETAL GROWTH
213. Johan Haux: STUDIES ON CYTOTOXICITY INDUCED BY HUMAN NATURAL KILLER CELLS AND DIGITOXIN
214. Turid Suzanne Berg-Nielsen: PARENTING PRACTICES AND MENTALLY DISORDERED ADOLESCENTS
215. Astrid Rydning: BLOOD FLOW AS A PROTECTIVE FACTOR FOR THE STOMACH MUCOSA. AN EXPERIMENTAL STUDY ON THE ROLE OF MAST CELLS AND SENSORY AFFERENT NEURONS

2003

216. Jan Pål Loennechen: HEART FAILURE AFTER MYOCARDIAL INFARCTION. Regional Differences, Myocyte Function, Gene Expression, and Response to Cariporide, Losartan, and Exercise Training.

217. Elisabeth Qvigstad: EFFECTS OF FATTY ACIDS AND OVER-STIMULATION ON INSULIN SECRETION IN MAN
218. Arne Åsberg: EPIDEMIOLOGICAL STUDIES IN HEREDITARY HEMOCHROMATOSIS: PREVALENCE, MORBIDITY AND BENEFIT OF SCREENING.
219. Johan Fredrik Skomsvoll: REPRODUCTIVE OUTCOME IN WOMEN WITH RHEUMATIC DISEASE. A population registry based study of the effects of inflammatory rheumatic disease and connective tissue disease on reproductive outcome in Norwegian women in 1967-1995.
220. Siv Mørkved: URINARY INCONTINENCE DURING PREGNANCY AND AFTER DELIVERY: EFFECT OF PELVIC FLOOR MUSCLE TRAINING IN PREVENTION AND TREATMENT
221. Marit S. Jordhøy: THE IMPACT OF COMPREHENSIVE PALLIATIVE CARE
222. Tom Christian Martinsen: HYPERGASTRINEMIA AND HYPOACIDITY IN RODENTS – CAUSES AND CONSEQUENCES
223. Solveig Tingulstad: CENTRALIZATION OF PRIMARY SURGERY FOR OVARAIN CANCER. FEASIBILITY AND IMPACT ON SURVIVAL
224. Haytham Eloqayli: METABOLIC CHANGES IN THE BRAIN CAUSED BY EPILEPTIC SEIZURES
225. Torunn Bruland: STUDIES OF EARLY RETROVIRUS-HOST INTERACTIONS – VIRAL DETERMINANTS FOR PATHOGENESIS AND THE INFLUENCE OF SEX ON THE SUSCEPTIBILITY TO FRIEND MURINE LEUKAEMIA VIRUS INFECTION
226. Torstein Hole: DOPPLER ECHOCARDIOGRAPHIC EVALUATION OF LEFT VENTRICULAR FUNCTION IN PATIENTS WITH ACUTE MYOCARDIAL INFARCTION
227. Vibeke Nossum: THE EFFECT OF VASCULAR BUBBLES ON ENDOTHELIAL FUNCTION
228. Sigurd Fasting: ROUTINE BASED RECORDING OF ADVERSE EVENTS DURING ANAESTHESIA – APPLICATION IN QUALITY IMPROVEMENT AND SAFETY
229. Solfrid Romundstad: EPIDEMIOLOGICAL STUDIES OF MICROALBUMINURIA. THE NORD-TRØNDELAG HEALTH STUDY 1995-97 (HUNT 2)
230. Geir Torheim: PROCESSING OF DYNAMIC DATA SETS IN MAGNETIC RESONANCE IMAGING
231. Catrine Ahlén: SKIN INFECTIONS IN OCCUPATIONAL SATURATION DIVERS IN THE NORTH SEA AND THE IMPACT OF THE ENVIRONMENT
232. Arnulf Langhammer: RESPIRATORY SYMPTOMS, LUNG FUNCTION AND BONE MINERAL DENSITY IN A COMPREHENSIVE POPULATION SURVEY. THE NORD-TRØNDELAG HEALTH STUDY 1995-97. THE BRONCHIAL OBSTRUCTION IN NORD-TRØNDELAG STUDY
233. Einar Kjelsås: EATING DISORDERS AND PHYSICAL ACTIVITY IN NON-CLINICAL SAMPLES
234. Arne Wibe: RECTAL CANCER TREATMENT IN NORWAY – STANDARDISATION OF SURGERY AND QUALITY ASSURANCE

2004

235. Eivind Witsø: BONE GRAFT AS AN ANTIBIOTIC CARRIER
236. Anne Mari Sund: DEVELOPMENT OF DEPRESSIVE SYMPTOMS IN EARLY ADOLESCENCE
237. Hallvard Lærum: EVALUATION OF ELECTRONIC MEDICAL RECORDS – A CLINICAL TASK PERSPECTIVE
238. Gustav Mikkelsen: ACCESSIBILITY OF INFORMATION IN ELECTRONIC PATIENT RECORDS; AN EVALUATION OF THE ROLE OF DATA QUALITY
239. Steinar Krokstad: SOCIOECONOMIC INEQUALITIES IN HEALTH AND DISABILITY. SOCIAL EPIDEMIOLOGY IN THE NORD-TRØNDELAG HEALTH STUDY (HUNT), NORWAY
240. Arne Kristian Myhre: NORMAL VARIATION IN ANOGENITAL ANATOMY AND MICROBIOLOGY IN NON-ABUSED PRESCHOOL CHILDREN
241. Ingunn Dybedal: NEGATIVE REGULATORS OF HEMATOPOIETEC STEM AND PROGENITOR CELLS
242. Beate Sitter: TISSUE CHARACTERIZATION BY HIGH RESOLUTION MAGIC ANGLE SPINNING MR SPECTROSCOPY
243. Per Arne Aas: MACROMOLECULAR MAINTENANCE IN HUMAN CELLS – REPAIR OF URACIL IN DNA AND METHYLATIONS IN DNA AND RNA

244. Anna Bofin: FINE NEEDLE ASPIRATION CYTOLOGY IN THE PRIMARY INVESTIGATION OF BREAST TUMOURS AND IN THE DETERMINATION OF TREATMENT STRATEGIES
245. Jim Aage Nøttestad: DEINSTITUTIONALIZATION AND MENTAL HEALTH CHANGES AMONG PEOPLE WITH MENTAL RETARDATION
246. Reidar Fossmark: GASTRIC CANCER IN JAPANESE COTTON RATS
247. Wibeke Nordhøy: MANGANESE AND THE HEART, INTRACELLULAR MR RELAXATION AND WATER EXCHANGE ACROSS THE CARDIAC CELL MEMBRANE

2005

248. Sturla Molden: QUANTITATIVE ANALYSES OF SINGLE UNITS RECORDED FROM THE HIPPOCAMPUS AND ENTORHINAL CORTEX OF BEHAVING RATS
249. Wenche Brenne Drøyvold: EPIDEMIOLOGICAL STUDIES ON WEIGHT CHANGE AND HEALTH IN A LARGE POPULATION. THE NORD-TRØNDELAG HEALTH STUDY (HUNT)
250. Ragnhild Støen: ENDOTHELIUM-DEPENDENT VASODILATION IN THE FEMORAL ARTERY OF DEVELOPING PIGLETS
251. Aslak Steinsbekk: HOMEOPATHY IN THE PREVENTION OF UPPER RESPIRATORY TRACT INFECTIONS IN CHILDREN
252. Hill-Aina Steffenach: MEMORY IN HIPPOCAMPAL AND CORTICO-HIPPOCAMPAL CIRCUITS
253. Eystein Stordal: ASPECTS OF THE EPIDEMIOLOGY OF DEPRESSIONS BASED ON SELF-RATING IN A LARGE GENERAL HEALTH STUDY (THE HUNT-2 STUDY)
254. Viggo Pettersen: FROM MUSCLES TO SINGING: THE ACTIVITY OF ACCESSORY BREATHING MUSCLES AND THORAX MOVEMENT IN CLASSICAL SINGING
255. Marianne Fyhn: SPATIAL MAPS IN THE HIPPOCAMPUS AND ENTORHINAL CORTEX
256. Robert Valderhaug: OBSESSIVE-COMPULSIVE DISORDER AMONG CHILDREN AND ADOLESCENTS: CHARACTERISTICS AND PSYCHOLOGICAL MANAGEMENT OF PATIENTS IN OUTPATIENT PSYCHIATRIC CLINICS
257. Erik Skaaheim Haug: INFRARENAL ABDOMINAL AORTIC ANEURYSMS – COMORBIDITY AND RESULTS FOLLOWING OPEN SURGERY
258. Daniel Kondziella: GLIAL-NEURONAL INTERACTIONS IN EXPERIMENTAL BRAIN DISORDERS
259. Vegard Heimly Brun: ROUTES TO SPATIAL MEMORY IN HIPPOCAMPAL PLACE CELLS
260. Kenneth McMillan: PHYSIOLOGICAL ASSESSMENT AND TRAINING OF ENDURANCE AND STRENGTH IN PROFESSIONAL YOUTH SOCCER PLAYERS
261. Marit Sæbø Indredavik: MENTAL HEALTH AND CEREBRAL MAGNETIC RESONANCE IMAGING IN ADOLESCENTS WITH LOW BIRTH WEIGHT
262. Ole Johan Kemi: ON THE CELLULAR BASIS OF AEROBIC FITNESS, INTENSITY-DEPENDENCE AND TIME-COURSE OF CARDIOMYOCYTE AND ENDOTHELIAL ADAPTATIONS TO EXERCISE TRAINING
263. Eszter Vanky: POLYCYSTIC OVARY SYNDROME – METFORMIN TREATMENT IN PREGNANCY
264. Hild Fjærtoft: EXTENDED STROKE UNIT SERVICE AND EARLY SUPPORTED DISCHARGE. SHORT AND LONG-TERM EFFECTS
265. Grete Dyb: POSTTRAUMATIC STRESS REACTIONS IN CHILDREN AND ADOLESCENTS
266. Vidar Fykse: SOMATOSTATIN AND THE STOMACH
267. Kirsti Berg: OXIDATIVE STRESS AND THE ISCHEMIC HEART: A STUDY IN PATIENTS UNDERGOING CORONARY REVASCULARIZATION
268. Björn Inge Gustafsson: THE SEROTONIN PRODUCING ENTEROCHROMAFFIN CELL, AND EFFECTS OF HYPERSEROTONINEMIA ON HEART AND BONE

2006

269. Torstein Baade Rø: EFFECTS OF BONE MORPHOGENETIC PROTEINS, HEPATOCYTE GROWTH FACTOR AND INTERLEUKIN-21 IN MULTIPLE MYELOMA
270. May-Britt Tessem: METABOLIC EFFECTS OF ULTRAVIOLET RADIATION ON THE ANTERIOR PART OF THE EYE
271. Anne-Sofie Helvik: COPING AND EVERYDAY LIFE IN A POPULATION OF ADULTS WITH HEARING IMPAIRMENT

272. Therese Standal: MULTIPLE MYELOMA: THE INTERPLAY BETWEEN MALIGNANT PLASMA CELLS AND THE BONE MARROW MICROENVIRONMENT
273. Ingvild Saltvedt: TREATMENT OF ACUTELY SICK, FRAIL ELDERLY PATIENTS IN A GERIATRIC EVALUATION AND MANAGEMENT UNIT – RESULTS FROM A PROSPECTIVE RANDOMISED TRIAL
274. Birger Henning Endreseth: STRATEGIES IN RECTAL CANCER TREATMENT – FOCUS ON EARLY RECTAL CANCER AND THE INFLUENCE OF AGE ON PROGNOSIS
275. Anne Mari Aukan Rokstad: ALGINATE CAPSULES AS BIOREACTORS FOR CELL THERAPY
276. Mansour Akbari: HUMAN BASE EXCISION REPAIR FOR PRESERVATION OF GENOMIC STABILITY
277. Stein Sundstrøm: IMPROVING TREATMENT IN PATIENTS WITH LUNG CANCER – RESULTS FROM TWO MULITCENTRE RANDOMISED STUDIES
278. Hilde Pleym: BLEEDING AFTER CORONARY ARTERY BYPASS SURGERY - STUDIES ON HEMOSTATIC MECHANISMS, PROPHYLACTIC DRUG TREATMENT AND EFFECTS OF AUTOTRANSFUSION
279. Line Merethe Oldervoll: PHYSICAL ACTIVITY AND EXERCISE INTERVENTIONS IN CANCER PATIENTS
280. Boye Welde: THE SIGNIFICANCE OF ENDURANCE TRAINING, RESISTANCE TRAINING AND MOTIVATIONAL STYLES IN ATHLETIC PERFORMANCE AMONG ELITE JUNIOR CROSS-COUNTRY SKIERS
281. Per Olav Vandvik: IRRITABLE BOWEL SYNDROME IN NORWAY, STUDIES OF PREVALENCE, DIAGNOSIS AND CHARACTERISTICS IN GENERAL PRACTICE AND IN THE POPULATION
282. Idar Kirkeby-Garstad: CLINICAL PHYSIOLOGY OF EARLY MOBILIZATION AFTER CARDIAC SURGERY
283. Linn Getz: SUSTAINABLE AND RESPONSIBLE PREVENTIVE MEDICINE. CONCEPTUALISING ETHICAL DILEMMAS ARISING FROM CLINICAL IMPLEMENTATION OF ADVANCING MEDICAL TECHNOLOGY
284. Eva Tegnander: DETECTION OF CONGENITAL HEART DEFECTS IN A NON-SELECTED POPULATION OF 42,381 FETUSES
285. Kristin Gabestad Nørsett: GENE EXPRESSION STUDIES IN GASTROINTESTINAL PATHOPHYSIOLOGY AND NEOPLASIA
286. Per Magnus Haram: GENETIC VS. AQUIRED FITNESS: METABOLIC, VASCULAR AND CARDIOMYOCYTE ADAPTATIONS
287. Agneta Johansson: GENERAL RISK FACTORS FOR GAMBLING PROBLEMS AND THE PREVALENCE OF PATHOLOGICAL GAMBLING IN NORWAY
288. Svein Artur Jensen: THE PREVALENCE OF SYMPTOMATIC ARTERIAL DISEASE OF THE LOWER LIMB
289. Charlotte Björk Ingul: QUANITIFICATION OF REGIONAL MYOCARDIAL FUNCTION BY STRAIN RATE AND STRAIN FOR EVALUATION OF CORONARY ARTERY DISEASE. AUTOMATED VERSUS MANUAL ANALYSIS DURING ACUTE MYOCARDIAL INFARCTION AND DOBUTAMINE STRESS ECHOCARDIOGRAPHY
290. Jakob Nakling: RESULTS AND CONSEQUENCES OF ROUTINE ULTRASOUND SCREENING IN PREGNANCY – A GEOGRAPHIC BASED POPULATION STUDY
291. Anne Engum: DEPRESSION AND ANXIETY – THEIR RELATIONS TO THYROID DYSFUNCTION AND DIABETES IN A LARGE EPIDEMIOLOGICAL STUDY
292. Ottar Bjerkeset: ANXIETY AND DEPRESSION IN THE GENERAL POPULATION: RISK FACTORS, INTERVENTION AND OUTCOME – THE NORD-TRØNDELAG HEALTH STUDY (HUNT)
293. Jon Olav Drogset: RESULTS AFTER SURGICAL TREATMENT OF ANTERIOR CRUCIATE LIGAMENT INJURIES – A CLINICAL STUDY
294. Lars Fosse: MECHANICAL BEHAVIOUR OF COMPACTED MORSELLISED BONE – AN EXPERIMENTAL IN VITRO STUDY
295. Gunilla Klensmeden Fosse: MENTAL HEALTH OF PSYCHIATRIC OUTPATIENTS BULLIED IN CHILDHOOD
296. Paul Jarle Mork: MUSCLE ACTIVITY IN WORK AND LEISURE AND ITS ASSOCIATION TO MUSCULOSKELETAL PAIN

297. Björn Stenström: LESSONS FROM RODENTS: I: MECHANISMS OF OBESITY SURGERY – ROLE OF STOMACH. II: CARCINOGENIC EFFECTS OF *HELICOBACTER PYLORI* AND SNUS IN THE STOMACH

2007

298. Haakon R. Skogseth: INVASIVE PROPERTIES OF CANCER – A TREATMENT TARGET ? IN VITRO STUDIES IN HUMAN PROSTATE CANCER CELL LINES
299. Janniche Hammer: GLUTAMATE METABOLISM AND CYCLING IN MESIAL TEMPORAL LOBE EPILEPSY
300. May Britt Drugli: YOUNG CHILDREN TREATED BECAUSE OF ODD/CD: CONDUCT PROBLEMS AND SOCIAL COMPETENCIES IN DAY-CARE AND SCHOOL SETTINGS
301. Arne Skjold: MAGNETIC RESONANCE KINETICS OF MANGANESE DIPYRIDOXYL DIPHOSPHATE (MnDPDP) IN HUMAN MYOCARDIUM. STUDIES IN HEALTHY VOLUNTEERS AND IN PATIENTS WITH RECENT MYOCARDIAL INFARCTION
302. Siri Malm: LEFT VENTRICULAR SYSTOLIC FUNCTION AND MYOCARDIAL PERFUSION ASSESSED BY CONTRAST ECHOCARDIOGRAPHY
303. Valentina Maria do Rosario Cabral Iversen: MENTAL HEALTH AND PSYCHOLOGICAL ADAPTATION OF CLINICAL AND NON-CLINICAL MIGRANT GROUPS
304. Lasse Løvstakken: SIGNAL PROCESSING IN DIAGNOSTIC ULTRASOUND: ALGORITHMS FOR REAL-TIME ESTIMATION AND VISUALIZATION OF BLOOD FLOW VELOCITY
305. Elisabeth Olstad: GLUTAMATE AND GABA: MAJOR PLAYERS IN NEURONAL METABOLISM
306. Lilian Leistad: THE ROLE OF CYTOKINES AND PHOSPHOLIPASE A_2s IN ARTICULAR CARTILAGE CHONDROCYTES IN RHEUMATOID ARTHRITIS AND OSTEOARTHRITIS
307. Arne Vaaler: EFFECTS OF PSYCHIATRIC INTENSIVE CARE UNIT IN AN ACUTE PSYCIATHRIC WARD
308. Mathias Toft: GENETIC STUDIES OF LRRK2 AND PINK1 IN PARKINSON'S DISEASE
309. Ingrid Løvold Mostad: IMPACT OF DIETARY FAT QUANTITY AND QUALITY IN TYPE 2 DIABETES WITH EMPHASIS ON MARINE N-3 FATTY ACIDS
310. Torill Eidhammer Sjøbakk: MR DETERMINED BRAIN METABOLIC PATTERN IN PATIENTS WITH BRAIN METASTASES AND ADOLESCENTS WITH LOW BIRTH WEIGHT
311. Vidar Beisvåg: PHYSIOLOGICAL GENOMICS OF HEART FAILURE: FROM TECHNOLOGY TO PHYSIOLOGY
312. Olav Magnus Søndenå Fredheim: HEALTH RELATED QUALITY OF LIFE ASSESSMENT AND ASPECTS OF THE CLINICAL PHARMACOLOGY OF METHADONE IN PATIENTS WITH CHRONIC NON-MALIGNANT PAIN
313. Anne Brantberg: FETAL AND PERINATAL IMPLICATIONS OF ANOMALIES IN THE GASTROINTESTINAL TRACT AND THE ABDOMINAL WALL
314. Erik Solligård: GUT LUMINAL MICRODIALYSIS
315. Elin Tollefsen: RESPIRATORY SYMPTOMS IN A COMPREHENSIVE POPULATION BASED STUDY AMONG ADOLESCENTS 13-19 YEARS. YOUNG-HUNT 1995-97 AND 2000-01; THE NORD-TRØNDELAG HEALTH STUDIES (HUNT)
316. Anne-Tove Brenne: GROWTH REGULATION OF MYELOMA CELLS
317. Heidi Knobel: FATIGUE IN CANCER TREATMENT – ASSESSMENT, COURSE AND ETIOLOGY
318. Torbjørn Dahl: CAROTID ARTERY STENOSIS. DIAGNOSTIC AND THERAPEUTIC ASPECTS
319. Inge-Andre Rasmussen jr.: FUNCTIONAL AND DIFFUSION TENSOR MAGNETIC RESONANCE IMAGING IN NEUROSURGICAL PATIENTS
320. Grete Helen Bratberg: PUBERTAL TIMING – ANTECEDENT TO RISK OR RESILIENCE ? EPIDEMIOLOGICAL STUDIES ON GROWTH, MATURATION AND HEALTH RISK BEHAVIOURS; THE YOUNG HUNT STUDY, NORD-TRØNDELAG, NORWAY
321. Sveinung Sørhaug: THE PULMONARY NEUROENDOCRINE SYSTEM. PHYSIOLOGICAL, PATHOLOGICAL AND TUMOURIGENIC ASPECTS
322. Olav Sande Eftedal: ULTRASONIC DETECTION OF DECOMPRESSION INDUCED VASCULAR MICROBUBBLES
323. Rune Bang Leistad: PAIN, AUTONOMIC ACTIVATION AND MUSCULAR ACTIVITY RELATED TO EXPERIMENTALLY-INDUCED COGNITIVE STRESS IN HEADACHE PATIENTS

324. Svein Brekke: TECHNIQUES FOR ENHANCEMENT OF TEMPORAL RESOLUTION IN THREE-DIMENSIONAL ECHOCARDIOGRAPHY
325. Kristian Bernhard Nilsen: AUTONOMIC ACTIVATION AND MUSCLE ACTIVITY IN RELATION TO MUSCULOSKELETAL PAIN
326. Anne Irene Hagen: HEREDITARY BREAST CANCER IN NORWAY. DETECTION AND PROGNOSIS OF BREAST CANCER IN FAMILIES WITH *BRCA1*GENE MUTATION
327. Ingebjørg S. Juel : INTESTINAL INJURY AND RECOVERY AFTER ISCHEMIA. AN EXPERIMENTAL STUDY ON RESTITUTION OF THE SURFACE EPITHELIUM, INTESTINAL PERMEABILITY, AND RELEASE OF BIOMARKERS FROM THE MUCOSA
328. Runa Heimstad: POST-TERM PREGNANCY
329. Jan Egil Afset: ROLE OF ENTEROPATHOGENIC *ESCHERICHIA COLI* IN CHILDHOOD DIARRHOEA IN NORWAY
330. Bent Håvard Hellum: *IN VITRO* INTERACTIONS BETWEEN MEDICINAL DRUGS AND HERBS ON CYTOCHROME P-450 METABOLISM AND P-GLYCOPROTEIN TRANSPORT
331. Morten André Høydal: CARDIAC DYSFUNCTION AND MAXIMAL OXYGEN UPTAKE MYOCARDIAL ADAPTATION TO ENDURANCE TRAINING

2008

332. Andreas Møllerløkken: REDUCTION OF VASCULAR BUBBLES: METHODS TO PREVENT THE ADVERSE EFFECTS OF DECOMPRESSION
333. Anne Hege Aamodt: COMORBIDITY OF HEADACHE AND MIGRAINE IN THE NORD-TRØNDELAG HEALTH STUDY 1995-97
334. Brage Høyem Amundsen: MYOCARDIAL FUNCTION QUANTIFIED BY SPECKLE TRACKING AND TISSUE DOPPLER ECHOCARDIOGRAPHY – VALIDATION AND APPLICATION IN EXERCISE TESTING AND TRAINING
335. Inger Anne Næss: INCIDENCE, MORTALITY AND RISK FACTORS OF FIRST VENOUS THROMBOSIS IN A GENERAL POPULATION. RESULTS FROM THE SECOND NORD-TRØNDELAG HEALTH STUDY (HUNT2)
336. Vegard Bugten: EFFECTS OF POSTOPERATIVE MEASURES AFTER FUNCTIONAL ENDOSCOPIC SINUS SURGERY
337. Morten Bruvold: MANGANESE AND WATER IN CARDIAC MAGNETIC RESONANCE IMAGING
338. Miroslav Fris: THE EFFECT OF SINGLE AND REPEATED ULTRAVIOLET RADIATION ON THE ANTERIOR SEGMENT OF THE RABBIT EYE
339. Svein Arne Aase: METHODS FOR IMPROVING QUALITY AND EFFICIENCY IN QUANTITATIVE ECHOCARDIOGRAPHY – ASPECTS OF USING HIGH FRAME RATE
340. Roger Almvik: ASSESSING THE RISK OF VIOLENCE: DEVELOPMENT AND VALIDATION OF THE BRØSET VIOLENCE CHECKLIST
341. Ottar Sundheim: STRUCTURE-FUNCTION ANALYSIS OF HUMAN ENZYMES INITIATING NUCLEOBASE REPAIR IN DNA AND RNA
342. Anne Mari Undheim: SHORT AND LONG-TERM OUTCOME OF EMOTIONAL AND BEHAVIOURAL PROBLEMS IN YOUNG ADOLESCENTS WITH AND WITHOUT READING DIFFICULTIES
343. Helge Garåsen: THE TRONDHEIM MODEL. IMPROVING THE PROFESSIONAL COMMUNICATION BETWEEN THE VARIOUS LEVELS OF HEALTH CARE SERVICES AND IMPLEMENTATION OF INTERMEDIATE CARE AT A COMMUNITY HOSPITAL COULD PROVIDE BETTER CARE FOR OLDER PATIENTS. SHORT AND LONG TERM EFFECTS
344. Olav A. Foss: "THE ROTATION RATIOS METHOD". A METHOD TO DESCRIBE ALTERED SPATIAL ORIENTATION IN SEQUENTIAL RADIOGRAPHS FROM ONE PELVIS
345. Bjørn Olav Åsvold: THYROID FUNCTION AND CARDIOVASCULAR HEALTH
346. Torun Margareta Melø: NEURONAL GLIAL INTERACTIONS IN EPILEPSY
347. Irina Poliakova Eide: FETAL GROWTH RESTRICTION AND PRE-ECLAMPSIA: SOME CHARACTERISTICS OF FETO-MATERNAL INTERACTIONS IN DECIDUA BASALIS
348. Torunn Askim: RECOVERY AFTER STROKE. ASSESSMENT AND TREATMENT; WITH FOCUS ON MOTOR FUNCTION
349. Ann Elisabeth Åsberg: NEUTROPHIL ACTIVATION IN A ROLLER PUMP MODEL OF CARDIOPULMONARY BYPASS. INFLUENCE ON BIOMATERIAL, PLATELETS AND COMPLEMENT

350. Lars Hagen: REGULATION OF DNA BASE EXCISION REPAIR BY PROTEIN INTERACTIONS AND POST TRANSLATIONAL MODIFICATIONS
351. Sigrun Beate Kjøtrød: POLYCYSTIC OVARY SYNDROME – METFORMIN TREATMENT IN ASSISTED REPRODUCTION
352. Steven Keita Nishiyama: PERSPECTIVES ON LIMB-VASCULAR HETEROGENEITY: IMPLICATIONS FOR HUMAN AGING, SEX, AND EXERCISE
353. Sven Peter Näsholm: ULTRASOUND BEAMS FOR ENHANCED IMAGE QUALITY
354. Jon Ståle Ritland: PRIMARY OPEN-ANGLE GLAUCOMA & EXFOLIATIVE GLAUCOMA. SURVIVAL, COMORBIDITY AND GENETICS
355. Sigrid Botne Sando: ALZHEIMER'S DISEASE IN CENTRAL NORWAY. GENETIC AND EDUCATIONAL ASPECTS
356. Parvinder Kaur: CELLULAR AND MOLECULAR MECHANISMS BEHIND METHYLMERCURY-INDUCED NEUROTOXICITY
357. Ismail Cüneyt Güzey: DOPAMINE AND SEROTONIN RECEPTOR AND TRANSPORTER GENE POLYMORPHISMS AND EXTRAPYRAMIDAL SYMPTOMS. STUDIES IN PARKINSON'S DISEASE AND IN PATIENTS TREATED WITH ANTIPSYCHOTIC OR ANTIDEPRESSANT DRUGS
358. Brit Dybdahl: EXTRA-CELLULAR INDUCIBLE HEAT-SHOCK PROTEIN 70 (Hsp70) – A ROLE IN THE INFLAMMATORY RESPONSE ?
359. Kristoffer Haugarvoll: IDENTIFYING GENETIC CAUSES OF PARKINSON'S DISEASE IN NORWAY
360. Nadra Nilsen: TOLL-LIKE RECEPTOR 2 –EXPRESSION, REGULATION AND SIGNALING
361. Johan Håkon Bjørngaard: PATIENT SATISFACTION WITH OUTPATIENT MENTAL HEALTH SERVICES – THE INFLUENCE OF ORGANIZATIONAL FACTORS.
362. Kjetil Høydal : EFFECTS OF HIGH INTENSITY AEROBIC TRAINING IN HEALTHY SUBJECTS AND CORONARY ARTERY DISEASE PATIENTS; THE IMPORTANCE OF INTENSITY„ DURATION AND FREQUENCY OF TRAINING.
363. Trine Karlsen: TRAINING IS MEDICINE: ENDURANCE AND STRENGTH TRAINING IN CORONARY ARTERY DISEASE AND HEALTH.
364. Marte Thuen: MANGANASE-ENHANCED AND DIFFUSION TENSOR MR IMAGING OF THE NORMAL, INJURED AND REGENERATING RAT VISUAL PATHWAY
365. Cathrine Broberg Vågbø: DIRECT REPAIR OF ALKYLATION DAMAGE IN DNA AND RNA BY 2-OXOGLUTARATE- AND IRON-DEPENDENT DIOXYGENASES
366. Arnt Erik Tjønna: AEROBIC EXERCISE AND CARDIOVASCULAR RISK FACTORS IN OVERWEIGHT AND OBESE ADOLESCENTS AND ADULTS
367. Marianne W. Furnes: FEEDING BEHAVIOR AND BODY WEIGHT DEVELOPMENT: LESSONS FROM RATS
368. Lene N. Johannessen: FUNGAL PRODUCTS AND INFLAMMATORY RESPONSES IN HUMAN MONOCYTES AND EPITHELIAL CELLS
369. Anja Bye: GENE EXPRESSION PROFILING OF *INHERITED* AND *ACQUIRED* MAXIMAL OXYGEN UPTAKE – RELATIONS TO THE METABOLIC SYNDROME.
370. Oluf Dimitri Røe: MALIGNANT MESOTHELIOMA: VIRUS, BIOMARKERS AND GENES. A TRANSLATIONAL APPROACH
371. Ane Cecilie Dale: DIABETES MELLITUS AND FATAL ISCHEMIC HEART DISEASE. ANALYSES FROM THE HUNT1 AND 2 STUDIES
372. Jacob Christian Hølen: PAIN ASSESSMENT IN PALLIATIVE CARE: VALIDATION OF METHODS FOR SELF-REPORT AND BEHAVIOURAL ASSESSMENT
373. Erming Tian: THE GENETIC IMPACTS IN THE ONCOGENESIS OF MULTIPLE MYELOMA
374. Ole Bosnes: KLINISK UTPRØVING AV NORSKE VERSJONER AV NOEN SENTRALE TESTER PÅ KOGNITIV FUNKSJON
375. Ola M. Rygh: 3D ULTRASOUND BASED NEURONAVIGATION IN NEUROSURGERY. A CLINICAL EVALUATION
376. Astrid Kamilla Stunes: ADIPOKINES, PEROXISOME PROFILERATOR ACTIVATED RECEPTOR (PPAR) AGONISTS AND SEROTONIN. COMMON REGULATORS OF BONE AND FAT METABOLISM
377. Silje Engdal: HERBAL REMEDIES USED BY NORWEGIAN CANCER PATIENTS AND THEIR ROLE IN HERB-DRUG INTERACTIONS
378. Kristin Offerdal: IMPROVED ULTRASOUND IMAGING OF THE FETUS AND ITS CONSEQUENCES FOR SEVERE AND LESS SEVERE ANOMALIES

379. Øivind Rognmo: HIGH-INTENSITY AEROBIC EXERCISE AND CARDIOVASCULAR HEALTH
380. Jo-Åsmund Lund: RADIOTHERAPY IN ANAL CARCINOMA AND PROSTATE CANCER

2009

381. Tore Grüner Bjåstad: HIGH FRAME RATE ULTRASOUND IMAGING USING PARALLEL BEAMFORMING
382. Erik Søndenaa: INTELLECTUAL DISABILITIES IN THE CRIMINAL JUSTICE SYSTEM
383. Berit Rostad: SOCIAL INEQUALITIES IN WOMEN'S HEALTH, HUNT 1984-86 AND 1995-97, THE NORD-TRØNDELAG HEALTH STUDY (HUNT)
384. Jonas Crosby: ULTRASOUND-BASED QUANTIFICATION OF MYOCARDIAL DEFORMATION AND ROTATION
385. Erling Tronvik: MIGRAINE, BLOOD PRESSURE AND THE RENIN-ANGIOTENSIN SYSTEM
386. Tom Christensen: BRINGING THE GP TO THE FOREFRONT OF EPR DEVELOPMENT
387. Håkon Bergseng: ASPECTS OF GROUP B STREPTOCOCCUS (GBS) DISEASE IN THE NEWBORN. EPIDEMIOLOGY, CHARACTERISATION OF INVASIVE STRAINS AND EVALUATION OF INTRAPARTUM SCREENING
388. Ronny Myhre: GENETIC STUDIES OF CANDIDATE TENE3S IN PARKINSON'S DISEASE
389. Torbjørn Moe Eggebø: ULTRASOUND AND LABOUR
390. Eivind Wang: TRAINING IS MEDICINE FOR PATIENTS WITH PERIPHERAL ARTERIAL DISEASE
391. Thea Kristin Våtsveen: GENETIC ABERRATIONS IN MYELOMA CELLS
392. Thomas Jozefiak: QUALITY OF LIFE AND MENTAL HEALTH IN CHILDREN AND ADOLESCENTS: CHILD AND PARENT PERSPECTIVES
393. Jens Erik Slagsvold: N-3 POLYUNSATURATED FATTY ACIDS IN HEALTH AND DISEASE – CLINICAL AND MOLECULAR ASPECTS
394. Kristine Misund: A STUDY OF THE TRANSCRIPTIONAL REPRESSOR ICER. REGULATORY NETWORKS IN GASTRIN-INDUCED GENE EXPRESSION
395. Franco M. Impellizzeri: HIGH-INTENSITY TRAINING IN FOOTBALL PLAYERS. EFFECTS ON PHYSICAL AND TECHNICAL PERFORMANCE
396. Kari Hanne Gjeilo: HEALTH-RELATED QUALITY OF LIFE AND CHRONIC PAIN IN PATIENTS UNDERGOING CARDIAC SURGERY
397. Øyvind Hauso: NEUROENDOCRINE ASPECTS OF PHYSIOLOGY AND DISEASE
398. Ingvild Bjellmo Johnsen: INTRACELLULAR SIGNALING MECHANISMS IN THE INNATE IMMUNE RESPONSE TO VIRAL INFECTIONS
399. Linda Tømmerdal Roten: GENETIC PREDISPOSITION FOR DEVELOPMENT OF PREEMCLAMPSIA – CANDIDATE GENE STUDIES IN THE HUNT (NORD-TRØNDELAG HEALTH STUDY) POPULATION
400. Trude Teoline Nausthaug Rakvåg: PHARMACOGENETICS OF MORPHINE IN CANCER PAIN
401. Hanne Lehn: MEMORY FUNCTIONS OF THE HUMAN MEDIAL TEMPORAL LOBE STUDIED WITH fMRI
402. Randi Utne Holt: ADHESION AND MIGRATION OF MYELOMA CELLS – IN VITRO STUDIES –
403. Trygve Solstad: NEURAL REPRESENTATIONS OF EUCLIDEAN SPACE
404. Unn-Merete Fagerli: MULTIPLE MYELOMA CELLS AND CYTOKINES FROM THE BONE MARROW ENVIRONMENT; ASPECTS OF GROWTH REGULATION AND MIGRATION
405. Sigrid Bjørnelv: EATING– AND WEIGHT PROBLEMS IN ADOLESCENTS, THE YOUNG HUNT-STUDY
406. Mari Hoff: CORTICAL HAND BONE LOSS IN RHEUMATOID ARTHRITIS. EVALUATING DIGITAL X-RAY RADIOGRAMMETRY AS OUTCOME MEASURE OF DISEASE ACTIVITY, RESPONSE VARIABLE TO TREATMENT AND PREDICTOR OF BONE DAMAGE
407. Siri Bjørgen: AEROBIC HIGH INTENSITY INTERVAL TRAINING IS AN EFFECTIVE TREATMENT FOR PATIENTS WITH CHRONIC OBSTRUCTIVE PULMONARY DISEASE
408. Susanne Lindqvist: VISION AND BRAIN IN ADOLESCENTS WITH LOW BIRTH WEIGHT
409. Torbjørn Hergum: 3D ULTRASOUND FOR QUANTITATIVE ECHOCARDIOGRAPHY

410. Jørgen Urnes: PATIENT EDUCATION IN GASTRO-OESOPHAGEAL REFLUX DISEASE. VALIDATION OF A DIGESTIVE SYMPTOMS AND IMPACT QUESTIONNAIRE AND A RANDOMISED CONTROLLED TRIAL OF PATIENT EDUCATION
411. Elvar Eyjolfsson: 13C NMRS OF ANIMAL MODELS OF SCHIZOPHRENIA
412. Marius Steiro Fimland: CHRONIC AND ACUTE NEURAL ADAPTATIONS TO STRENGTH TRAINING
413. Øyvind Støren: RUNNING AND CYCLING ECONOMY IN ATHLETES; DETERMINING FACTORS, TRAINING INTERVENTIONS AND TESTING
414. Håkon Hov: HEPATOCYTE GROWTH FACTOR AND ITS RECEPTOR C-MET. AUTOCRINE GROWTH AND SIGNALING IN MULTIPLE MYELOMA CELLS
415. Maria Radtke: ROLE OF AUTOIMMUNITY AND OVERSTIMULATION FOR BETA-CELL DEFICIENCY. EPIDEMIOLOGICAL AND THERAPEUTIC PERSPECTIVES
416. Liv Bente Romundstad: ASSISTED FERTILIZATION IN NORWAY: SAFETY OF THE REPRODUCTIVE TECHNOLOGY
417. Erik Magnus Berntsen: PREOPERATIV PLANNING AND FUNCTIONAL NEURONAVIGATION – WITH FUNCTIONAL MRI AND DIFFUSION TENSOR TRACTOGRAPHY IN PATIENTS WITH BRAIN LESIONS
418. Tonje Strømmen Steigedal: MOLECULAR MECHANISMS OF THE PROLIFERATIVE RESPONSE TO THE HORMONE GASTRIN
419. Vidar Rao: EXTRACORPOREAL PHOTOCHEMOTHERAPY IN PATIENTS WITH CUTANEOUS T CELL LYMPHOMA OR GRAFT-vs-HOST DISEASE
420. Torkild Visnes: DNA EXCISION REPAIR OF URACIL AND 5-FLUOROURACIL IN HUMAN CANCER CELL LINES

2010

421. John Munkhaugen: BLOOD PRESSURE, BODY WEIGHT, AND KIDNEY FUNCTION IN THE NEAR-NORMAL RANGE: NORMALITY, RISK FACTOR OR MORBIDITY ?
422. Ingrid Castberg: PHARMACOKINETICS, DRUG INTERACTIONS AND ADHERENCE TO TREATMENT WITH ANTIPSYCHOTICS: STUDIES IN A NATURALISTIC SETTING
423. Jian Xu: BLOOD-OXYGEN-LEVEL-DEPENDENT-FUNCTIONAL MAGNETIC RESONANCE IMAGING AND DIFFUSION TENSOR IMAGING IN TRAUMATIC BRAIN INJURY RESEARCH
424. Sigmund Simonsen: ACCEPTABLE RISK AND THE REQUIREMENT OF PROPORTIONALITY IN EUROPEAN BIOMEDICAL RESEARCH LAW. WHAT DOES THE REQUIREMENT THAT BIOMEDICAL RESEARCH SHALL NOT INVOLVE RISKS AND BURDENS DISPROPORTIONATE TO ITS POTENTIAL BENEFITS MEAN?
425. Astrid Woodhouse: MOTOR CONTROL IN WHIPLASH AND CHRONIC NON-TRAUMATIC NECK PAIN
426. Line Rørstad Jensen: EVALUATION OF TREATMENT EFFECTS IN CANCER BY MR IMAGING AND SPECTROSCOPY
427. Trine Moholdt: AEROBIC EXERCISE IN CORONARY HEART DISEASE
428. Øystein Olsen: ANALYSIS OF MANGANESE ENHANCED MRI OF THE NORMAL AND INJURED RAT CENTRAL NERVOUS SYSTEM
429. Bjørn H. Grønberg: PEMETREXED IN THE TREATMENT OF ADVANCED LUNG CANCER
430. Vigdis Schnell Husby: REHABILITATION OF PATIENTS UNDERGOING TOTAL HIP ARTHROPLASTY WITH FOCUS ON MUSCLE STRENGTH, WALKING AND AEROBIC ENDURANCE PERFORMANCE
431. Torbjørn Øien: CHALLENGES IN PRIMARY PREVENTION OF ALLERGY. THE PREVENTION OF ALLERGY AMONG CHILDREN IN TRONDHEIM (PACT) STUDY.
432. Kari Anne Indredavik Evensen: BORN TOO SOON OR TOO SMALL: MOTOR PROBLEMS IN ADOLESCENCE
433. Lars Adde: PREDICTION OF CEREBRAL PALSY IN YOUNG INFANTS. COMPUTER BASED ASSESSMENT OF GENERAL MOVEMENTS
434. Magnus Fasting: PRE- AND POSTNATAL RISK FACTORS FOR CHILDHOOD ADIPOSITY
435. Vivi Talstad Monsen: MECHANISMS OF ALKYLATION DAMAGE REPAIR BY HUMAN AlkB HOMOLOGUES

436. Toril Skandsen: MODERATE AND SEVERE TRAUMATIC BRAIN INJURY. MAGNETIC RESONANCE IMAGING FINDINGS, COGNITION AND RISK FACTORS FOR DISABILITY
437. Ingeborg Smidesang: ALLERGY RELATED DISORDERS AMONG 2-YEAR OLDS AND ADOLESCENTS IN MID-NORWAY – PREVALENCE, SEVERITY AND IMPACT. THE PACT STUDY 2005, THE YOUNG HUNT STUDY 1995-97
438. Vidar Halsteinli: MEASURING EFFICIENCY IN MENTAL HEALTH SERVICE DELIVERY: A STUDY OF OUTPATIENT UNITS IN NORWAY
439. Karen Lehrmann Ægidius: THE PREVALENCE OF HEADACHE AND MIGRAINE IN RELATION TO SEX HORMONE STATUS IN WOMEN. THE HUNT 2 STUDY
440. Madelene Ericsson: EXERCISE TRAINING IN GENETIC MODELS OF HEART FAILURE
441. Marianne Klokk: THE ASSOCIATION BETWEEN SELF-REPORTED ECZEMA AND COMMON MENTAL DISORDERS IN THE GENERAL POPULATION. THE HORDALAND HEALTH STUDY (HUSK)
442. Tomas Ottemo Stølen: IMPAIRED CALCIUM HANDLING IN ANIMAL AND HUMAN CARDIOMYOCYTES REDUCE CONTRACTILITY AND INCREASE ARRHYTHMIA POTENTIAL – EFFECTS OF AEROBIC EXERCISE TRAINING
443. Bjarne Hansen: ENHANCING TREATMENT OUTCOME IN COGNITIVE BEHAVIOURAL THERAPY FOR OBSESSIVE COMPULSIVE DISORDER: THE IMPORTANCE OF COGNITIVE FACTORS
444. Mona Løvlien: WHEN EVERY MINUTE COUNTS. FROM SYMPTOMS TO ADMISSION FOR ACUTE MYOCARDIAL INFARCTION WITH SPECIAL EMPHASIS ON GENDER DIFFERECES
445. Karin Margaretha Gilljam: DNA REPAIR PROTEIN COMPLEXES, FUNCTIONALITY AND SIGNIFICANCE FOR REPAIR EFFICIENCY AND CELL SURVIVAL
446. Anne Byriel Walls: NEURONAL GLIAL INTERACTIONS IN CEREBRAL ENERGY – AND AMINO ACID HOMEOSTASIS – IMPLICATIONS OF GLUTAMATE AND GABA
447. Cathrine Fallang Knetter: MECHANISMS OF TOLL-LIKE RECEPTOR 9 ACTIVATION
448. Marit Følsvik Svindseth: A STUDY OF HUMILIATION, NARCISSISM AND TREATMENT OUTCOME IN PATIENTS ADMITTED TO PSYCHIATRIC EMERGENCY UNITS
449. Karin Elvenes Bakkelund: GASTRIC NEUROENDOCRINE CELLS – ROLE IN GASTRIC NEOPLASIA IN MAN AND RODENTS
450. Kirsten Brun Kjelstrup: DORSOVENTRAL DIFFERENCES IN THE SPATIAL REPRESENTATION AREAS OF THE RAT BRAIN
451. Roar Johansen: MR EVALUATION OF BREAST CANCER PATIENTS WITH POOR PROGNOSIS
452. Rigmor Myran: POST TRAUMATIC NECK PAIN. EPIDEMIOLOGICAL, NEURORADIOLOGICAL AND CLINICAL ASPECTS
453. Krisztina Kunszt Johansen: GENEALOGICAL, CLINICAL AND BIOCHEMICAL STUDIES IN *LRRK2* – ASSOCIATED PARKINSON'S DISEASE
454. Pål Gjerden: THE USE OF ANTICHOLINERGIC ANTIPARKINSON AGENTS IN NORWAY. EPIDEMIOLOGY, TOXICOLOGY AND CLINICAL IMPLICATIONS
455. Else Marie Huuse: ASSESSMENT OF TUMOR MICROENVIRONMENT AND TREATMENT EFFECTS IN HUMAN BREAST CANCER XENOGRAFTS USING MR IMAGING AND SPECTROSCOPY
456. Khalid S. Ibrahim: INTRAOPERATIVE ULTRASOUND ASSESSMENT IN CORONARY ARTERY BYPASS SURGERY – WITH SPECIAL REFERENCE TO CORONARY ANASTOMOSES AND THE ASCENDING AORTA
457. Bjørn Øglænd: ANTHROPOMETRY, BLOOD PRESSURE AND REPRODUCTIVE DEVELOPMENT IN ADOLESCENCE OF OFFSPRING OF MOTHERS WHO HAD PREECLAMPSIA IN PREGNANCY
458. John Olav Roaldset: RISK ASSESSMENT OF VIOLENT, SUICIDAL AND SELF-INJURIOUS BEHAVIOUR IN ACUTE PSYCHIATRY – A BIO-PSYCHO-SOCIAL APPROACH
459. Håvard Dalen: ECHOCARDIOGRAPHIC INDICES OF CARDIAC FUNCTION – NORMAL VALUES AND ASSOCIATIONS WITH CARDIAC RISK FACTORS IN A POPULATION FREE FROM CARDIOVASCULAR DISEASE, HYPERTENSION AND DIABETES: THE HUNT 3 STUDY
460. Beate André: CHANGE CAN BE CHALLENGING. INTRODUCTION TO CHANGES AND IMPLEMENTATION OF COMPUTERIZED TECHNOLOGY IN HEALTH CARE

461. Latha Nrugham: ASSOCIATES AND PREDICTORS OF ATTEMPTED SUICIDE AMONG DEPRESSED ADOLESCENTS – A 6-YEAR PROSPECTIVE STUDY
462. Håvard Bersås Nordgaard: TRANSIT-TIME FLOWMETRY AND WALL SHEAR STRESS ANALYSIS OF CORONARY ARTERY BYPASS GRAFTS – A CLINICAL AND EXPERIMENTAL STUDY

Cotutelle with University of Ghent: Abigail Emily Swillens: A MULTIPHYSICS MODEL FOR IMPROVING THE ULTRASONIC ASSESSMENT OF LARGE ARTERIES

2011

463. Marte Helene Bjørk: DO BRAIN RHYTHMS CHANGE BEFORE THE MIGRAINE ATTACK? A LONGITUDINAL CONTROLLED EEG STUDY
464. Carl-Jørgen Arum: A STUDY OF UROTHELIAL CARCINOMA: GENE EXPRESSION PROFILING, TUMORIGENESIS AND THERAPIES IN ORTHOTOPIC ANIMAL MODELS
465. Ingunn Harstad: TUBERCULOSIS INFECTION AND DISEASE AMONG ASYLUM SEEKERS IN NORWAY. SCREENING AND FOLLOW-UP IN PUBLIC HEALTH CARE
466. Leif Åge Strand: EPIDEMIOLOGICAL STUDIES AMONG ROYAL NORWEGIAN NAVY SERVICEMEN. COHORT ESTABLISHMENT, CANCER INCIDENCE AND CAUSE-SPECIFIC MORTALITY
467. Katrine Høyer Holgersen: SURVIVORS IN THEIR THIRD DECADE AFTER THE NORTH SEA OIL RIG DISASTER OF 1980. LONG-TERM PERSPECTIVES ON MENTAL HEALTH
468. MarianneWallenius: PREGNANCY RELATED ASPECTS OF CHRONIC INFLAMMATORY ARTHRITIDES: DISEASE ONSET POSTPARTUM, PREGNANCY OUTCOMES AND FERTILITY. DATA FROM A NORWEGIAN PATIENT REGISTRY LINKED TO THE MEDICAL BIRTH REGISTRY OF NORWAY
469. Ole Vegard Solberg: 3D ULTRASOUND AND NAVIGATION – APPLICATIONS IN LAPAROSCOPIC SURGERY
470. Inga Ekeberg Schjerve: EXERCISE-INDUCED IMPROVEMENT OF MAXIMAL OXYGEN UPTAKE AND ENDOTHELIAL FUNCTION IN OBESE AND OVERWEIGHT INDIVIDUALS ARE DEPENDENT ON EXERCISE-INTENSITY
471. Eva Veslemøy Tyldum: CARDIOVASCULAR FUNCTION IN PREECLAMPSIA – WITH REFERENCE TO ENDOTHELIAL FUNCTION, LEFT VENTRICULAR FUNCTION AND PRE-PREGNANCY PHYSICAL ACTIVITY
472. Benjamin Garzón Jiménez de Cisneros: CLINICAL APPLICATIONS OF MULTIMODAL MAGNETIC RESONANCE IMAGING
473. Halvard Knut Nilsen: ASSESSING CODEINE TREATMENT TO PATIENTS WITH CHRONIC NON-MALIGNANT PAIN: NEUROPSYCHOLOGICAL FUNCTIONING, DRIVING ABILITY AND WEANING
474. Eiliv Brenner: GLUTAMATE RELATED METABOLISM IN ANIMAL MODELS OF SCHIZOPHRENIA
475. Egil Jonsbu: CHEST PAIN AND PALPITATIONS IN A CARDIAC SETTING; PSYCHOLOGICAL FACTORS, OUTCOME AND TREATMENT
476. Mona Høysæter Fenstad: GENETIC SUSCEPTIBILITY TO PREECLAMPSIA : STUDIES ON THE NORD-TRØNDELAG HEALTH STUDY (HUNT) COHORT, AN AUSTRALIAN/NEW ZEALAND FAMILY COHORT AND DECIDUA BASALIS TISSUE
477. Svein Erik Gaustad: CARDIOVASCULAR CHANGES IN DIVING: FROM HUMAN RESPONSE TO CELL FUNCTION
478. Karin Torvik: PAIN AND QUALITY OF LIFE IN PATIENTS LIVING IN NURSING HOMES
479. Arne Solberg: OUTCOME ASSESSMENTS IN NON-METASTATIC PROSTATE CANCER
480. Henrik Sahlin Pettersen: CYTOTOXICITY AND REPAIR OF URACIL AND 5-FLUOROURACIL IN DNA
481. Pui-Lam Wong: PHYSICAL AND PHYSIOLOGICAL CAPACITY OF SOCCER PLAYERS: EFFECTS OF STRENGTH AND CONDITIONING
482. Ole Solheim: ULTRASOUND GUIDED SURGERY IN PATIENTS WITH INTRACRANIAL TUMOURS
483. Sten Roar Snare: QUANTITATIVE CARDIAC ANALYSIS ALGORITHMS FOR POCKET-SIZED ULTRASOUND DEVICES